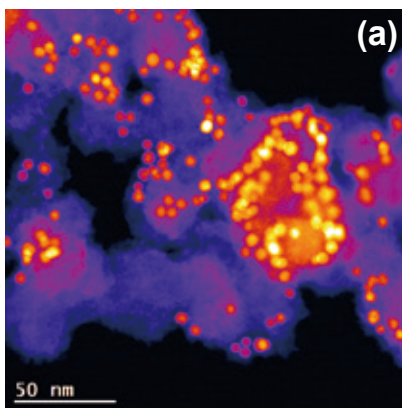
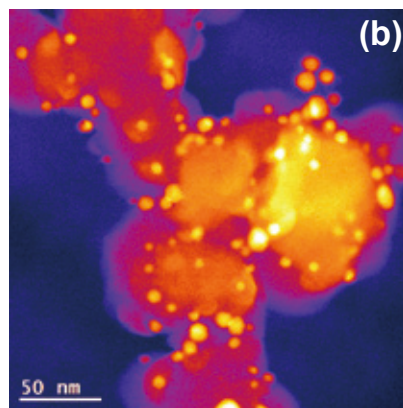
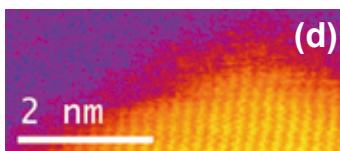
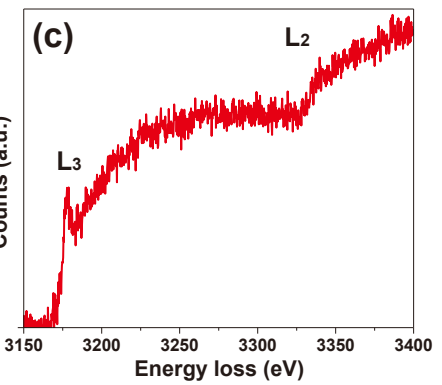
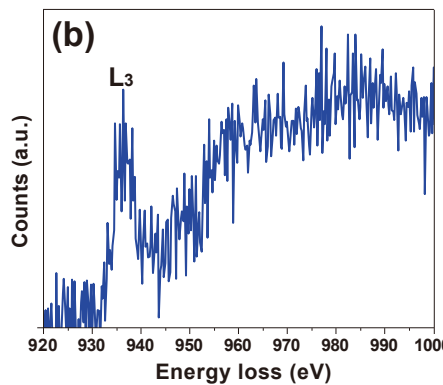
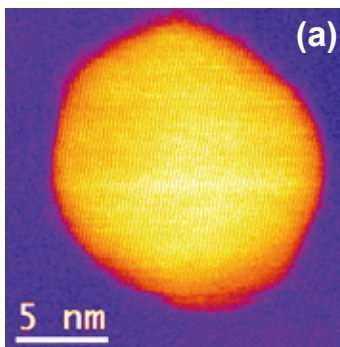
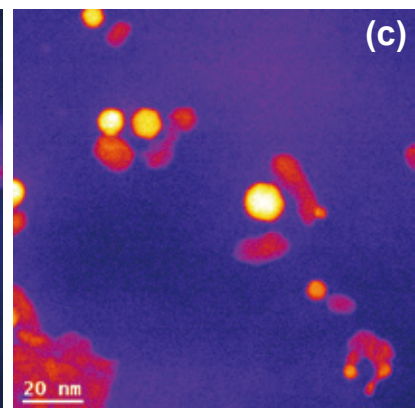
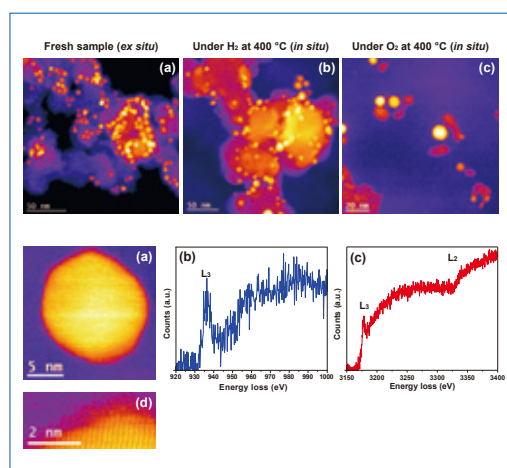


Fresh sample (*ex situ*)Under H<sub>2</sub> at 400 °C (*in situ*)Under O<sub>2</sub> at 400 °C (*in situ*)

- Degradation of CuPd Nanoparticles upon Redox Cycling Shown by *In situ* Scanning Transmission Electron Microscopy in the JEOL NEOARM .....2  
 Alexandre C. Foucher<sup>1</sup>, Eric A. Stach<sup>1,2</sup>  
<sup>1</sup>Department of Materials Science and Engineering, University of Pennsylvania  
<sup>2</sup>Laboratory for Research on the Structure of Matter, University of Pennsylvania
- Accurate Quantification of Q<sup>n</sup> Species Distributions in Modified Silicate Glass by Phase Adjusted Spinning Sideband NMR Experiment .....6  
 Lekhan Lodhi and Krishna Kishor Dey Dr. Harisingh Gour Central University
- Electron Cryomicroscopy: Recent Progress and Future Perspective for Structural Life Sciences .....10  
 Keiichi Namba<sup>1,2</sup> and Fumiaki Makino<sup>1,3</sup>  
<sup>1</sup>Graduate School of Frontier Biosciences, Osaka University, <sup>2</sup>RIKEN SPring-8 Center, <sup>3</sup>JEOL Ltd.
- Chemical-State Analysis of Li Compounds and Nitrogen-Getter Material for Liquid Li by Soft X-ray Emission Spectroscopy .....18  
 Keisuke Mukai<sup>1,2</sup>, Ryo Omura<sup>1</sup>, Juro Yagi<sup>1</sup>, Ryuta Kasada<sup>3</sup>  
<sup>1</sup>Institute of Advanced Energy, Kyoto University, <sup>2</sup>Kyoto Fusion Engineering Ltd. <sup>3</sup>Institute for Material Research, Tohoku University
- Observation and Analysis of Micro-Textures in Mineral Samples with an Aberration Corrected STEM .....23  
 Ichiro Ohnishi EM Business Unit, JEOL Ltd.
- New Semi-in-lens SEM JSM-IT800 .....28  
 Excellent for Semiconductor Device Observation .....28  
 Motohiro Nakamura and Yuhei Nakajima EP Business Unit, JEOL Ltd.
- Automated TEM lamella Preparation with JIB-4700F .....35  
 Yoshitaka Ishihara, Tomohiro Mihira EP Business Unit, JEOL Ltd.
- Spectrum Imaging for Secondary Electrons and Backscattered Electrons Using Band Pass Filter with Variable Energy Resolution .....40  
 Tatsuya Uchida<sup>1</sup>, Konomi Ikita<sup>1</sup>, Akihiro Tanaka<sup>1</sup>, Kazushiro Yokouchi<sup>1</sup>, Nobuyuki Ikee<sup>1</sup>, Kenichi Tsutsumi<sup>1</sup>, Noboru Taguchi<sup>2</sup>  
<sup>1</sup>JEOL Ltd. <sup>2</sup>National Institute of Advanced Industrial Science and Technology (AIST)
- Developing an Electron-Beam Metal 3D Printer JAM-5200EBM .....48  
 Ayumu Miyakita 3D Additive Manufacturing Project, JEOL Ltd.
- Gas Chromatograph - Quadrupole Mass Spectrometer, JMS-Q1600GC UltraQuad™ SQ-Zeta .....51  
 Yoshio Abe and Masaaki Ubukata MS Business Unit, JEOL Ltd.
- Introduction of JEOL Products .....56



## Cover micrograph

Atomic-scale study of structural changes of Cu<sub>80</sub>Pd<sub>20</sub> particles during a redox cycle. Top row shows HAADF-STEM images of (a) fresh sample (particles supported on amorphous carbon), (b) sample after reduction (at elevated temperature of 400 °C) showing moderate sintering, and (c) oxidized sample (400 °C) with internal segregation of Cu and Pd, and extensive sintering caused by collapse of the carbon support. Bottom row shows STEM and EELS analyses of a single particle under O<sub>2</sub> (400 °C) after oxidation. (a) HAADF-STEM image of the whole particle and (d) its magnified image showing a thin and amorphous CuO layer on top of the crystalline particle. (b) and (c) EELS spectra of Cu L<sub>2,3</sub> edge indicating the presence of CuO and of Pd L<sub>2,3</sub> edge revealing the presence of PdO.

# Degradation of CuPd Nanoparticles upon Redox Cycling Shown by *In situ* Scanning Transmission Electron Microscopy in the JEOL NEOARM

Alexandre C. Foucher<sup>1</sup>, Eric A. Stach<sup>1,2</sup>

<sup>1</sup> Department of Materials Science and Engineering, University of Pennsylvania

<sup>2</sup> Laboratory for Research on the Structure of Matter, University of Pennsylvania

Palladium is a major catalyst used in industrial processes and environmental engineering. However, the high price of palladium limits its application for large-scale chemical production. To circumvent this issue, palladium is often incorporated with a less expensive material to reduce the costs of catalysts. In this work, bimetallic Cu<sub>20</sub>Pd<sub>80</sub> particles were studied with *in situ* scanning transmission electron microscopy (STEM) in the JEOL NEOARM (JEM-ARM200F). We report structural modification of Cu<sub>80</sub>Pd<sub>20</sub> particles, primarily upon oxidation, that can be expected to impact the activity of the material. Exposure to an oxidative atmosphere leads to substantial segregation of Cu oxide, and Pd atoms became covered with Cu atoms. Electron energy loss spectroscopy (EELS) showed oxidation of Pd after exposure to O<sub>2</sub> at 400 °C. In contrast, the particles remained stable under a reductive environment at elevated temperatures. These results emphasize the necessity of keeping Cu-Pd systems under a reductive environment to avoid segregation of Cu oxide on the surface, resulting in the catalyst deactivation.

## Introduction

Heterogeneous catalysis plays a crucial role in the industrial production of chemicals. In fact, transition metals are relevant candidates to control chemical reactions for efficient production of fuels and environmental engineering. For instance, Pd nanoparticles are excellent catalysts in automobile catalytic converters for transforming toxic hydrocarbons and nitrogen oxides into less harmful products [1, 2]. Another important example is Lindlar's catalyst, which consists of Pd deposited on CaCO<sub>3</sub> for the hydrogenation of alkynes [3]. The adsorption of alkynes on a Pd surface leads to the formation of alkenes, which are valuable molecules to synthesize alcohols or plastics.

However, Pd became very expensive due to its ubiquitous usage and scarcity. To reduce the cost of Pd-based catalysts, it is advantageous to dilute Pd atoms into a less expensive metal and optimize Pd's catalytic activity [4, 5]. The mixture with a less expensive metal can increase the surface of exposed Pd to maximize metal-gas interactions. Additionally, previous publications have shown synergetic effects obtained with mixing two transition metals [6, 7]. The combination of two metals can lead to enhanced activity and selectivity and ultimately yield better control of chemical reactions. Specifically, it has been shown that Cu-Pd systems can display improved properties for a range of chemical reactions [8, 9]. However, little is known about dynamical changes in the Cu-Pd catalysts during reaction.

The knowledge of changes in morphology, composition, and valence state is necessary to guide the design of stable and efficient nanocatalysts.

We performed a STEM-EELS analysis of Cu<sub>80</sub>Pd<sub>20</sub> particles using both *ex situ* and *in situ* conditions to answer these questions. For the *ex situ* analysis, free-standing particles were analyzed. The particles were deposited on an amorphous carbon support with a 20% metal weight loading for *in situ* analysis. This was done to avoid sintering of free-standing CuPd particles and to recreate realistic conditions. In fact, nanocatalysts are often deposited on a substrate such as amorphous carbon or oxides to stabilize the particles.

## Experimental details

Cu<sub>80</sub>Pd<sub>20</sub> particles were synthesized with a previously reported method [10].

For this study, a JEOL NEOARM was used in STEM mode. Dark-field images were collected with a camera length of 4 cm and a probe current of 150 pA. For EELS, the camera length was 2 cm, and the probe current was 700 pA. EELS data were collected with a K2-IS camera provided by Gatan, in Summit mode. *In situ* experiments were done with a gas-heating holder provided by Hummingbird Scientific. The sample was deposited on an SiN<sub>3</sub> chip and was enclosed into a micro-cell on the tip of the environmental holder. Control of temperature and gas

flow inside the cell was achieved with a gas system provided by Hummingbird Scientific. The temperature was ramped up with a rate of 10 °C/min, and the flow of gases was 5 sccm. Only pure gases were used, and the cell was purged with N<sub>2</sub> after exposure to H<sub>2</sub> and before introducing O<sub>2</sub>. In the *in situ* experiment, the catalyst was exposed to 400 °C under H<sub>2</sub> for 1 hour. Then, the temperature was decreased to room temperature, the cell was purged with N<sub>2</sub>, and O<sub>2</sub> was introduced. Ultimately, the system was exposed to O<sub>2</sub> at 400 °C for 1 hour.

## Results and Discussion

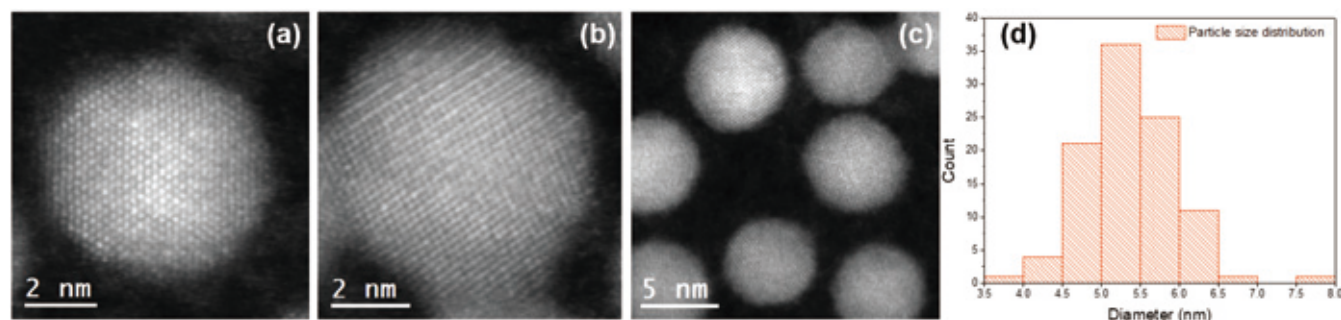
First, an *ex situ* analysis was performed on free-standing Cu<sub>80</sub>Pd<sub>20</sub> particles. High-angle annular dark-field (HAADF)-STEM images obtained with the JEOL NEOARM instrument are shown in **Figure 1**. Most particles had a random alloy configuration, as shown in Figure 1a, as some atomic columns are brighter than others in a random fashion. In fact, the brightness of atoms is proportional to Z<sup>1.65</sup> in HAADF imaging, one can conclude that bright columns contain more Pd atoms than dim columns [11]. In some cases, it was possible to observe an intermetallic solution, as shown in Figure 1b. It is possible to identify bright rows of atoms between dim rows of atoms richer

in Cu. Figure 1c shows a representative set of Cu<sub>80</sub>Pd<sub>20</sub> particles. The nanostructures are spherical and monodispersed (5.34 ± 0.57 nm). Figure 1d shows the size distribution over 100 particles and underlines that most particles have a diameter comprised between 4.5 nm and 6.5 nm.

Energy-dispersive X-ray spectroscopy (EDS) and EELS were also performed. Elemental mappings with EDS data show a uniform distribution of Cu and Pd within individual particles (**Figure 2a-c**). EELS analysis indicates that Cu and Pd are not oxidized, as no white line could be seen on the L<sub>2,3</sub> edges for both elements (Figure 2d and 2e). The presence of a white line is a characteristic of CuO and PdO and is due to unfilled 3d orbitals in oxides that allow additional energy transitions visible as a peak in the L<sub>2,3</sub> edges. The reference spectrum for Cu<sub>2</sub>O has no white line, but the absence of detected oxygen with EELS emphasizes that Cu is metallic in the fresh sample. To conclude, the fresh sample of free-standing Cu<sub>80</sub>Pd<sub>20</sub> particles had metallic Cu and Pd, and no substantial traces of oxygen were detected. The high intensity of signal from the Pd L<sub>2,3</sub> is a direct result of the high brightness of the cold field-emission source of the NEOARM, the CESCOR aberration corrector and the use of the K2-IS detector.

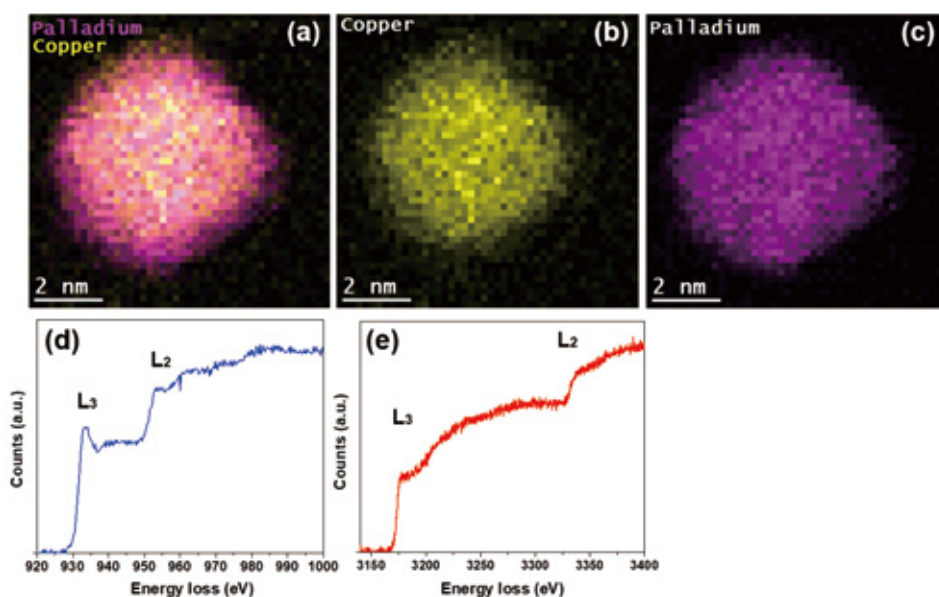
Following this initial *ex situ* analysis, the nanoparticles were

**Fig. 1 HAADF-STEM images and particle size distribution of the Cu<sub>80</sub>Pd<sub>20</sub> samples.**



(a) Atomic resolution image showing the random alloy configuration that was observed in most particles. (b) Atomic resolution image showing an intermetallic solution of Cu and Pd. (c) Representative set of Cu<sub>80</sub>Pd<sub>20</sub> particles. (d) Particle size distribution. The particles are monodispersed, and most particles have a diameter between 4.5 nm and 6.5 nm.

**Fig. 2 EDS and EELS analysis of the sample under *ex situ* conditions.**



(a) Combined EDS map of Cu and Pd indicating a uniform mixing between Cu and Pd. (b) EDS map for Cu. (c) EDS map for Pd. (d) Cu L<sub>2,3</sub> edge indicating a metallic state. (e) Pd L<sub>2,3</sub> edge with no white line, indicating a metallic state for Pd.



deposited on an amorphous carbon film with a metal weight loading of 20%. The sample was enclosed in a microcell in the environmental holder and was exposed to the redox cycle described in the “experimental details” section.

HAADF-STEM images for each step of the cycle are shown in **Figure 3**. The sample was particularly sensitive to the beam, hence images from different regions are shown for each step to avoid beam-induced effect after multiple imaging. In the fresh sample, the particles are dispersed on the carbon film, and some particles are located very close to each other (Figure 3a). After exposure to  $H_2$  at 400 °C, it is possible to observe some sintering and formation of larger particles (Figure 3b). It should be noticed that Figures 3a and 3b have the same size for the scalebar. Finally, internal segregation of Cu and Pd was not observed, as no dimmer regions within the particles were visible. Based on the brightness and contrast, no Pd-rich regions could be seen on the HAADF-STEM images.

Upon exposure to oxygen at high temperatures, the amorphous carbon support collapsed. Additionally, Cu was pulled out of the particles, and Cu oxide “leaked out” of the  $Cu_{80}Pd_{20}$  particles. The segregated CuO is indicated by the red arrows in Figure 3c. The dim brightness indicates a light oxide, and an additional EELS analysis indicated that these regions were composed of CuO.

A more detailed analysis was performed on the sample after oxidation, as the changes to the catalyst were substantial. **Figure 4** summarizes an analysis on a single, larger-than-average particle at the end of the redox cycle. Figure 4a shows an atomic resolution HAADF-STEM image of a single particle taken in an the  $O_2$  environment at 400 °C. In Figures 4b and 4c, EELS analysis was performed on the particle and showed that Cu became oxidized into CuO within the particles. Indeed, the analysis was performed on the particle, excluding Cu oxide that migrated out of the particles, as in Figure 3d. The study of the Pd  $L_{2,3}$  edge displayed the characteristic “white line” for the PdO phase. Thus, the oxidative conditions were strong enough to oxidize Pd, even though Cu migrated to the surface and covered Pd. The white line was visible for EELS data collected on the edges and the middle of the particle. Even though the presence of metallic Pd in the core cannot be excluded, the EELS investigation shows a deep penetration of oxygen inside the particles, leading to the formation of Pd oxide well below the surface. A higher magnification HAADF-STEM image (Figure 4d) shows the presence of a dim layer covering the crystalline particles. The low brightness and the apparent amorphous structure show that CuO is covering the particle's surface.

The dynamical restructuring effects during the redox cycle

**Fig. 3 HAADF-STEM images showing the sample's evolution during the redox cycle.**

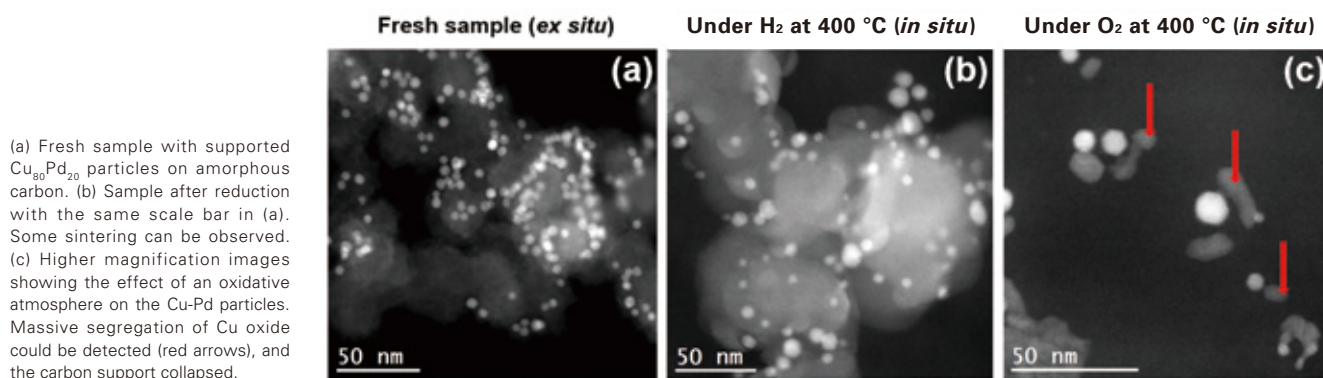
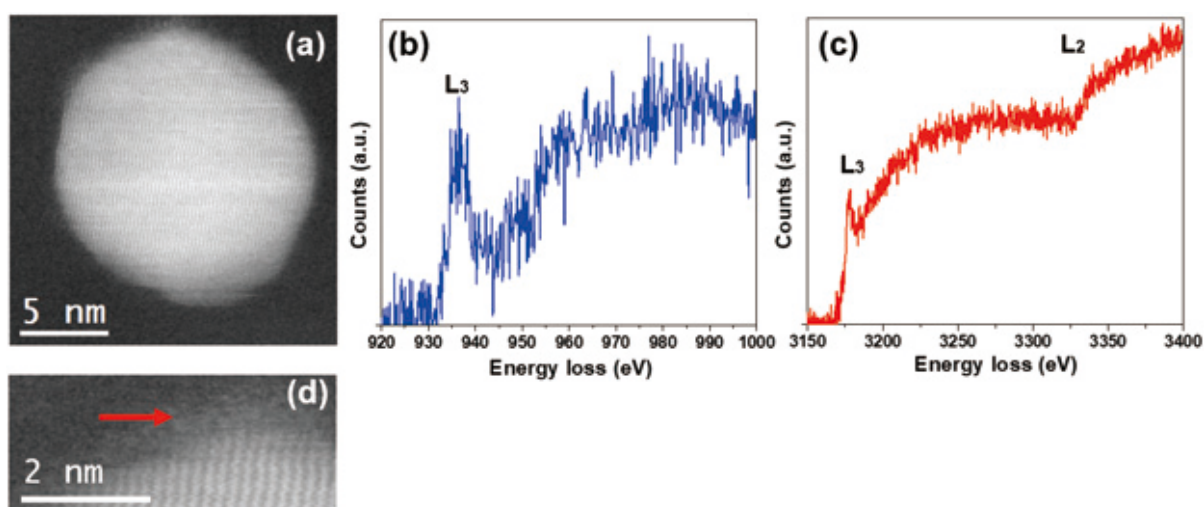


**Fig. 4 STEM and EELS analysis of a single particle under  $O_2$  at 400 °C.**



underline degradation mechanisms under reductive and oxidative environments. Under H<sub>2</sub> at elevated temperature, no segregation of Cu was visible, as the brightness within the particles remained uniform, as was the case for the fresh sample. Nevertheless, substantial particle migration and coalescence occurred under H<sub>2</sub> at 400 °C for 1 hour. Thus, the Cu-Pd alloy conformation does not appear as stable as other alloys reported in the literature [12]. However, the random alloy configuration was not altered, suggesting that Cu-Pd particles are efficient at maintaining surface Pd under reductive conditions at elevated temperatures.

In contrast, the changes under an oxidative environment at elevated temperatures can be expected and affect the catalytic activity more significantly. In fact, Pd becomes covered with Cu oxide, which will then prevent any surface reactions with the precious metal component. The migration of Cu from the core of the particles to the surface, under oxidative conditions, is due to the high oxophilicity of Cu [13]. Additionally, Pd is oxidized into PdO, which can be an advantage or a drawback for specific chemical reactions. Some investigations suggest superior selectivity of PdO over Pd for dimethyl ether production through dehydration of methanol [14]. Other reports indicate better benzyl alcohol conversion for Pd instead of PdO, within an Au-Pd alloy [15]. Also, one can say that Cu is not as efficient as other transition metals, such as Au, at preventing the oxidation of Pd [15]. It is also interesting to note that EELS maps on the particles after oxidation did not suggest the presence of a large core with metallic Pd. Hence, exposure to O<sub>2</sub> at 400°C leads to significant structural and valence state modification. The process is also irreversible, as Cu oxide migrated outside of the particles upon exposure to oxygen and became wholly separated from the remaining Pd-rich particle.

---

## Conclusions

In conclusion, we used *ex situ* and *in situ* STEM with the JEOL NEOARM to understand structural changes of Cu<sub>80</sub>Pd<sub>20</sub> particles under a redox cycle at the atomic scale. The particles initially had a random alloy configuration with no apparent segregation of Cu or Pd. Upon exposure to H<sub>2</sub> at 400 °C for one hour, no segregation of Cu was visible. Substantial sintering of the carbon-supported sample could also be observed. Upon oxidation with O<sub>2</sub> at 400 °C for 1 hour, it was possible to observe strong segregation of Cu to the surface. We observed full separation of Cu oxide, suggesting an irreversible degradation of the catalysis. We also detected remaining Cu oxide covering the surface of the particles, preventing surface reaction with Pd. EELS analysis on a single particle showed global oxidation of Cu and Pd even in sub-surface regions. The changes in Pd valence states and the presence of Cu oxide on the surface of the particles are substantial hurdles for the efficiency of CuPd alloys under oxidative conditions. These results clearly demonstrate the utility of aberration-corrected STEM in the NEOARM instrument for the analytical characterization of bimetallic catalysts in reactive environments. These insights can be applied to a wide range of bimetallic structures and provide guidelines to understand and design novel catalysts.

---

## Acknowledgments

This work was supported as part of the Integrated Mesoscale Architectures for Sustainable Catalysis (IMASC), an Energy Frontier Research Center funded by the U.S. Department of Energy, Office of Science, Basic Energy Sciences under

Award #DE-SC0012573. Experiments were also carried out at the Singh Center for Nanotechnology at the University of Pennsylvania, supported by the National Science Foundation (NSF) National Nanotechnology Coordinated Infrastructure Program grant NNCI-1542153. Additional support to the Nanoscale Characterization Facility at the Singh Center has been provided by the Laboratory for Research on the Structure of Matter (MRSEC) supported by the National Science Foundation (DMR-1720530).

Note: Eric Stach is a co-founder and equity holder in Hummingbird Scientific.

## References

- [ 1 ] Sekiba, T., Kimura, S., Yamamoto, H. & Okada, A. Development of automotive palladium three-way catalysts. *Catal. Today* **22**, 113–126 (1994).
- [ 2 ] Nishihata, Y. *et al.* Self-regeneration of a Pd-perovskite catalyst for automotive emissions control. *Nat.* **2002** *4186894* **418**, 164–167 (2002).
- [ 3 ] Lindlar, H. Ein neuer Katalysator für selektive Hydrierungen. *Helv. Chim. Acta* **35**, 446–450 (1952).
- [ 4 ] Luneau, M. *et al.* Guidelines to Achieving High Selectivity for the Hydrogenation of  $\alpha,\beta$ -Unsaturated Aldehydes with Bimetallic and Dilute Alloy Catalysts: A Review. *Chemical Reviews* vol. 120 12834–12872 (2020).
- [ 5 ] Luneau, M. *et al.* Achieving High Selectivity for Alkyne Hydrogenation at High Conversions with Compositionally Optimized PdAu Nanoparticle Catalysts in Raspberry Colloid-Templated SiO<sub>2</sub>. *ACS Catal.* **10**, 441–450 (2020).
- [ 6 ] Notar Francesco, I., Fontaine-Vive, F. & Antoniotti, S. Synergy in the Catalytic Activity of Bimetallic Nanoparticles and New Synthetic Methods for the Preparation of Fine Chemicals. *ChemCatChem* **6**, 2784–2791 (2014).
- [ 7 ] Jung, H., King, M. E. & Personick, M. L. Strategic synergy: advances in the shape control of bimetallic nanoparticles with dilute alloyed surfaces. *Curr. Opin. Colloid Interface Sci.* **40**, 104–117 (2019).
- [ 8 ] Ball, M. R. *et al.* AgPd and CuPd Catalysts for Selective Hydrogenation of Acetylene. *ACS Catal.* **10**, 8567–8581 (2020).
- [ 9 ] Zhang, Y. & Park, S. J. Stabilizing CuPd bimetallic alloy nanoparticles deposited on holey carbon nitride for selective hydroxylation of benzene to phenol. *J. Catal.* **379**, 154–163 (2019).
- [ 10 ] Liu, S. *et al.* Fabrication of palladium-copper nanoparticles with controllable size and chemical composition. *J. Colloid Interface Sci.* **526**, 201–206 (2018).
- [ 11 ] Krivanek, O. L. *et al.* Atom-by-atom structural and chemical analysis by annular dark-field electron microscopy. *Nat.* **2010** *4647288* **464**, 571–574 (2010).
- [ 12 ] Luneau, M. *et al.* Enhancing catalytic performance of dilute metal alloy nanomaterials. *Commun. Chem.* **3**, 1–9 (2020).
- [ 13 ] Kepp, K. P. A quantitative scale of oxophilicity and thiophilicity. *Inorg. Chem.* **55**, 9461–9470 (2016).
- [ 14 ] Huang, F. *et al.* Pd or PdO: Catalytic active site of methane oxidation operated close to stoichiometric air-to-fuel for natural gas vehicles. *Appl. Catal. B Environ.* **219**, 73–81 (2017).
- [ 15 ] Wu, P. *et al.* Formation of PdO on Au–Pd bimetallic catalysts and the effect on benzyl alcohol oxidation. *J. Catal.* **375**, 32–43 (2019).

# Accurate Quantification of $Q^n$ Species Distributions in Modified Silicate Glass by Phase Adjusted Spinning Sideband NMR Experiment

Lekhan Lodhi and Krishna Kishor Dey Dr. Harisingh Gour Central University

The 2D Phase Adjusted Spinning Sideband (PASS) sequence is applied here to quantify the distribution of  $Q^n$ , which denotes the number of bridging oxygens ( $n$ ) around a silicate tetrahedra, in a potassium disilicate glass. The relative concentrations of each  $Q^n$ -species were also measured and compared with previous MAF study on same glass composition. While MAF has been used in previous studies to improve the accuracy of  $Q^n$  species measurements in glasses, this technique requires a special probe capable of reorienting the rotor axis, making alternatives such as MAT or 2D PASS appealing since they can be implemented on a conventional MAS probe. Here we show that PASS experiment gives the same accuracy of MAF and it takes very less time compared to MAF experiment.

## Introduction

The coordination of silicon is commonly studied by  $^{29}\text{Si}$  MAS NMR, since silicon in a tetrahedral coordination with varying numbers of bridging oxygens ( $Q^n$  with  $n$  ranging from 0-4) can be separated on the basis of resonance shift, making it a powerful probe of atomic structure [1]. However, in disordered materials where a distribution of isotropic chemical shifts exists, lineshapes are complex due to large spectral overlap. NMR spectroscopists have generally avoided analyzing such data by unconstrained curve fitting because of the large uncertainties involved and doubts about the validity of Gaussian peak components. The concentration of  $Q^n$ -species can also be calculated by fitting the static NMR spectrum since the CSA parameters ( $\zeta$  and  $\eta$ ) for each  $Q^n$ -species varies significantly allowing multiple sites to be distinguished [2].

The full nuclear shielding tensor contains important information related to the structural details concerning the local bonding environment of a nuclei of interest. While the full tensor components can be obtained through acquisition of a static powder pattern, this approach suffers from low sensitivity since the integrated area of the line-shape is spread over a large frequency region. Sensitivity is somewhat improved in spinning samples because the intensity of the resulting spinning sideband pattern is related to the magnitude of the nuclear shielding anisotropy [3]. While the area of the sidebands for a given site is quantitative, differentiating between sidebands for multiple sites in a 1D NMR spectrum can be complicated. Therefore, to properly determine the nuclear shielding anisotropy for a system composed of multiple non-equivalent sites it is beneficial to use techniques such as Magic Angle Flipping (MAF) [4, 5], Magic Angle Hopping (MAH) [6], Magic Angle Turning (MAT) [7],

or 2D Phase Adjusted Spinning Sidebands (2D PASS) [8, 9] that correlate a high-resolution isotropic dimension to an anisotropic dimension to improve resolution. While MAF suffers from low sensitivity since magnetizations lost during the long hop delay during which time the magnetization is stored to Zeeman order, limiting its overall applicability to  $^{29}\text{Si}$  enriched samples and laboratories capable of performing variable angle experiments. For this reason, it is preferable to utilize a technique (MAT or 2D PASS) that provides complimentary information to MAF while improving sensitivity and can be implemented on a commercially available MAS probe.

In this study we have applied  $^{29}\text{Si}$  2D PASS NMR (**Figure 1**) to quantify  $Q^n$ -species distributions in potassium disilicate glass ( $\text{K}_2\text{O}\cdot 2\text{SiO}_2$ ). While 2D PASS has been utilized to determine chemical shift parameters [10, 11, 12, 13, 14] and bonding environments [15], studies using 2D PASS NMR to quantify the relative concentration of different sites are limited [16]. Here we show that same quantitative analysis can be obtained from 2D PASS and MAF methods. We demonstrate this on potassium disilicate glass and is compare to the previously reported results [17].

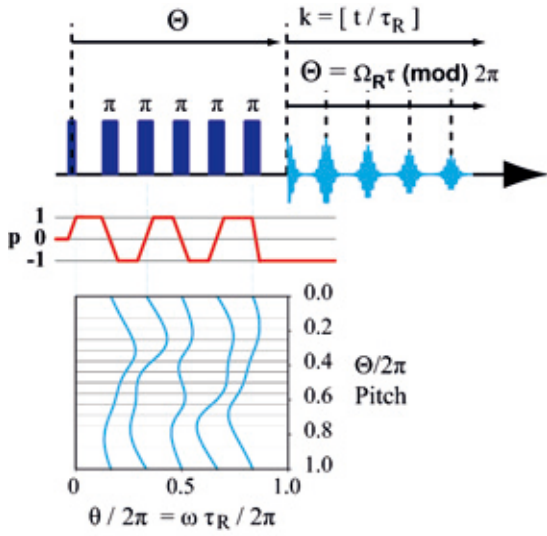
## 1. Experimental

### 1.1. Sample Preparation

Enriched sample was prepared from high purity  $\text{K}_2\text{CO}_3$  and 96%  $^{29}\text{Si}$ -enriched  $\text{SiO}_2$ . First  $\text{SiO}_2$  was heat treated at 600 °C for 5 h in order to remove protons present in the sample and was then kept in an argon filled glove box. The  $\text{K}_2\text{CO}_3$  was then decarbonated at 750 °C for 4 h and melted at 1300 °C. The melt was then quenched to room temperature by placing the bottom of the crucible into water. The NMR rotor was filled in argon filled glove box.



**Fig. 1**



2D PASS pulse sequence from Antzutkin et al. [9] where  $\Theta$  represents the rotor pitch and  $\Omega_R$  is the rotor spinning frequency.

## 1.2. Nuclear Magnetic Resonance Spectroscopy

All NMR experiments were conducted on a Spectrometer operating at a field strength of 9.7 T. The entire experiment was rotor synchronized to a sustained rotor frequency of 1 kHz  $\pm$  2 Hz. A shifted echo version of 2D PASS is utilized, where a delay of one rotor period ( $\tau_r$ ) is used prior to the fifth  $\pi$  pulse, which gives a full echo at  $3\tau_r$  for zero rotor pitch. The pulse sequence and coherence transfer diagram for the 2D PASS experiment proposed by Antzutkin et al. [9] is given in Figure 1. Each  $\pi$  pulse leads to an alternating coherence order between +1 and -1, where the timings between each pulse determines the phase of the acquired echo. While coherence transfer is 100% efficient for a perfect  $\pi$  pulses, pulse imperfections lead to finite coherence transfer between any of the three possible coherence pathways (+1, 0, -1) in an isolated spin-1/2 system. For an experiment involving five imperfect  $\pi$  pulses, the minimum number of required steps using a traditional nested phase cycle is 243, which leads to a very long experimental time particularly for samples with long  $T_1$ . All 2D PASS experiments on the  $^{29}\text{Si}$  potassium disilicate were carried out using an 11-step cogwheel phase cycle [18]. The  $T_1$  of this sample was 89 s and a relaxation delay of 6 min was used. A 32 steps PASS sequence was used. 11 scans were taken for each slice. The total experiment time for this experiment was 35.2 h. In the discussion we use following notations for defining full chemical shift tensor. The isotropic nuclear shielding is defined as the trace of the shielding tensor.

$$\delta_{iso} = \frac{1}{3}(\sigma_{xx} + \sigma_{yy} + \sigma_{zz}) \quad (1)$$

where  $\sigma_{xx}$ ,  $\sigma_{yy}$ , and  $\sigma_{zz}$  are the components of the nuclear shielding tensor in its principal axis system. The isotropic chemical shift,  $\delta_{iso}$ , is defined as

$$\delta_{iso} = (\sigma_{ref} - \sigma_{iso}) / (1 - \sigma_{ref}) \quad (2)$$

where  $\sigma_{ref}$  is the isotropic nuclear shielding of a reference compound, which is for this study is TMS. We adopt the Haeblerlen [19] convention, where

$$|\sigma_{zz} - \sigma_{iso}| > |\sigma_{yy} - \sigma_{iso}| > |\sigma_{xx} - \sigma_{iso}| \quad (3)$$

and the shielding anisotropy,  $\zeta$ , and asymmetry parameter,  $\eta$ , are

defined as

$$\zeta = \sigma_{zz} - \sigma_{iso} \quad (4)$$

and

$$\eta = \frac{\sigma_{yy} - \sigma_{iso}}{\zeta} \quad (5)$$

respectively.

The popular model [20, 21] for understanding the energetic and thermodynamic mixing properties of silicate melts involves disproportionation equilibrium between  $Q^{(n)}$  species.

$$2Q^{(n)} \rightleftharpoons Q^{(n-1)} + Q^{(n+1)} \quad (6)$$

with the equilibrium constant at glass transition temperature

$$k_n = \frac{[Q^{(n+1)}][Q^{(n-1)}]}{[Q^{(n)}]^2} \quad (7)$$

The value of equilibrium constant  $k_n$  ranges from 0 for a highly ordered (i.e., binary) distribution of  $Q^{(n)}$  species to  $k_3 = 0.375$ ,  $k_2 = 0.439$ , and  $k_1 = 0.311$  for a completely random distribution [22, 23].

## 1.3. Two-Dimensional Phase Adjusted Spinning Sideband (PASS) Experiment

For the 2D PASS experiment proposed by Antzutkin et al. [9] the frequency domain signal can be represented as

$$\Omega(t, \phi_0) = \sum_{l=0}^{\infty} \omega_{l,0}(\Omega_{PR}) + \sum_{l=0}^{\infty} \sum_{m \neq 0} \omega_{l,m}(\Omega_{PR}) e^{im(\Omega_R t + \phi_0)} \quad (8)$$

where  $\phi_0$  is the initial rotor phase,  $\Omega_R$  is the rotor spinning frequency,  $\omega_{l,0}(\Omega_{PR})$  are the isotropic components of the frequency, and  $\omega_{l,m}(\Omega_{PR})$  are the complex Fourier components depending upon the orientation  $\Omega_R = (\alpha_{PR}, \beta_{PR}, \gamma_{PR})$  of the principle axis system (PAS) of the CSA tensor with respect to a rotor system (R), where the  $z$  axis of R is fixed along the rotation axis. The phase at any time  $t$  can then be written as

$$\Phi(t, \phi_0) = \int_0^t \Omega(s) ds = W_{l,0} t + \sum_{m \neq 0} W_{l,m} [e^{im(\Omega_R t + \phi_0)} - e^{im\phi_0}] \quad (9)$$

where

$$W_{l,0} = \sum_{l=0}^{\infty} \omega_{l,0}(\Omega_{PR}) \quad (10)$$

and

$$W_{l,m} = \sum_{l=1}^{\infty} \frac{\omega_{l,m}(\Omega_{PR})}{im\Omega_R} \quad (11)$$

Following the approach first used by Dixon [8] and expanded by Antzutkin et al. [9], the phase can be manipulated using a series of  $\pi$  pulses at time  $\tau_j$  from the initial excitation pulse. In 2D PASS the signal must evolve in  $t_1$  as a function of rotor pitch so the signal phase is manipulated to have the form

$$\Phi_{PASS} = - \sum_{l,m \neq 0} iW_{l,m} e^{im\phi_0} [e^{im(\Omega_R t + \Theta)} - 1] \quad (12)$$

where  $\Theta$  is the applied rotor pitch. Since chemical shift anisotropy is a second rank tensor with  $l = 2$ , there are  $2l + 1$  possible values of  $m$  requiring at least five evolution periods separated by five  $\pi$  pulses. Writing the  $\pi$  pulse spacing in terms of pitch defined by  $\theta_j = \tau_j \Omega_R$ , and  $\theta_T = \Omega_R T$ , where  $T$  is the total PASS period, we can write the condition for PASS containing  $n$   $\pi$  pulses as

$$-(-1)^n e^{im(\Theta + \theta_T)} + 1 + 2 \sum_{j=1}^n (-1)^j e^{im\theta_j} = 0 \quad (13)$$



and

$$\theta_T + 2 \sum_{j=1}^n (-1)^{j+n} \theta_j = 0. \quad (14)$$

The real and imaginary part of the equation (13) and (14) contain a set of five nonlinear equations with  $n + 1$  unknowns ( $\theta_1, \dots, \theta_n$ ) and  $\theta_T$ . Setting  $n = 5$  the above equations can be solved numerically.

#### 1.4. Application of 2D $^{29}\text{Si}$ PASS to Silicate Glasses

While previous studies have utilized 2D PASS spectra to qualitatively analyze crystalline and disordered materials for different  $Q^{(n)}$  species, a full quantitative analysis has been lacking. To determine if 2D PASS can be used to quantify  $Q^{(n)}$  in an amorphous glass whose 1D NMR spectrum is completely unresolved we compare relative concentrations of  $Q^{(n)}$ -species in a  $^{29}\text{Si}$ -enriched potassium disilicate glass reported in a previous work [17] to those obtained by fitting a  $^{29}\text{Si}$  2D PASS NMR spectrum of the same material.

The PASS experiment avoids all the assumptions and gives the distributions of  $Q^n$  species in glass. **Figure 2** shows the correlations between isotropic and anisotropic dimensions. Unlike the isotropic dimension of  $2\text{Na}_2\text{O} \cdot 3\text{SiO}_2$  [22] glass where separate resonance for  $Q^{(2)}$  and  $Q^{(3)}$  are observed, here there is no clear resolutions of different species in isotropic dimension as seen in isotropic dimension of Figure 2. As shown in [22, 24] five different  $Q^{(n)}$  species have different shielding tensor value for  $^{29}\text{Si}$  resonance. As it can be seen from Figure 2 that -90 ppm is dominated by  $Q^{(3)}$ , -81.6 ppm is dominated by  $Q^{(2)}$  and -103.1 ppm is dominated by  $Q^{(4)}$  species. The anisotropic line shape for each site was modeled using four parameters: Isotropic chemical shift ( $\delta_{iso}$ ), shielding anisotropy ( $\zeta$ ), chemical shift asymmetry ( $\eta$ ), and integrated intensity. A 3 ppm difference in  $\zeta$  was observed for  $Q^{(3)}$  (-77.8 ppm) and  $Q^{(2)}$  (-88.9 ppm) between 2D PASS experiments presented in this work and previous MAF studies [17] attributed to differences in experimental

conditions (spinning speed, angular dependencies, etc.), while  $\eta$  values were identical ( $\eta = 0.08$  and  $0.46$  for  $Q^{(3)}$  and  $Q^{(2)}$  respectively). For  $Q^{(4)}$   $\zeta$  and  $\eta$  were set to zero. Spectra were fit using a 2D fitting routine utilizing the NMR simulation package SIMPSON [25] and the Levenberg-Marquardt algorithm built into the Optimization toolbox of Matlab. In this way, the full 2D spectrum could be fit and relative concentrations of each  $Q^{(n)}$ -species obtained. This procedure was employed to fit the  $^{29}\text{Si}$  2D PASS (Figure 2a) spectra of the  $^{29}\text{Si}$ -enriched potassium disilicate glass and the relative areas used to reconstruct a 1D lineshape to easily visualize the relative contributions of each  $Q^{(n)}$ -species to the full 2D spectrum (**Figure 3a, Table 1**).

The measured concentrations from 2D PASS is within 2% of the previously reported  $k_3$  from MAF (Table 1), indicating that 2D PASS can be utilized similar to MAF to quantify  $Q^{(n)}$ -species in silicate glasses. Since the 2D PASS technique can be performed on a standard MAS probe by spinning at a fixed angle this should offer a significant time savings over variable angle experiments allowing these experiments to be more readily performed in most NMR labs.

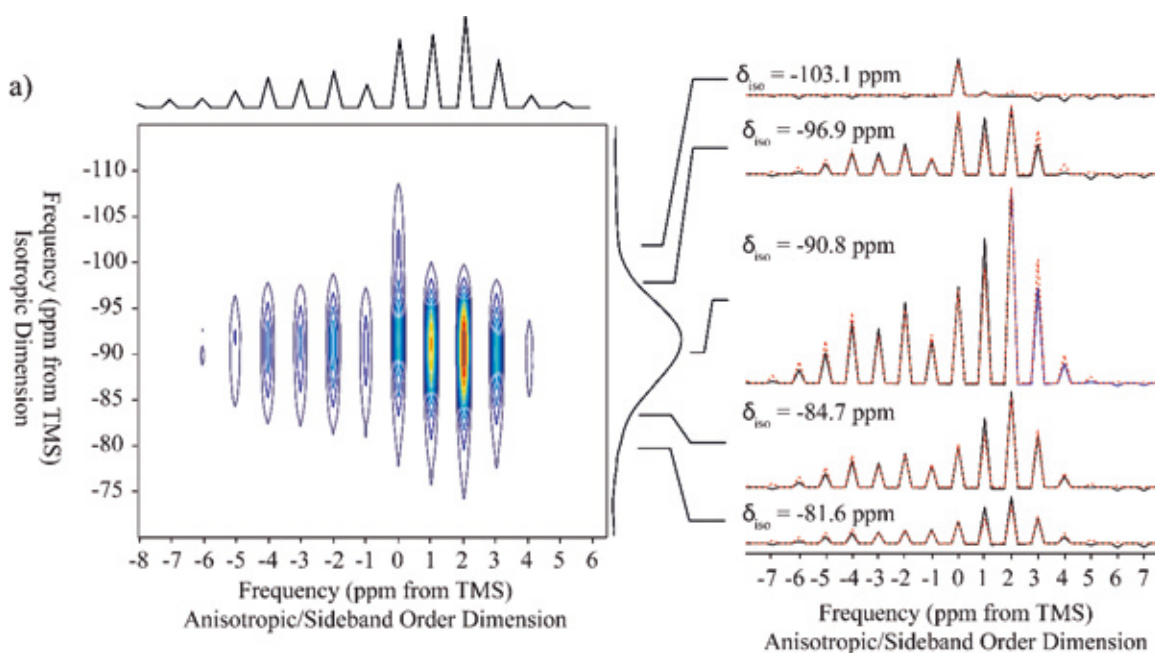
#### Summary

MAF method has been extensively used to quantify  $Q^n$  species distributions in silicate glass. Although it gives more accurate quantitative information than simple deconvolution of MAS spectra, but it is very time consuming and takes special probe design, so this method has not gained much popularity. Here for the first time, we quantitatively compare 2D PASS results with published MAF data. Our data agrees within 2% with the MAF results.

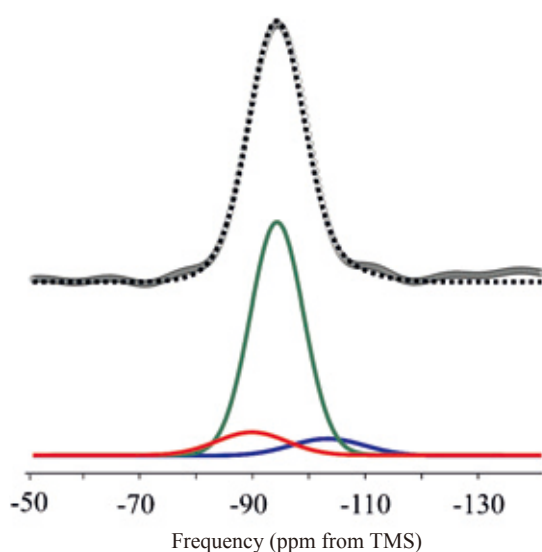
#### References

- [ 1 ] K. A. Smith, R. J. Kirkpatrick, E. Oldfield, D. M. Henderson, High-resolution Si-29 nuclear-magnetic-resonance spectroscopic study of rock-forming silicates, *Chemical Physics letter* **68** (1983) 1206–1215.

**Fig. 2**



The  $^{29}\text{Si}$  a) 2D PASS NMR spectrum of the  $^{29}\text{Si}$ -enriched potassium disilicate glass. Representative cross sections along the sideband dimension are provided where solid lines represent experimental spectra and dashed lines represent the least-squares fit simulation.

**Fig. 3**

Reconstructed 1D lineshape from the deconstruction of the a) 2D PASS NMR spectrum of the  $^{29}\text{Si}$ -enriched potassium disilicate glass. Each of the three Gaussians represent the relative contributions from  $\text{Q}^{(2)}$ ,  $\text{Q}^{(3)}$ , and  $\text{Q}^{(4)}$ , circles represent the 1D projection along the MAS dimension, and dashed lines are the total least squares best fit.

**Table 1**

Site	Relative Area	Mean Position/ ppm	Standard Deviation/ ppm
MAS <sup>†</sup>			
$\text{Q}^{(2)}$	$41.6 \pm 3.3\%$	$-87.55 \pm 0.11$	$5.15 \pm 0.03$
$\text{Q}^{(3)}$	$57.7 \pm 2.7\%$	$-92.24 \pm 0.02$	$3.88 \pm 0.01$
$\text{Q}^{(4)}$	$0.7 \pm 4.7\%$	$-104.83 \pm 0.10$	$1.92 \pm 0.08$
MAF <sup>†</sup>			
$\text{Q}^{(2)}$	$9.8 \pm 0.7\%$	$-82.74 \pm 0.03$	$3.27 \pm 0.03$
$\text{Q}^{(3)}$	$83.0 \pm 0.1\%$	$-91.32 \pm 0.01$	$4.19 \pm 0.01$
$\text{Q}^{(4)}$	$7.2 \pm 0.3\%$	$-101.67 \pm 0.02$	$5.09 \pm 0.03$
2D PASS			
$\text{Q}^{(2)}$	$8.7 \pm 0.2\%$	$-79.7 \pm 0.2$	$3.89 \pm 0.09$
$\text{Q}^{(3)}$	$84.5 \pm 0.2\%$	$-90.6 \pm 0.2$	$4.43 \pm 0.02$
$\text{Q}^{(4)}$	$6.6 \pm 0.1\%$	$-98.0 \pm 0.1$	$7.73 \pm 0.09$

Gaussian distribution parameters of isotropic chemical shifts of  $\text{Q}^{(n)}$ -species in  $^{29}\text{Si}$ -enriched  $\text{K}_2\text{O}\cdot 2\text{SiO}_2$  derived from analysis of  $^{29}\text{Si}$  MAS<sup>†</sup>,  $^{29}\text{Si}$  MAF<sup>†</sup>,  $^{29}\text{Si}$  2D PASS spectra, where<sup>†</sup> indicates experimental results reported in a previous work [17].

[ 2 ] J. F. Stebbins, Identification of multiple structural species in silicate glasses by  $^{29}\text{Si}$  NMR, *Nature* **330** (1987) 465.  
 [ 3 ] J. Herzfeld, A. E. Berger, Sideband intensities in NMR spectra of samples spinning at the magic angle, *J. Chem. Phys.* **73** (1980) 6021.  
 [ 4 ] Bax, N. M. Szeverenyi, G. E. Maciel, Correlation of isotropic shifts and chemical shift anisotropies by two dimensional Fourier-transform magic-angle hopping NMR spectroscopy, *J. Magn. Reson.* **52** (1983) 147.  
 [ 5 ] P. J. Grandinetti, J. H. Baltisberger, A. Llor, Y. K. Lee, U. Werner, M. A. Eastman, A. Pines, Pure absorption-mode lineshapes and sensitivity in two-dimensional dynamic angle

spinning NMR, *J. Magn. Reson.* **A 103** (1993) 72–81.

[ 6 ] J. Z. Hu, D. W. Alderman, C. H. Ye, R. J. Pugmire, D. M. Grant, An isotropic chemical shift-chemical shift anisotropy magic-angle slow-spinning 2D NMR experiment, *J. Magn. Reson.* **A 105** (1) (1993) 82–87.  
 [ 7 ] Z. H. Gan, High-resolution chemical-shift and chemical-shift anisotropy correlation in solids using slow magic-angle spinning, *J. Am. Chem. Soc.* **114** (21) (1992) 8307–8309.  
 [ 8 ] W. T. Dixon, Spinning-sideband-free and spinning-sideband only NMR spectra in spinning samples, *J. Chem. Phys.* **77** (1982) 1800.  
 [ 9 ] O. N. Antzutkin, S. C. Shekar, M. H. Levitt, Two-dimensional sideband separation in magic-angle spinning NMR, *J. Magn. Reson.* **A 115** (1995) 7–19.  
 [ 10 ] M. S. Ironside, R. S. Stein, M. J. Duer, Using chemical shift anisotropy to resolve isotropic signals in solid-state NMR, *Journal of Magnetic Resonance* **188** (2007) 49–55.  
 [ 11 ] M. S. Ironside, D. G. Reid, M. J. Duer, Correlating sideband patterns with powder patterns for accurate determination of chemical shift parameters in solid-state NMR, *Magnetic Resonance in Chemistry* **46** (2008) 913–917.  
 [ 12 ] F. G. Vogt, J. M. Gibson, D. J. Aurentz, K. T. Mueller, A. J. Benesi, Multiple-rotor-cycle 2D PASS experiments with applications to  $^{207}\text{Pb}$  spectroscopy, *Journal of Magnetic Resonance* **143** (2000) 153–160.  
 [ 13 ] F. Song, O. N. Antzutkin, A. Rupprecht, M. H. Levitt, Order resolved sideband separation in magic-angle-spinning nmr.  $^{31}\text{P}$  NMR of oriented DNA fibers, *Chemical Physics Letters* **253** (1996) 349–354.  
 [ 14 ] Y. Wei, D. Lee, A. Ramamoorthy, Solid-state  $^{13}\text{C}$  NMR chemical shift anisotropy tensors of polypeptides, *Journal of the American Chemical Society* **123** (2001) 6118–6126.  
 [ 15 ] F. Fayon, C. Bessada, A. Douy, D. Massiot, Chemical bonding of lead in glasses through isotropic vs anisotropic correlation: Pass shifted echo, *J. Magn. Reson.* **137** (1999) 116–121.  
 [ 16 ] B. Cherry, J. W. Zwanziger, B. G. Aitken, The structure of  $\text{GeS}_2\text{-P}_2\text{S}_5$  glasses, *Journal of Physical Chemistry B* **106** (2002) 11093–11101.  
 [ 17 ] M. Davis, D. Kaseman, S. Parvani, K. Sanders, P. Grandinetti, P. Florian, D. Massiot,  $\text{Q}^{(n)}$ -species distribution in  $\text{K}_2\text{O}\cdot 2\text{SiO}_2$  by  $^{29}\text{Si}$  Magic Angle Flipping NMR, *J. Phys. Chem. A* **114** (17) (2010) 5503–5508.  
 [ 18 ] N. Ivchenko, C. E. Hughes, M. H. Levitt, Application of cogwheel phase cycling to sideband manipulation experiments in solid-state nmr, *Journal of Magnetic Resonance* **164** (2003) 286–293.  
 [ 19 ] R. K. Harris, E. D. Becker, S. M. C. D, P. Grangerd, R. E. Hoffman, K. W. Zilm, *Inorg. Chem.* **3** (2008) 41–56.  
 [ 20 ] G. N. Greaves, S. J. Gurman, C. R. A. Catlow, A. V. Chadwick, S. Houde-Walter, C. M. B. Henderson, B. R. Dobson, *Philos. Magn.* **A 64** (1991) 1059–1072.  
 [ 21 ] M. D. Ingram, *Philos. Magn.* **B 60** (1989) 729.  
 [ 22 ] P. Zhang, C. Dunlap, P. Florian, P. J. Grandinetti, I. Farnan, J. F. Stebbins, *J. Non-Cryst. Solids* **204** (1996) 294–300.  
 [ 23 ] E. D. Lacy, *Phys. Chem. Glasses* **6** (1965) 171–180.  
 [ 24 ] P. Zhang, P. J. Grandinetti, J. F. Stebbins, *J. Phys. Chem. B* **101** (1997) 4004–4008.  
 [ 25 ] M. Baks, J. T. Rasmussen, N. C. Nielsen, SIMPSON: A general simulation program for solid-state NMR spectroscopy, *J. Magn. Reson.* **147** (2000) 296–330.

# Electron Cryomicroscopy: Recent Progress and Future Perspective for Structural Life Sciences

Keiichi Namba<sup>1,2</sup> and Fumiaki Makino<sup>1,3</sup>

<sup>1</sup> Graduate School of Frontier Biosciences, Osaka University, <sup>2</sup>RIKEN SPring-8 Center, <sup>3</sup>JEOL Ltd.

The three-dimensional (3D) structure of biological macromolecules such as proteins and nucleic acids is essential and fundamental information not only for life sciences but also for medical sciences and drug discovery. X-ray crystallography and NMR have been the core technologies for structural determination in structural biology, but electron cryomicroscopy (cryoEM) has largely surpassed its role as a complement to them and has now become an extremely powerful tool as the fundamental method for high-resolution structural analysis of biomacromolecules and their complexes. The development of hardware and software, including electron cryomicroscopes equipped with highly stable and controllable electron optics, cold field emission electron guns, energy filters, and high frame rate, high sensitivity CMOS-type direct electron detection cameras, as well as high-speed computers and image analysis software, has enabled the 3D structures of biomacromolecules to be determined within a few days even from a few  $\mu\text{g}$  of aqueous sample solutions. How is it possible to visualize the 3D structures of biomacromolecules, which are damaged by irradiation of an electron beam even at relatively low dose? In this article, we discuss recent advances in cryoEM and future perspective on its contributions to life/medical sciences and drug discovery.

## Introduction

The basic mechanisms that drive and support complex biological activities are common from microorganisms such as bacteria and yeast to multicellular organisms such as animals and plants, and even to humans with higher brain functions. Every biological function is determined by the structures and dynamics of biological macromolecules such as proteins and nucleic acids and their highly complex and dynamic interaction networks. The structures of biomacromolecules are determined by the three-dimensional (3D) arrangements of their numerous constituent atoms, which number from thousands to tens and hundreds of thousands, but they are not as rigid as those of metals or ceramics. They are dynamic and flexible because it is weak non-covalent bond networks that hold them in place. Biomacromolecules are designed to function actively with thermal fluctuations, thus allowing organisms to sustain their activities at extremely low energy levels compared to artificial machines. One of the major challenges in life science is to elucidate the mechanisms of complex biological functions based on the structures, dynamics, and interactions of biomacromolecules, which requires visualization of the structures of numerous biomacromolecules involved in various biological functions and their stable or transient complexes they form in various functional states. The number of 3D structures we need to visualize would range from a few millions to a few hundreds of millions or possibly many more. However, X-ray

crystallography and NMR, which have long been the core techniques in structural biology, are limited by their stringent requirement that samples be crystallized or that the molecular mass be less than 50 kDa, respectively. By recent remarkable progress, cryoEM has established itself as the major and core technique for the structural analysis of macromolecules and their complexes and is attracting much attention because it enables atomic resolution structural analysis even from aqueous solution samples of only a few  $\mu\text{g}$ . No crystallization is required and there is almost no upper limit in the sample size. The 2017 Nobel Prize in Chemistry was awarded to three pioneers of this technique for their important contributions. In this article, we describe an overview of cryoEM single particle image analysis as a structural analysis method, history of its progress, and the current state of technological development, including our own experience in the development and application of the technique, as well as its future potential for life sciences, medical sciences, and drug discovery through further technological advances.

## CryoEM single particle image analysis

The powerful feature of cryoEM, especially single particle image analysis, is characterized by the fact that sample crystallization is not required and there is almost no upper limit in the sample size. What is needed for structural life science is a method that can visualize numerous structures of biomacromolecules and their complexes in their different



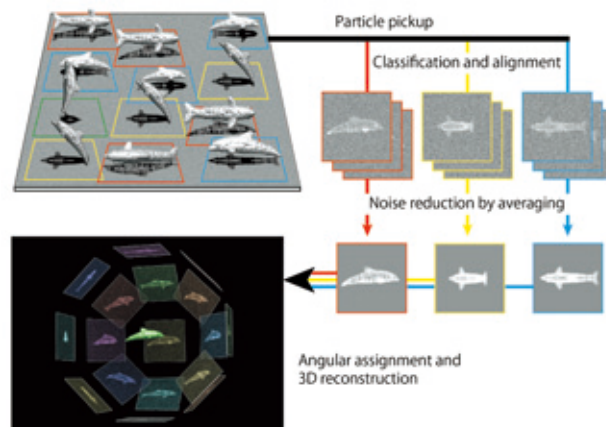
functional states that can never be analyzed by X-ray or NMR. CryoEM has made it possible.

Most of the atomic bonds that maintain the 3D structures of biomacromolecules and their complexes are weak non-covalent bonds such as hydrogen bonds, salt bridges, and van der Waals forces that generate hydrophobic interactions, and they are very sensitive to electron irradiation. Therefore, to record high-resolution cryoEM images in their native, functional conformations without significant damage, it is necessary to quickly freeze their aqueous solutions, embed them in an amorphous thin ice film, and record their cryoEM images with a transmission electron cryomicroscope (cryoTEM) with a specimen stage cooled below 100 K with liquid helium or liquid nitrogen. The lower the temperature, the less electron irradiation damage [1], but at temperatures below 20 K, image drift is likely to occur due to charge-up or other causes due to the low electron conductivity of ice and carbon on the frozen sample grid [2]. Even at such low temperatures, the electron dose that can be irradiated without causing significant damage to the structure is limited to 20-30  $e/\text{\AA}^2$ . The quality of cryoEM images is extremely poor due to the inherent statistical noise caused by the small number of electrons detected in each pixel of the camera and the Landau noise generated by the large distribution of signal levels of individual electrons detected by the camera. Furthermore, since cryoEM images are two-dimensional (2D) projections of a 3D structure of the sample molecule embedded in a thin ice film in various orientations, it is necessary to collect enough number of molecular images that uniformly cover the projection directions in order to reconstruct a 3D image with high resolution in all directions. Therefore, it is essential to efficiently collect as many molecular images as possible, classify them by their orientations, align the position and orientation of each molecular image, and obtain an averaged image for each orientation to increase the signal level while reducing the noise. This procedure is called 2D class averaging. The relative relationships between the projection directions are then obtained, and finally the 3D image of the molecule can be reconstructed (Fig. 1, cited from [2]). To achieve high-resolution structural analysis, it is essential to use cryoTEMs and cameras that can rapidly and efficiently collect high-quality, high-resolution cryoEM images. High-precision image analysis programs and high-speed computers are also necessary.

## CryoTEM with liquid helium stage and thermal FEG

In the 1980s, Fujiyoshi, together with JEOL, designed and developed a liquid helium-cooled sample stage that minimizes radiation damage for high-resolution cryoEM imaging [3, 4]. In 1994, Fujiyoshi and Namba set up a new laboratory in the newly established Panasonic Research Institute in Keihanna Science City and asked JEOL to develop a liquid helium-cooled cryoTEM (JEOL JEM-3000SFF) equipped with a Schottky-type field emission electron gun (thermal FEG) (Fig. 2). This was the world's first FEG-equipped cryoTEM [2, 4], and the highly coherent electron beam by field emission had significantly improved the image quality and resolution of cryoEM images [5-10]. High-resolution 3D density maps were obtained for the structures of the bacterial flagellar filament and tubular crystals of nicotinic acetylcholine receptor channel, which enabled atomic models to be built [6, 7]. 2D crystals of membrane proteins such as bacteriorhodopsin and aquaporin were analyzed at near-atomic resolution by electron crystallography combining imaging and diffraction [8-10]. Because the image detector was

**Fig. 1 Schematic diagram explaining the process of single particle image analysis.**



Dolphins represent biological macromolecules embedded in a thin film of vitreous ice in various orientations. CryoEM images correspond to their 2D projections with high noise levels. After the S/N is greatly increased by going through 2D classification and average of many 2D projections, a 3D image can be reconstructed by back projection. Adopted from [2].

photographic films, the efficiency and throughput of high-quality image data collection was extremely low, and it took more than several years for these structural analyses to reach near-atomic resolution, but many high-impact results were published in the early to mid-2000s [6-10]. The structure of the bacterial flagellar filament by cryoEM helical image analysis reached a resolution of nearly 4  $\text{\AA}$  from a relatively small number of images containing only 40,000 flagellin molecules, where the polypeptide main chain and large side chains were successfully resolved for the first time by cryoEM image analysis [6].

## CCD detectors and energy filters

The development of automated image data collection methods by using CCD detectors began in the late 1990s [11-14], but most research groups continued to use photographic films through 2000s because the resolving power of CCD was significantly lower than that of photographic film. The low resolution of CCD was due to the blurring of each electron spot caused by electron scattering on the thin scintillator layer that converts electrons to photons. That is why CCDs were used mainly for recording electron diffraction and rarely for imaging in those days. Nevertheless, the ability to evaluate image quality on a display immediately after imaging was a great advantage for efficient data collection, so we utilized a CCD detector to improve the efficiency of cryoEM image data collection. We also considered that an energy filter would be effective in improving the signal-to-noise ratio (S/N) of cryoEM images by removing most of electrons that lost energy and coherence by inelastic scattering from the sample and contribute only to the background noise. We requested JEOL to equip a 300 kV liquid helium-cooled cryoTEM (JEOL JEM-3200FSC) with a  $4\text{ k} \times 4\text{ k}$  slow-scan CCD (TVIPS F415MP) and an  $\Omega$ -type in-column energy filter (Fig. 2). This cryoTEM was installed in a new research building at Osaka University in 2004. Evaluation



of cryoEM images showed that the energy filter alone improved the S/N by nearly a factor of 2 and markedly increased the collection efficiency of high quality cryoEM images [15]. In addition, by stopping the liquid helium flow into the sample pod and increasing the temperature from 4 K to 50 K, the efficiency of high-quality image data collection was further improved. At a sample temperature of 4 K, irradiation damage was minimized but most of the cryoEM images showed local image drift due to charge up, and only a few percent or less of the images could be used for image analysis. These technological advances enabled a multi-year structural analysis project to be completed in a week or two and allowed us to determine a number of interesting structures of biomolecular complexes at 5 - 7 Å resolution, visualizing the secondary structures [15-20]. In the structure of the stack disk of tobacco mosaic virus coat protein, 3.8 Å resolution was achieved and many side chains were visualized (Fujii et al., unpublished).

### CMOS direct electron detectors

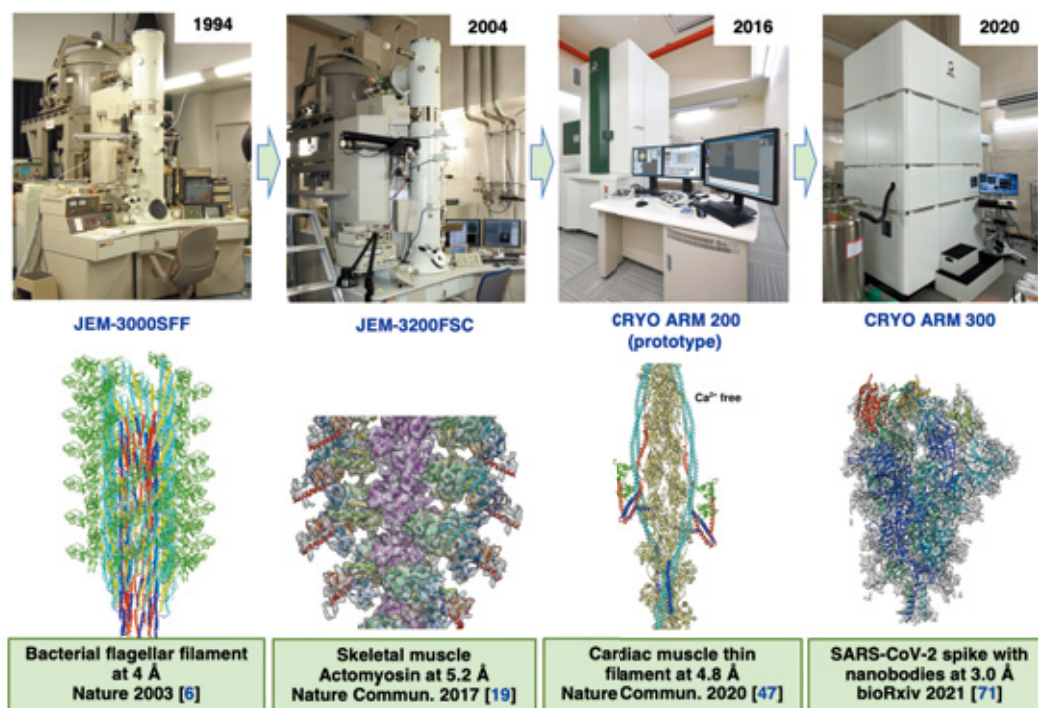
In 2013, a CMOS-based direct electron detection camera was introduced and dramatically improved the resolution of cryoEM structural analysis [21]. In collaboration with a camera manufacturer, Gatan, Agard at UCSF converted a CMOS sensor for X-ray developed at UC Berkeley to a cryoEM image sensor. Gatan made this camera commercially available, and the 4 k × 4 k pixel CMOS camera named K2 Summit had a high sensitivity, low blurring due to electron scattering, and an image acquisition rate of 400 frames/second, which enabled single electron detection and movie-mode imaging. Cheng and colleagues at UCSF have taken full advantage of the performance of this

CMOS camera to develop a method to capture high-resolution cryoEM images [21]. They successfully solved the structure of TRPV1 thermoreceptor ion channel, a membrane protein that eluded crystallization over many years, at high resolution and published two papers in Nature [22, 23]. The structure was solved at 3.3 Å resolution by extracting approximately 100,000 particle images of the detergent-solubilized membrane protein picked up from about 1,000 cryoEM images. This was the beginning of the revolutionary breakthrough of cryoEM called the “resolution revolution”. Since then, the highest resolution as well as the average resolution has shown steady improvement every year due also to the improved accuracy of image analysis software such as MotionCor2, CTFFIND4, gctf, RELION, and cryoSPARC [24-29], etc. The highest resolution record has been updated every year as follows: 3.2 Å for β-galactosidase in 2014 [30]; 2.6 Å for rotavirus in 2015 [31]; 2.2 Å for β-galactosidase in 2015 [32]; 1.8 Å for glutamate dehydrogenase in 2016 [33]; 1.65 Å and 1.62 Å for apoferritin in 2018 [28, 34]; 1.53 Å for apoferritin in 2019 [35]; and 1.25 Å and 1.22 Å for apoferritin in 2020 [36, 37]. Even individual atoms are clearly visualized at these highest resolutions better than 1.3 Å.

### Cold FEG and monochromator

One of the important factors that determines the resolution of EM images is the coherence of the electron beam, the higher the coherence, the higher the resolution. To improve the coherence, it is necessary to reduce the size of the electron source on the gun tip and the energy width of the electron beam. The resolutions of 1.5 Å [35] and those around 1.2 Å [36, 37] were achieved by cryoTEMs equipped either with cold FEG

**Fig. 2 Development history of cryoTEMs in our laboratory.**



From left to right: JEM-3000SFF with liquid helium stage and thermal FEG; JEM-3200FSC with Ω-type energy filter and TVIPS F415mp CCD detector, in addition to liquid helium stage and thermal FEG; CRYO ARM™ 200 prototype with liquid N<sub>2</sub> stage, cryo-grid autoloader, JADAS-based automated data collection and Gatan K2 CMOS detector, in addition to thermal FEG and Ω-type energy filter; CRYO ARM™ 300 with cold FEG, upgraded Ω-type energy filter, Gatan K3 detector and SerialEM-based high-throughput automated data collection, in addition to liquid N<sub>2</sub> stage and cryo-grid autoloader. Lower panels show example structures determined by the cryoTEMs above.

or thermal FEG combined with a monochromator. Kato et al. [35] and Nakane et al. [37] used cold FEG-equipped cryoTEMs with source sizes of 5-10 nm and an energy width of about 0.35 eV, while Yip et al. used a thermal FEG cryoTEM with a monochromator and a spherical aberration corrector to narrow the energy width to 0.1 eV [36]. Thus, cryoEM has become a fundamental technology that plays an extremely important role in life sciences, medicine, and drug discovery by its capability of visualizing even the positions of hydrogen atoms in proteins, elucidating the physicochemical reaction mechanisms of proteins, and improving the accuracy and efficiency of structure-based drug discovery. Achieving a resolution beyond 1 Å by combining cold FEG and monochromator is no longer a distant dream.

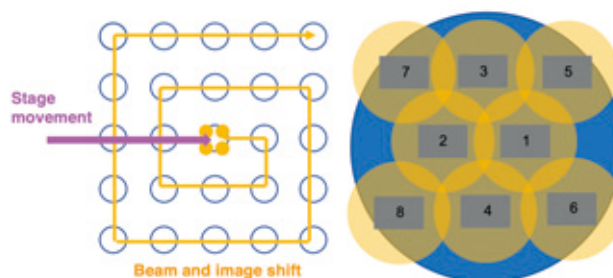
### High-throughput data collection

Now that the resolution of cryoEM structural analysis has reached the atomic level and that many of the results are equivalent to the average resolution of 2 Å in X-ray crystallography, one of the remaining issues is the speed and full automation of data collection. The development of high-performance, easy-to-use cryoTEMs equipped with an automated cryo-grid loading device and automated imaging technology began in the 2010s, but it was not until the latter half of the 2010s that the data collection speed was significantly improved. In cryoEM imaging, frozen-hydrated biomacromolecules are imaged with those embedded in an amorphous ice film of several tens of nanometers thick in each of micron-sized holes regularly arranged on the holey carbon film on the EM grid. In the conventional imaging method, the sample stage is moved for every shot to align the optical axis of the electron beam with each hole, resulting in an extremely slow data collection speed as it takes several tens of seconds to wait for the drift to subside after the stage movement. With CCD cameras, which require several tens of seconds for data acquisition, the data collection rate was about 500 images per day, and even with CMOS cameras, which are much faster in data acquisition, the rate remained at 1,000 to 1,500 images per day until 2018 [38]. Recently, however, multi-spot imaging utilizing beam tilt and image shift has become a standard, and images of multiple holes around the electron optics axis ( $3 \times 3$  or  $5 \times 5$ ) can be captured without moving the sample stage. When the magnification is large enough, multi-shot imaging within each hole can also be used to achieve an even higher speed (Fig. 3) [39-42]. As a result, the data acquisition rate has been remarkably increased without sacrificing high-resolution information, having enabled collection of 7,000 images per day (250 images/hour) in 2019, 23,000 images per day (1,000 images/hour) in 2020, and 30,000 images per day (1,300 images/hour) in 2021 (Fig. 4) [43-45].

This technology was developed with Titan Krios of Thermo Fisher Scientific and CRYO ARM™ 300 of JEOL to increase the imaging throughput. CRYO ARM™ is a cryoTEM we have been developing with JEOL since 2010. It is based on JEM-ARM200F, a high-resolution TEM for materials research, to aim at automation, high throughput and high resolution in cryoEM imaging. The combination of a high-resolution electron optics and an  $\Omega$ -type in-column energy filter that minimizes the background noise due to inelastic scattered electrons, together with a newly developed computer-controlled liquid nitrogen-cooled sample stage and an automatic cryo-grid loading system, has made it a highly efficient and easy-to-use cryoTEM for collecting high-resolution data. The  $\Omega$ -type energy filter is also useful for measuring the thickness of ice films, which is very

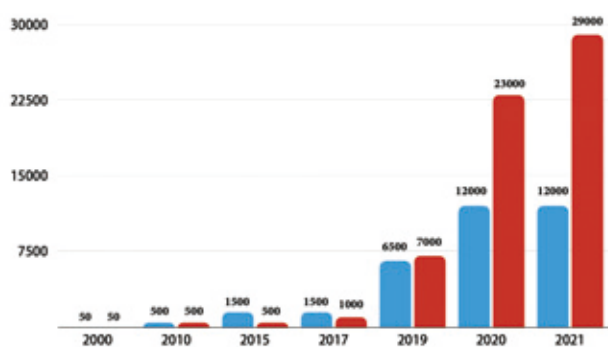
convenient for judging the quality of cryo-grids. The prototype of CRYO ARM™ with an acceleration voltage of 200 kV was equipped with thermal FEG and Gatan K2 camera and was installed at Osaka University in early summer of 2016. It then took nearly a year to fix hardware and software bugs (Fig. 2), but once it started its stable operation in 2017, it demonstrated

**Fig. 3 Procedure of multi-hole/multi-shot imaging by beam tilt and image shift.**



Multi-hole imaging records cryoEM images in surrounding holes ( $5 \times 5$  in this case) by beam tilt and image shift without stage movement in the order as indicated by the yellow arrow (left). In addition to this, multi-shot imaging records multiple cryoEM images within each hole. In the case of zero-fringe mode (right), it is possible to take 8 images within a single hole even with a 1.2  $\mu\text{m}$  hole of the Quantifoil R1.2/1.3 holey carbon grid.

**Fig. 4 History of improvement in cryoEM data collection throughput.**



Year	CryoTEM	Detector	Data collection method
2000	JEM3000SFF	Photographic film	Manual
2010	JEM3200FSC	TVIPS F415mp	Manual
2017	CRYO ARM 200 (prototype)	GATAN K2	JADAS
2019	CRYO ARM 300	GATAN K3	SerialEM
2020	CRYO ARM 300	GATAN K3	SerialEM & PyJEM
2021	CRYO ARM 300 II	GATAN K3	SerialEM & PyJEM & Zero-fringe

The bar graphs show the maximum numbers of images that can be collected per day in each record update year indicated at the bottom. The blue bars represent the record by TFS cryoTEMs [38, 39, 41, 42], and the red bars represent those by JEOL cryoTEMs in our laboratory. CryoTEMs, detectors, and data collection methods used for data collection are listed in the bottom table [2, 6, 11]. The throughputs of 50 per day in 2000 and 500 per day in 2010 are rough estimates around those time.

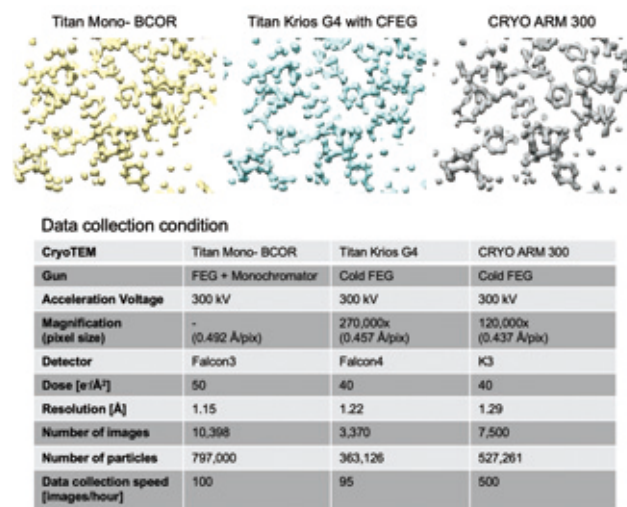


its power and contributed to the structural analyses of many biologically important protein complexes, including the native supercoiled bacterial flagellar hook acting as a universal joint [46], human cardiac muscle thin filament in the presence and absence of  $\text{Ca}^{2+}$  that revealed the molecular mechanism of heart beat [47], and the bacterial flagellar LP ring as a nearly frictionless bushing of the rotary motor [48]. The resolution was further improved with the commercial versions of CRYO ARM™ released in 2017 because they were all equipped with cold FEG. In 2019, CRYO ARM™ 300 equipped with a Gatan K2 detector achieved 1.53 Å resolution for apoferritin from approximately 1,000 cryoEM images collected over a day [35]. In 2020, an improved version of CRYO ARM™ 300 equipped with a Gatan K3 detector and a new high-precision chiller was installed at Osaka University. We used this cryoTEM to establish an automated data collection workflow and speed up the imaging rate by multi-hole, multi-shot imaging by developing a TEM control software, utilizing PyJEM, a python library for JEOL's TEM system control, and SerialEM [49]. A dramatic speed-up to 30,000 images/day was achieved in 2021 as described above (Fig. 4). For a typical protein sample, several thousands of cryoEM image data are required for high-resolution structural analysis, and it used to take several days to collect such a dataset. But now CRYO ARM™ 300 allows multiple datasets to be collected in one day, and this has made it practical for pharmaceutical companies to carry out structure-based drug screening. This was also useful for us in solving multiple structures of the bacterial flagellar rotor ring within a short time of period [50]. Even atomic-resolution structural analysis is possible in such fast data acquisition by minimizing coma aberration due to the beam tilt to preserve high-resolution information (Fig. 5). In the test data collection and analysis of apoferritin, 1.29 Å resolution was achieved from 7,500 images collected in 15 hours [51]. Since the number of images required to achieve a resolution in the 1.2 Å range with apoferritin is generally less than half of this [43, 44], it implies that data collection for atomic-resolution structural analysis can be easily accelerated by 2-fold or more and can be completed within a few hours.

## Potential for sub-Å resolution

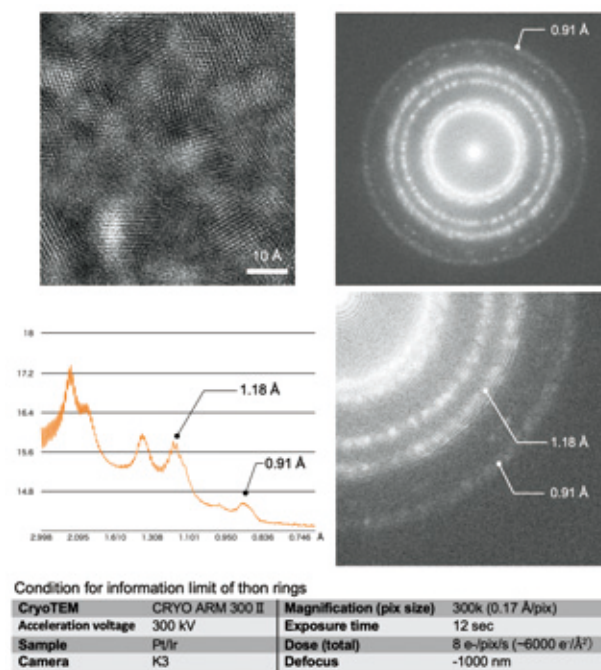
Now that atomic-resolution structural analysis of the apoferritin structure is no longer a rarity, the achievement of sub-Å resolution by the combination of cold FEG and monochromator is not a distant dream. But even recent state-of-the-art cryoTEMs with excellent electron optical system and sample stage stability may be able to exceed 1 Å resolution. One of the standard methods to examine the resolution attainable by a cryoTEM is to image thin film samples of metals such as amorphous platinum-iridium alloys (Pt/Ir) with a defocus of about 1 μm as for cryoEM imaging of protein and to check the extension of the Thon ring in the Fourier image (Fig. 6). In the Pt/Ir image taken by 300 kV cryoTEMs with thermal FEG, the Thon ring disappears at about 1.8 Å [52], but it extended to 1.1 Å by CRYO ARM™ 300 with cold FEG [2]. Interestingly, by the second generation CRYO ARM™ 300 II, the resolution further increased to 0.9 Å (Fig. 6), which is a significant improvement that could not have been simply predicted by the hardware design. In any case, this is quite promising toward achieving the goal of sub-Å resolution structural analysis. It would be possible to visualize protein structures at a resolution beyond 1.0 Å if such high-resolution imaging conditions are satisfied.

**Fig. 5 Comparison of three cryoTEMs that achieved atomic resolution.**



The upper panels show part of the 3D density maps of apoferritin. The names of three cryoTEMs and data collection conditions are listed in the lower panel.

**Fig. 6 Evaluation of information limit of CRYO ARM™ 300 II by Thon rings of Pt/Ir.**



Upper left is a cryoEM image of Pt/Ir at 300 k magnification. Upper right is the Fourier transform showing the Thon rings extending to 0.91 Å. Lower left is one-dimensional profile of the Thon rings. High-resolution peaks at 1.18 Å and 0.91 Å are indicated. Lower right is a magnified image of upper right panel. The table at the bottom shows the parameters used for imaging.

---

## The last bottleneck

Since the speed of cryoEM imaging is no longer the bottleneck, cryo-grid preparation became the last remaining issue. For efficient cryoEM imaging, it is necessary to prepare good cryo-grids with high reproducibility with sample molecules embedded within thin ice film of several 10 nm thick with their good dispersion within the holes of carbon films [53]. Recently, various quick-freezing devices have been developed [54-57], and efforts have been made to create high-quality cryo-grids with minimal sample denaturation [54-60]. Proteins in thin films of aqueous solutions tend to localize to the air-water interface and easily denature before quick-freezing, and their orientation distribution also tends to be biased. These are the two major factors that make high-resolution 3D image reconstruction inefficient [61]. It therefore requires much time and effort to optimize the conditions for cryo-grid preparation [62, 63]. One solution to overcome this problem is to use thin support films such as graphene to adsorb sample molecules on the grid surface [64-67]. The surface adsorption of sample molecules onto the support film avoids the contact of molecules with the air-water interface, suppressing their denaturation and possibly improving the orientation bias. Graphene itself is not a good support due to its hydrophobic nature, but it can be made hydrophilic by glow discharge or chemical modification [68]. Graphene oxide obtained by treating graphite can also be used as a hydrophilic support film and is readily available at low cost, but its small flaky nature (less than 10  $\mu\text{m}$ ) makes it somewhat difficult to create grids with uniform surface coverage [69,70]. Attempts have also been made to use large graphene sheets synthesized by chemical vapor deposition (CVD) on metal substrates followed by additional surface functionalization [65, 66].

We have developed an epoxidized graphene grid (EG-grid) that effectively adsorbs protein particles on the graphene surface by applying a unique oxidation reaction using photoactivated  $\text{ClO}_2^*$  and further chemical modification with epichlorohydrin [51]. We tested the EG-grid on the cryoEM structural analyses of a number of samples, including GroEL, glyceraldehyde 3-phosphate dehydrogenase (GAPDH),  $\beta$ -galactosidase, apoferritin, and SARS-CoV-2 spike protein complexed with a VHH nanobody. For every sample, the cryo-grid showed high particle density and small orientation bias, and one or two grid preparation was sufficient for successful structural analysis. The GroEL structure was solved at 1.99  $\text{\AA}$  resolution from only about 500 images, and the GAPDH structure reached 2.16  $\text{\AA}$  resolution from only about 250 images. For the SARS-CoV-2 spike protein nanobody complex, a low concentration sample solution of 0.1 mg/ml was sufficient to collect a good dataset, and the 3.03  $\text{\AA}$  resolution density map obtained from approximately 4,200 images clearly visualized the epitope on the spike protein recognized by the nanobody of high virus-neutralizing activity. The development of a mass production process of the CVD graphene grid for EG-grid preparation is under way to make it available for cryoEM users worldwide so that cryo-grid preparation will become a routine. The EG-grid will be a powerful tool to further accelerate cryoEM structural analysis.

---

## Conclusion

The number of X-ray crystal structures deposited annually to the Protein Data Bank has remained constant at around 10,000 per year, while the annual deposition number of cryoEM structures has been growing exponentially with an annual

increase of about 1.7-fold over the past five years and reached 2,952 in 2021. Even by simple extrapolation, the number of cryoEM structures will reach 14,500 by 2024, three years from now, surpassing the number of X-ray structures. But it would be much sooner for cryoEM to become the major technique for macromolecular structural analysis considering the recent dramatic improvement in the data collection throughput as well as the steady increment in the computational speed by the development of computer hardware and image analysis software. The number of macromolecular complex structures with molecular mass greater than 500 kDa already surpassed that of X-ray structures several years ago, and the number of membrane protein structures was twice that of X-ray already in 2020.

Since all the functions and mechanisms that support biological activities of living organisms are determined by dynamic networks of interacting biomacromolecules, it is essential to elucidate the structures of biomolecular complexes going through repeated association and dissociation in atomic detail. The recent advances in cryoEM have revealed numerous complex structures and their intermolecular interactions that could not be analyzed by other techniques due to technical limitations such as difficulty in crystallization or too large size of the complexes. It is expected that cryoEM will rapidly accelerate the development of a wide range of research fields including life sciences, medical sciences, and drug discovery. CryoEM is still a technology under development. It is no exaggeration to say that the promotion of further technological development in cryoEM to maximize its power by drawing out hidden potentials is one of the most important tasks for the future of human society.

---

## Acknowledgments

We express our deepest appreciation and respect to Yoshinori Fujiyoshi, Takayuki Kato, Tomoko Miyata, and Junso Fujita, as well as many engineers and staff members of JEOL Ltd. for their great cooperation and contributions to the technical development and application of cryoEM technologies. Please note that this article is a compact and compressed version of our review article published in the 70th anniversary issue of *Microscopy* [72].

## References

- [ 1 ] Fujiyoshi Y, Uyeda N, Morikawa K, and Yamagishi H (1984) Electron microscopy of tRNA crystals II. 4  $\text{\AA}$  resolution diffraction pattern and substantial stability to radiation damage. *J. Mol. Biol.* **172**, 347-354.
- [ 2 ] Namba K and Kato T (2018) Technical development of electron cryomicroscopy and contributions to life sciences. *JEOL News* **53**, 18-24.
- [ 3 ] Fujiyoshi Y, Mizusaki T, Morikawa K, Yamagishi H, Aoki Y, Kihara H, and Harada Y (1991) Development of a superfluid helium stage for high-resolution electron microscopy. *Ultramicrosc.* **38**, 241-251.
- [ 4 ] Fujiyoshi Y (2009) Observation of membrane proteins through an electron beam. *JEOL News* **44**, 23-31.
- [ 5 ] Mimori Y, Yamashita I, Murata K, Fujiyoshi Y, Yonekura K, Toyoshima C, and Namba K (1995) The structure of the R-type straight flagellar filament of *Salmonella* at 9  $\text{\AA}$  resolution by electron cryomicroscopy. *J. Mol. Biol.* **249**, 69-87.



- [ 6 ] Yonekura K, Maki-Yonekura S, and Namba K (2003) Complete atomic model of the bacterial flagellar filament by electron cryomicroscopy. *Nature* **424**, 643-650.
- [ 7 ] Miyazawa A, Fujiyoshi Y, and Unwin N (2003) Structure and gating mechanism of the acetylcholine receptor pore. *Nature* **423**, 949-955.
- [ 8 ] Kimura Y, Vassilyev DG, Miyazawa A, Kidera A, Matsushima M, Mitsuoka K, Murata K, Hirai T, Fujiyoshi Y (1997) Surface of bacteriorhodopsin revealed by high-resolution electron crystallography. *Nature* **389**, 206-211.
- [ 9 ] Murata K, Mitsuoka K, Hirai T, Walz T, Agre P, Heymann JB, Engel A, Fujiyoshi Y (2000) Structural determinants of water permeation through aquaporin-1. *Nature* **407**, 599-605.
- [10] Gonen T, Cheng Y, Sliz P, Hiroaki Y, Fujiyoshi Y, Harrison SC, and Walz T (2005) Lipid-protein interactions in double-layered two-dimensional AQP0 crystals. *Nature* **438**, 633-638.
- [11] Carragher B, Kisseberth N, Kriegman D, Milligan R A, Potter C S, Pulokas J, and Reilein A (2000) Leginon: An automated system for acquisition of images from citreous ice specimens. *J. Struct. Biol.* **132**, 33-45.
- [12] Suloway C, Pulokas J, Fellmann D, Cheng A, Guerra F, Quispe J, Stagg S, Potter C S, and Carragher B (2005) Automated molecular microscopy: The new Leginon system. *J. Struct. Biol.* **151**, 41-60.
- [13] Mastronarde D N (2005) Automated electron microscope tomography using robust prediction of specimen movements. *J. Struct. Biol.* **152**, 36-51.
- [14] Zhang J, Nakamura N, Shimizu Y, Liang N, Liu X, Jakana J, Marsh M P, Booth C R, Shinkawa T, Nakata M, and Chiu W (2009) JADAS: A customizable automated data acquisition system and its application to ice-embedded single particles. *J. Struct. Biol.* **165**, 1-9.
- [15] Fujii T, Kato T, and Namba K (2009) Specific arrangement of  $\alpha$ -helical coiled coils in the core domain of the bacterial flagellar hook for the universal joint function. *Struct.* **17**, 1485-1493.
- [16] Fujii T, Iwane AH, Yanagida T, and Namba K (2010) Direct visualization of secondary structures of F-actin by electron cryomicroscopy. *Nature* **467**, 724-728.
- [17] Gayathri P, Fujii T, Møller-Jensen J, van den Ent F, Namba K, and Löwe J (2012) A bipolar spindle of antiparallel ParM filaments drives bacterial plasmid segregation. *Science* **338**, 1334-1337.
- [18] Fujii T, Cheung M, Blanco A, Kato T, Blocker A J, Namba K (2012) Structure of a type III secretion needle at 7-Å resolution provides insights into its assembly and signaling mechanisms. *Proc. Natl. Acad. Sci. USA* **109**, 4461-4466.
- [19] Fujii T and Namba K (2017) Structure of actomyosin rigour complex at 5.2 Å resolution and insights into the ATP cycle mechanism. *Nature Commun.* **8**, 13969.
- [20] Fujii T, Kato T, Hiraoka K D, Miyata T, Minamino T, Chevance F F V, Hughes K T, and Namba K (2017) Identical folds used for distinct mechanical functions of the bacterial flagellar rod and hook. *Nature Commun.* **8**, 14276.
- [21] Li X, Mooney P, Zheng S, Booth C R, Braunfeld M B, Gubbens S, Agard D A, and Cheng Y (2013) Electron counting and beam-induced motion correction enable near-atomic-resolution single-particle cryo-EM. *Nat. Methods* **10**, 584-590.
- [22] Liao M, Cao E, Julius D, and Cheng Y (2013) Structure of the TRPV1 ion channel determined by electron cryo-microscopy. *Nature* **504**, 107-112.
- [23] Cao E, Liao M, Cheng Y, and Julius D (2013) TRPV1 structures in distinct conformations reveal activation mechanisms. *Nature* **504**, 113-118.
- [24] Zheng S Q, Palovcak E, Armache J-P, Verba K A, Cheng Y, and Agard D (2017) MotionCor2: anisotropic correction of beam-induced motion for improved cryo-electron microscopy. *Nat. Methods* **14**, 331-332.
- [25] Rohou A and Grigorieff N (2016) CTFFIND4: Fast and accurate defocus estimation from electron micrographs. *J. Struct. Biol.* **193**, 1-12.
- [26] Zhang K (2016) Gctf: Real-time CTF determination and correction. *J. Struct. Biol.* **193**, 1-12.
- [27] Kimanius D, Forsberg B O, Scheres S H W, Lindahl E (2016) Accelerated cryo-EM structure determination with parallelization using GPUs in RELION-2. *eLife* **5**, e18722.
- [28] Zivanov J, Nakane T, Forsberg B O, Kimanius D, Hagen W J H, Lindahl E, Scheres S H W (2018) New tools for automated high-resolution cryo-EM structure determination in RELION-3. *eLife* **7**, e42166.
- [29] Punjani A, Rubinstein J L, Fleet D J, Brubaker M A (2017) cryoSPARC: algorithms for rapid unsupervised cryo-EM structure determination. *Nat. Methods* **14**, 290-296.
- [30] Bartesaghi A, Matthies D, Banerjee S, Merk A, and Subramaniam S (2014) Structure of  $\beta$ -galactosidase at 3.2-Å resolution obtained by cryo-electron microscopy. *Proc. Natl. Acad. Sci. USA* **111**, 11709-11714.
- [31] Grant T and Grigorieff N (2015) Measuring the optimal exposure for single particle cryo-EM using a 2.6 Å reconstruction of rotavirus VP6. *eLife* **4**, e06980.
- [32] Bartesaghi A, Merk A, Banerjee S, Matthies D, Wu X, Milne J L S, and Subramaniam S (2015) 2.2 Å resolution cryo-EM structure of  $\beta$ -galactosidase in complex with a cell-permeant inhibitor. *Science* **348**, 1147-1151.
- [33] Merk A, Bartesaghi A, Banerjee S, Falconieri V, Rao P, Davis M I, Pragani R, Boxer M B, Earl L A, Milne J L S, and Subramaniam S (2016) Breaking cryo-EM resolution barriers to facilitate drug discovery. *Cell* **165**, 1-10.
- [34] Danev R, Yanagisawa H, Kikkawa M (2018) Cryo-electron microscopy methodology: current aspects and future directions. *Trends Biochem. Sci.* **44**, 837-848.
- [35] Kato T, Makino F, Nakane T, Terahara N, Kaneko T, Shimizu Y, Motoki S, Ishikawa I, Yonekura K, and Namba K (2019) CryoTEM with a cold field emission gun that moves structural biology into a new stage. *Microsc. Microanal.* **25**, 998-999.
- [36] Yip K M, Fischer N, Paknia E, Chari A, and Stark H (2020) Atomic-resolution protein structure determination by cryo-EM. *Nature* **587**, 157-161.
- [37] Nakane T, Kotecha A, Sente A, McMullan G, Masiulis S, Brown P M G E, Grigoras I T, Malinauskaitė L, Malinauskas T, Miehl J, Uchanske T, Yu L, Karia D, Pechnokova E V, de Jong E, Keizer J, Bischoff M, McCormack J, Tiemeijer P, Hardwick S W, Chirgadze, D Y, Murshudov G, Aricescu A R, and Scheres S H W (2020) Single-particle cryo-EM at atomic resolution. *Nature* **587**, 152-156.
- [38] Baldwin P R, Tan Y Z, Eng E T, Rice W J, Noble A J, Negro C J, Cianfrocco M A, Potter C S, and Carragher B (2018) Big data in cryoEM: Automated collection, processing and accessibility of EM data. *Curr. Opin. Microbiol.* **43**, 1-8.
- [39] Weis F and Hagen W J H (2020) Combining high throughput and high quality for cryo-electron microscopy

- data collection. *Acta Cryst. D* **76**, 724–728.
- [40] Cheng A, Eng E T, Alink L, Rice W J, Jordan K D, Kim L Y, Potter C S, and Carragher B (2018) High resolution single particle cryo-electron microscopy using beam-image shift. *J. Struct. Biol.* **204**, 270–275.
- [41] Wu C, Huang X, Cheng J, Zhu D, and Zhang X (2019) High-quality, high-throughput cryo-electron microscopy data collection via beam tilt and astigmatism-free beam-image shift. *J. Struct. Biol.* **208**, 107396.
- [42] Li Y, Cash J N, Tesmer J J G, and Cianfrocco M A (2020) High-throughput cryo-EM enabled by user-free preprocessing routines. *Struct.* **28**, 858–869.
- [43] Zhang K, Pintilie G D, Li S, Schmid M F, and Chiu W (2020) Resolving individual atoms of protein complex by cryo-electron microscopy. *Cell Res.* **30**, 1136–1139.
- [44] Danev R, Yanagisawa H, and Kikkawa M (2021) Cryo-EM performance testing of hardware and data acquisition strategies. *Microsc.* **2021**, 1–11.
- [45] Oosaki A, Hosogi N, Makino F, Motoki S, Ishikawa I, Ookura Y, and Kobayashi K (2021) Development of high throughput cryo electron microscope with cold field emission gun (CRYO ARM™ 300 II). *Microsc. Microanal.* **30**, 1634–1636.
- [46] Kato T, Makino F, Miyata T, Horváth P, and Namba K (2019) Structure of the native supercoiled flagellar hook as a universal joint. *Nat. Commun.* **10**, 5295.
- [47] Yamada Y, Namba K, and Fujii T (2020) Cardiac muscle thin filament structures reveal calcium regulatory mechanism. *Nat. Commun.* **11**, 153.
- [48] Yamaguchi T, Makino F, Miyata T, Minamino T, Kato T, and Namba K (2021) Structure of the molecular bushing of the bacterial flagellar motor. *Nat. Commun.* **12**, 4469.
- [49] Schob M, Haberbosch I, Hagen W J H, Schwab Y, and Mastronarde D N (2019) Software tools for automated transmission electron microscopy. *Nat. Methods* **16**, 471–477.
- [50] Kawamoto A, Miyata T, Makino F, Kinoshita M, Minamino T, Imada K, Kato T, and Namba K (2021) Native flagellar MS ring is formed by 34 subunits with 23-fold and 11-fold subsymmetries. *Nat. Commun.* **12**, 4223.
- [51] Fujita J, Makino F, Asahara H, Moriguchi M, Kumano S, Anzai I, Kishikawa J, Matsuura Y, Kato T, Namba K, Inoue T. (2021) Epoxidized graphene grid for high-throughput high-resolution cryoEM structural analysis. *bioRxiv* <https://doi.org/10.1101/2021.11.17.468963v1>.
- [52] Hamaguchi T, Maki-Yonekura S, Naitow H, Matsuura Y, Ishikawa T, and Yonekura K (2019) A new cryo-EM system for single particle analysis. *J. Struct. Biol.* **207**, 40–48.
- [53] Dubochet J, Adrian M, Chang J O J, Homo J-C, Lepault J, McDowell A W, and Schultz P (1988) Cryo-electron microscopy of vitrified specimens. *Q. Rev. Biophys.* **21**, 129–228.
- [54] Jain T, Sheehan P, Crum J, Carragher B, and Potter C S (2012) Spotiton: A prototype for an integrated inkjet dispense and vitrification system for cryo-TEM. *J. Struct. Biol.* **179**, 68–75.
- [55] Razinkov I, Dandey V P, Wei H, Zhang Z, Melnekoff D, Rice W J, Wigge C, Potter C S, and Carragher B (2016) A new method for vitrifying samples for cryoEM. *J. Struct. Biol.* **195**, 190–198.
- [56] Dandey V P, Wei H, Zhang Z, Tan Y Z, Acharya P, Eng E T, Rice W J, Kahn P A, Potter C S, and Carragher B (2018) Spotiton: New features and applications. *J. Struct. Biol.* **202**, 161–169.
- [57] Ravelli R B G, Nijpels F J T, Henderikx R J M, Weissenberger G, Thewissen S, Gijbbers A, Beulen B W A M M, López-Iglesias C, and Peters P J (2020) Cryo-EM structures from sub-nl volumes using pin-printing and jet vitrification. *Nat. Commun.* **11**, 2563.
- [58] Lee J, Saha A, Pancera S M, Kempster A, Rieger J, Bose A, and Tripathi A (2012) Shear free and blotless cryo-TEM imaging: a new method for probing early evolution of nanostructures. *Langmuir* **28**, 4043–4046.
- [59] Arnold S A, Albiez S, Bieri A, Syntychaki A, Adaixo R, McLeod R A, Gokdie K N, Stahlberg H, and Braun T (2017) Blotting-free and lossless cryo-electron microscopy grid preparation from nanoliter-sized protein samples and single-cell extracts. *J. Struct. Biol.* **197**, 220–226.
- [60] Feng X, Fu Z, Kaledhonkar S, Jia Y, Shar B, Jin A, Liu Z, Sun M, Chen B, Grassucci R A, Ren Y, Jiang H, Frank J, Lin Q (2017) A fast and effective microfluidic spraying-plunging method for high-resolution single-particle cryo-EM. *Struct.* **25**, 663–670.
- [61] D'Imprima E, Floris D, Jope M, Sánchez R, Grininger M, and Kühlbrandt W (2019) Protein denaturation at the air-water interface and how to prevent it. *eLife* **8**, e42747.
- [62] Drulyte I, Johnson R M, Hesketh E L, Hurdiss D L, Scarff C A, Porav S A, Ranson N A, Muench S P, and Thompson R F (2018) Approaches to altering particle distributions in cryo-electron microscopy sample preparation. *Acta Cryst. D* **74**, 560–571.
- [63] Glaeser R M (2016) How good can cryo-EM become? *Nat. Methods* **13**, 28–32.
- [64] Grassucci R A, Taylor D J, and Frank J (2007) Preparation of macromolecular complexes for cryo-electron microscopy. *Nat. Protoc.* **2**, 3239–3246.
- [65] Han Y, Fan X, Sang H, Zhao F, Tully C G, Kong J, Yao N, and Yan N (2020) High-yield monolayer graphene grids for near-atomic resolution cryoelectron microscopy. *Proc. Natl. Acad. Sci. USA* **117**, 1009–1014.
- [66] Naydenova K, Peet M J, and Russo C J (2019) Multifunctional graphene supports for electron cryomicroscopy. *Proc. Natl. Acad. Sci. USA* **116**, 11718–11724.
- [67] Pantelic R S, Suk J W, Magnuson C W, Meyer J C, Wachsmuth P, Kaiser U, Ruoff R S, and Stahlberg H (2011) Graphene: Substrate preparation and introduction. *J. Struct. Biol.* **174**, 234–238.
- [68] Russo C J & Passmore L A (2014) Controlling protein adsorption on graphene for cryo-EM using low-energy hydrogen plasmas. *Nat. Methods* **11**, 649–652.
- [69] Santamaría-Juárez G, Gómez-Barojas E, Quiroga-González E, Sánchez-Mora E, Quintana-Ruiz M, and Santamaría-Juárez J D (2019) Safer modified Hummers' method for the synthesis of graphene oxide with high quality and high yield. *Mater. Res. Express* **6**, 125631.
- [70] Hummers W S and Offeman R E (1958) Preparation of Graphitic Oxide. *J. Am. Chem. Soc.* **80**, 1339–1339.
- [71] Maeda R, Fujita J, Konishi Y, Kazuma Y, Yamazaki H, Anzai I, Yamaguchi K, Kasai K, Nagata K, Yamaoka Y, Miyakawa K, Ryo A, Shirakawa K, Makino F, Matsuura Y, Inoue T, Imura A, Namba K, and Takaori-Kondo A (2021) Nanobodies recognizing conserved hidden clefts of all SARS-CoV-2 spike variants. *bioRxiv* <https://doi.org/10.1101/2021.10.25.465714>.
- [72] Namba K & Makino F (2022) Recent progress and future perspective of electron cryomicroscopy for structural life sciences. *Microscopy* in press.

# Chemical-State Analysis of Li Compounds and Nitrogen-Getter Material for Liquid Li by Soft X-ray Emission Spectroscopy

Keisuke Mukai<sup>1,2</sup>, Ryo Omura<sup>1</sup>, Juro Yagi<sup>1</sup>, Ryuta Kasada<sup>3</sup>

<sup>1</sup>Institute of Advanced Energy, Kyoto University, <sup>2</sup>Kyoto Fusion Engineering Ltd. <sup>3</sup>Institute for Material Research, Tohoku University

Lithium metal and oxides are key compounds for Li air battery and nuclear fusion. Constructing two dimensional mappings is a useful approach to understand chemical behavior and degradation mechanism of such materials at the micro-scale. Herein, we employ the soft X-ray emission spectrometer (SXES) to analyze characteristic X-ray emission spectra from the Li metal/oxides and nitrogen-getter material immersed in liquid Li metal. The high energy resolutions allowed us to measure N-K $\alpha$  and Ti-L $\ell$  emissions, separately. By comparing with the first-principle calculated density of states, the elemental and chemical state mappings in the degraded materials were successfully constructed.

## Introduction

As light elements have attractive nuclear properties, low Z (Z: atomic number) materials are utilized as key components in nuclear fission and fusion. Such materials are used in an extreme condition, such as high temperature, chemically corrosive environments, and intense neutron flux. Thus, it is of particular importance to understand those chemical behaviors and clarify degradation mechanisms, experimentally. We here employ a soft X-ray emission spectrometer (SXES) attached to an electron probe micro-analyzer (EPMA), which covers a low energy range (50–210 eV) with ultra-high energy resolutions as good as 0.2 eV [1,2]. In our previous studies, we report chemical state analysis of the low Z compounds utilized in the nuclear sector, including Li–Pb eutectic alloy, Be intermetallics, and B<sub>4</sub>C [3–6]. Herein, we introduce our recent studies: (i) electron structure analysis and chemical state mapping for Li metal and oxides [7], (ii) SXES peak analysis for clarifying N distribution within Fe–Ti alloy getter immersed in liquid Li metal [8].

## SXES analysis on Li metal and oxides

### Motivation

Li metal and oxides can serve as a tritium breeding material in nuclear fusion reactors, which converts kinetic energy of neutrons into heat and simultaneously produces fuel tritium by nuclear transmutation [9]. Additionally, Li–O<sub>2</sub> air battery has attracted significant attentions as alternative means of electrochemical storage where a Li metal anode is oxidized

and releases Li<sup>+</sup> to form discharge products of Li<sub>2</sub>O<sub>2</sub> at the cathode [9,10]. Generally, Li metal and oxides are chemically reactive in ambient atmosphere to form impurity phases and corrosion products that can degrade performance and raise safety concerns. Chemical phase analysis of Li-containing products can help our understandings of chemical reactions and degradations in such systems. Herein, the SXES developed by JEOL was employed to assess electronic states in Li, Li<sub>2</sub>O<sub>2</sub>, and Li<sub>2</sub>O for the chemical-state analysis. The SXES spectra are directly compared with the partial density of states (PDOS) of Li using density functional theory (DFT) calculations. Due to large errors in band calculations in oxides by DFT, not only a conventional functional based on the generalized gradient approximation (GGA) but also a hybrid functional were used in this study.

### Methods

Commercially available Li metal rod, Li<sub>2</sub>O, and Li<sub>2</sub>O<sub>2</sub> powders were procured and stored in a glove box filled with Ar gas. The powder samples were analyzed by a JXA-8500F field emission electron probe micro-analyzer (FE-EPMA) by JEOL equipped with SXES (SS-94000SXES by JEOL). The grating JS50XL was used for the analysis [1]. The measurement time and the acceleration voltages of the electron beam were 60 s and 2.0 kV, respectively. DFT calculations were performed using the Perdew–Burke–Ernzerhof (PBE) functional and hybrid HSE06 functional implemented in the Vienna ab initio simulation package (VASP) [10–14]. The electron configurations 1s<sup>2</sup>2s<sup>1</sup>, 2s<sup>2</sup>2p<sup>4</sup> were used for the Li and O atoms, respectively. For a direct comparison between SXES



spectrum and occupied states by PDOS, the energy of PDOS was referenced to the Li 1s band centroid,  $E_{Li-1s}$ .  $E_{Li-1s}$  was calculated as follows;

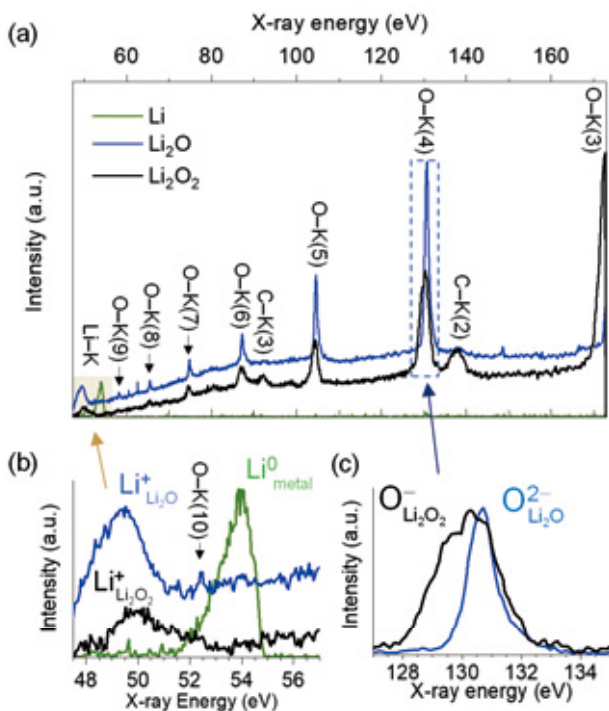
$$E_{Li-1s} = \frac{\int_{-\infty}^{E_{max}} E g_{Li-1s}(E) dE}{\int_{-\infty}^{E_{max}} g_{Li-1s}(E) dE}$$

where  $g_{Li-1s}(E)$  and  $E_{max}$  are the density of states of Li 1s orbitals at  $E$  and maximum energy of the Li 1s orbitals, respectively.

## Results and Discussion

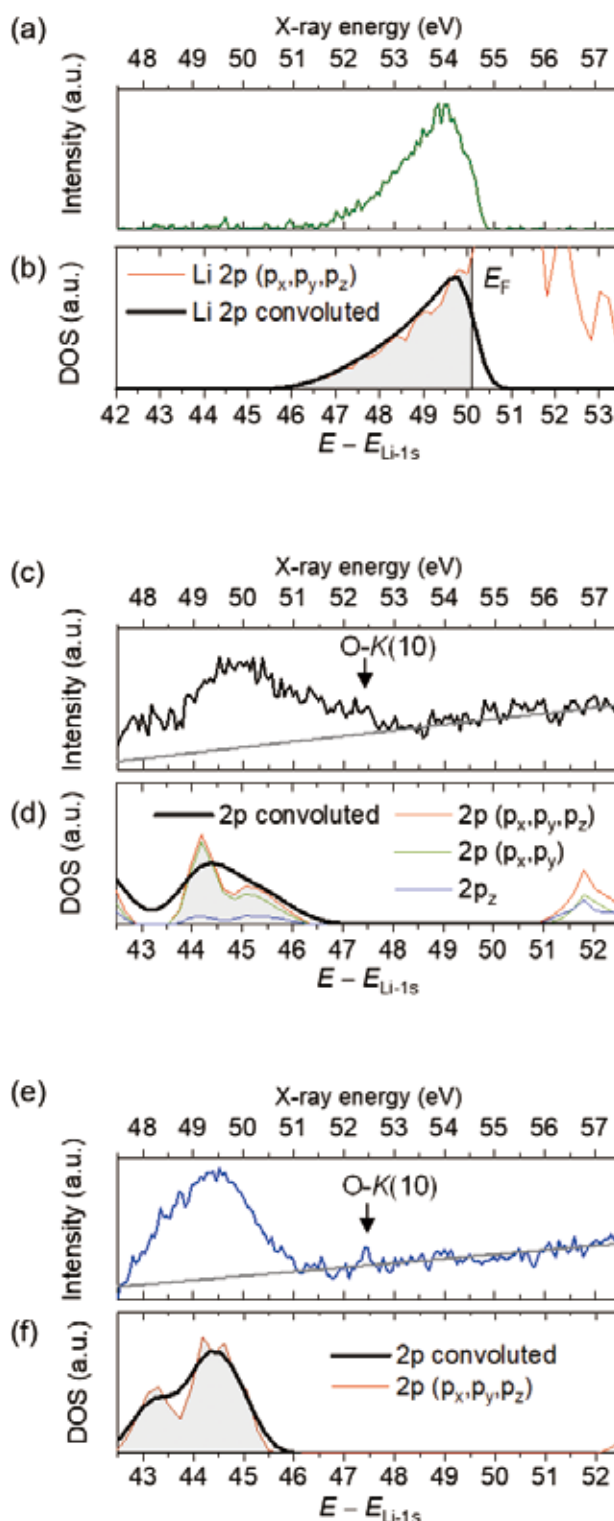
X-ray powder diffraction (XRD) was carried out using Co-K $\alpha$ , which indicated the formation of LiOH impurity phase in both of the Li<sub>2</sub>O<sub>2</sub> and Li<sub>2</sub>O samples. Multi-phase Rietveld refinements using the XRD data was carried out, which quantified ~6.3 and ~11.7 w.t.% of LiOH (space group: P4/nmm) in the Li<sub>2</sub>O<sub>2</sub> and Li<sub>2</sub>O samples respectively. **Figure 1** shows the SXES spectra of the Li metal, Li<sub>2</sub>O<sub>2</sub>, and Li<sub>2</sub>O samples. In the obtained spectra,  $n^{\text{th}}$  order peaks of Li-K $\alpha$  ( $n = 1$ ) and O-K $\alpha$  ( $n = 3-10$ ) were observed. Peaks of C-K $\alpha$  ( $n = 2$  and 3) were also observed. Taking the XRD results into account, the C peak could derive not from Li<sub>2</sub>CO<sub>3</sub> formation but from a carbon conduction tape. The Li-K spectrum of Li metal showed an asymmetric Doniach-Šunjić line shape in the range of 52–54.5 eV (Fig. 1b). The Li-K peak intensities for Li<sub>2</sub>O<sub>2</sub> and Li<sub>2</sub>O were significantly lower than that of Li. Ionization to Li<sup>+</sup> (oxidation) causes numerous Li valence electrons to be lost, and results in

**Fig. 1**



SXES spectra from the Li metal, Li<sub>2</sub>O<sub>2</sub>, and Li<sub>2</sub>O samples in the energy ranges of 47.5–173 eV (a), 47.5–57 eV for Li-K (b), and 127–135 eV for O-K(4) (c), in which number in bracket denotes the X-ray diffraction order.

**Fig. 2**



The Li-K spectra for Li (a), Li<sub>2</sub>O<sub>2</sub>(c), and Li<sub>2</sub>O (e) using the SXES compared to the convoluted DOSs of occupied Li 2p states in Li metal (b), Li<sub>2</sub>O<sub>2</sub>(d), and Li<sub>2</sub>O (f) using hybrid Heyd-Scuseria-Ernzerhof (HSE) functionals. Gray solid lines in panel (c) and (e) denotes linear background. Calculated energy is referenced to Li 1s centroid ( $E_{Li-1s}$ ) where Li 2p occupied states below the Fermi energy are colored by gray.



poor signal to noise (S/N) ratios.

In **Fig. 2**, the SXES Li–K spectra are directly compared with the DOS of Li using the HSE functional. The energy was referenced to  $E_{\text{Li-1s}}$ . The calculated Li  $2p$  occupied states were convoluted with Gaussian functions with full width at half-maxima (FWHM) of 0.6 eV (Li and  $\text{Li}_2\text{O}$ ) and 0.9 eV ( $\text{Li}_2\text{O}_2$ ) because of the difference in the calculated  $1s$  band width. The shapes of Li–K spectra agreed well with the convoluted  $2p$  occupied states. The calculated energies using HSE were underestimated as large as 4.0 eV for Li metal and 5.3 eV for the oxides. A comparison between the experimental spectra and DOS using PBE supports that the obtained spectral shapes describe Li valence electronic states, while the energetic underestimations were even larger with PBE.

The Li–K spectrum for  $\text{Li}_2\text{O}_2$  mainly derived from antibonding  $\pi_g^*$  orbitals appeared at 49–52 eV, while the peak of bonding orbitals ( $\sigma_g$  and  $\pi_u$ ) were below the SXES low-energy limit. The contributions of both bonding and antibonding orbitals were seen in the broad peak of O–K(4) for  $\text{Li}_2\text{O}_2$  in **Fig. 1c**. The O–K(4) FWHM of the  $\text{Li}_2\text{O}_2$  sample was 2.26 times wider than that from the  $\text{Li}_2\text{O}$  sample, which was consistent with the valence band width ratio of 2.12 calculated using HSE. The wide valence band was attributed to the anisotropic  $2p$  states in  $\text{Li}_2\text{O}_2$ . Although the unidentified O–K peak in  $\text{Li}_2\text{O}$  was observed at 528.9 eV in the previous SXES results [15], no peak was found at the corresponding position of 132.2 eV for O–K(4) in the  $\text{Li}_2\text{O}$  spectrum in the present work.

The chemical state and element mappings on a Li metal sample that has been naturally oxidized in air with a partial metallic surface are shown in **Fig. 3**. The SXES spectra were collected at  $40 \times 32$  measuring points (1280 points), with an acquisition time of 30 s per pixel (pixel size:  $1 \mu\text{m} \times 1 \mu\text{m}$ ).

From the naturally oxidized Li metal sample, the Li–K spectra of  $\text{Li}_2\text{O}$  ( $E < 51$  eV) and Li ( $> 51$  eV) were observed without peak overlap. No  $\text{Li}_2\text{O}_2$  peak was found from the collected data, as predicted by the MALT thermodynamic database. **Figure 3** visualizes element and chemical state mappings in the naturally oxidized Li metal sample. The energy ranges for Li metal ( $\text{Li}^0$ ) and  $\text{Li}_2\text{O}$  ( $\text{Li}^+$ ) were set as 51.0–55.0 eV and 47.5–51.0 eV as shown in **Fig. 3d**. Chemical state mappings (**Fig. 3a,b**) visualize Li metal/oxide phase distribution on the sample; the metallic Li phase was distributed on the right side of the observed area, while the  $\text{Li}_2\text{O}$  phase lies on the left. Together with O element mapping (**Fig. 3c**), it is possible to distinguish the  $\text{Li}_2\text{O}$  phase from other oxide phases with lacking Li. Nevertheless, the visualization of oxide phases struggled with weak Li–K emissions from the oxide samples. For an identification whether  $\text{Li}_2\text{O}_2$  or  $\text{Li}_2\text{O}$  phase in a Li– $\text{O}_2$  battery system, it is recommended to utilize O–K emissions rather than weak Li–K. A chemical state mapping of  $\text{Li}_2\text{O}_2$  may be accomplished by integrating signals of the bonding orbitals appeared in the range of 128–130 eV for O–K(4) (**Fig. 2c**).

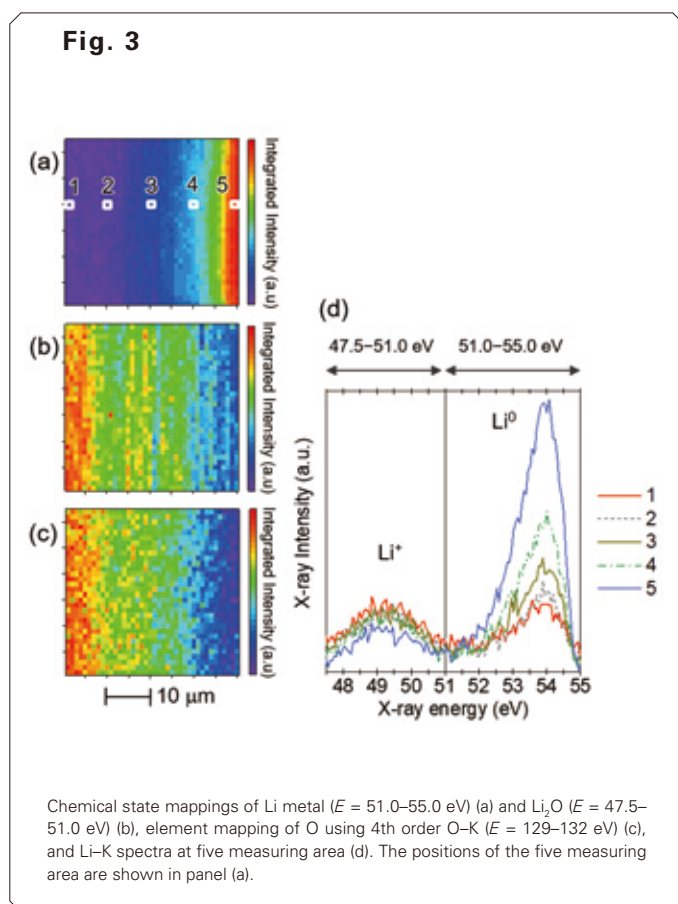
## Analysis on Fe–Ti alloy immersed in liquid Li metal

### Motivation

Liquid Li metal is a target material of an accelerator-based neutron source using d–Li stripping reaction [16]. N impurity is easily contained by liquid Li metal, which should be removed because it enhances corrosion of stainless tube [17]. As a trap material for removing N from liquid lithium metal, the use of Fe–Ti alloys has been proposed in order to overcome a low absorption rate of N by pure Ti [18]. However, distribution of trapped N within the Fe–Ti alloy have not been understood because characteristic X-ray emissions of N– $K\alpha$  (392 eV) and Ti– $L\ell$  (395 eV) are close and thus highly overlapped with conventional devices such as EDX (energy dispersive X-ray spectrometer). Thus, by separating these peaks using the SXES with an ultra-high energy resolution, we investigated Ti and N distribution within the Fe–Ti alloy samples after immersing in liquid Li metal.

### Experimental

Fe–Ti alloy spherical samples (diameter: 100–125  $\mu\text{m}$ ) containing 5 at.% of Ti were prepared by gas atomize method. 5.0 g of lithium (99.9% purity),  $\text{Li}_3\text{N}$  (99% purity) and 1.0 g of the alloys were enclosed in a SUS316L capsule in a glove box filled with Ar gas. Here, the amount of  $\text{Li}_3\text{N}$  was equal to 1000 wt.ppm of nitrogen concentration in liquid Li. The capsules were heated in an electric furnace for 9, 36, 81, and 256 h at 823 K. The SXES analysis was performed with the JS200N grating. The SXES spectra were collected by scanning the sample stage linearly in step of 1.0  $\mu\text{m}$  from the surface toward the central part of the alloys. SXES analyses were performed with acceleration voltage of 15 kV, beam current of 120 nA, and exposure time of 1000 s. In order to separate second order peaks of N– $K\alpha$  (392 eV) and Ti– $L\ell$ , reference energy spectra of nitrogen and titanium,  $f_{\text{N}}$  and  $f_{\text{Ti}}$ , were collected with ZrN powder (99% purity) and as-received Fe–Ti sample, respectively. The synthesized energy spectra  $f$  were obtained by fitting to the experimental spectra by the equation  $f = k_{\text{N}}f_{\text{N}} + k_{\text{Ti}}f_{\text{Ti}}$  where  $k_{\text{N}}$ ,  $k_{\text{Ti}}$ ,  $f_{\text{N}}$ , and  $f_{\text{Ti}}$  are weighting coefficients of N and Ti, and reference spectra for N and Ti taken from ZrN and as-received Fe–Ti sample, respectively. In **Fig. 4**, as an example, the SXES spectrum from the Fe–Ti sample



immersed for 256 h and the synthesized spectrum are shown. Concentration of X (X = N, Ti, and Fe),  $C_X$ , was calculated as follows:

$$C_X = \int_{192}^{200} k_X f_X dE$$

where  $E$  is X-ray energy (eV).

## Results and Discussion

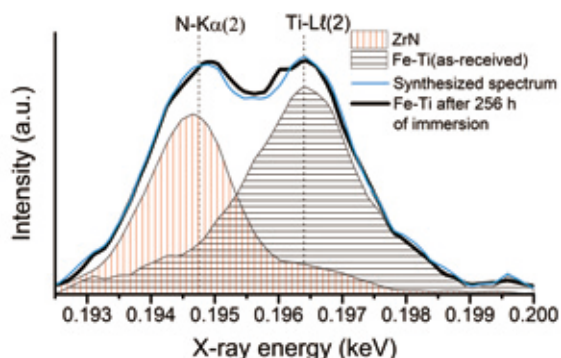
**Figure 5** shows the element mapping of Ti using Ti-K $\alpha$  and the grain boundary distribution obtained from the cross section of the Fe-Ti sample immersed for 256 h in the liquid Li metal. From the overlaid image of EDX and electron backscattered diffraction (EBSD) in Fig. 5(c), high concentrations of Ti were seen in the grain boundaries. The XRD patterns from the immersed samples showed a gradual shift of diffraction peaks to higher  $2\theta$  angle as the immersion time became longer. This indicates a gradual decrease in interplanar spacing of  $\alpha$ -Fe phase due to loss of dissolved titanium. Ti can exist a solute element in  $\alpha$ -Fe phase up to the fraction of approximately 2 at.% at 823 K [19]. As the Fe-Ti sample was oversaturated

state, dissolved Ti in the crystal grain was diffused during the immersion and finally trapped by segregated Ti in the grain boundaries.

The results of SXES line analysis in the immersed samples are shown in **Fig. 6**. The scan was carried out in the direction from the surface to the center of the samples. The immersed samples for 9–256 h had high N concentrations on the surfaces. In these samples, the peaks of Ti appeared with N peaks, indicating N impurities trapped at the grain boundaries. In the sample immersed for 256 h, the N peak was observed even in the central part of the spherical sample. This indicates that N diffusion and trapping is dominant on the surfaces and in the grain boundaries of the alloy samples. The concentration ratios of N/Ti were calculated by dividing  $C_N$  by  $C_{Ti}$ . The N/Ti ratio were independent on the immersion periods, where the ratios were high from the surfaces to 5  $\mu\text{m}$  deep because of the surface trapping. It is indicated that nitrogen is trapped rapidly near the surface of alloy samples, and gradually trapped in the grain boundaries as nitrogen diffuses into the Fe-Ti alloy samples.

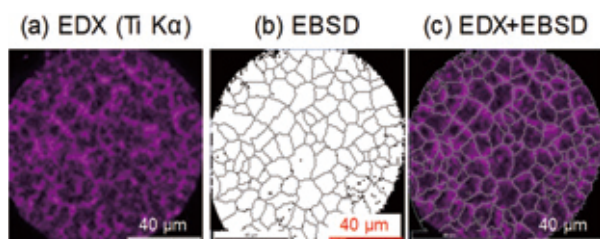
Mean N diffusivity in the Fe-Ti samples was estimated from the results of the SXES line analysis, in which the longest

**Fig. 4**



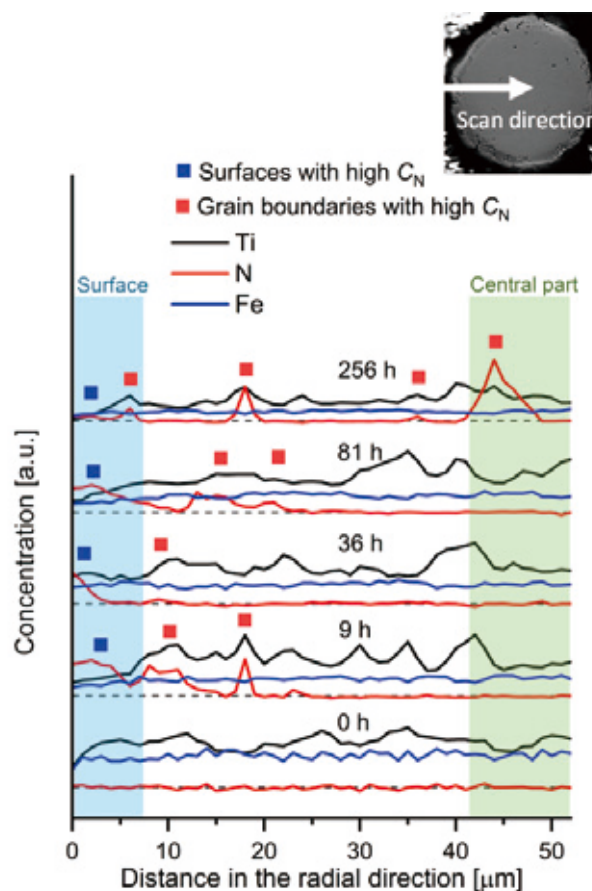
SXES spectrum from the Fe-Ti sample immersed in liquid Li metal for 256 h, synthesized spectrum, and reference spectra from ZrN and as-received Fe-Ti sample.

**Fig. 5**



(a) Ti-K energy dispersive X-rays (EDX) mapping, (b) electron backscatter diffraction (EBSD) mapping, and (c) EDX + EBSD overlaid image of the Fe-Ti sample immersed for 256 h in the liquid Li metal.

**Fig. 6**



Concentrations of N, Ti, and Fe obtained by SXES line analysis for the cross sections of the Fe-Ti samples before and after immersion in the liquid Li metal. Inset SEM image shows the cross section, measurement positions, and scan direction.

distances of N peak from the surfaces were set as the mean diffusion distances. As a result, the N diffusivity in the Fe–Ti sample was estimated to be  $5 \times 10^{-16}$  m<sup>2</sup>/s at 823 K. The obtained diffusivity was much higher than that in pure  $\alpha$ -Ti ( $1.3 \times 10^{-19}$  m<sup>2</sup>/s) at 823 K [20]. It is considered that N diffuses in the Fe–Ti alloy much faster than that  $\alpha$ -Ti because it diffuses through dominantly in  $\alpha$ -Fe phase. The high N diffusivity of Fe–Ti alloy is a promising property as a getter material immersed in liquid Li metal.

## Conclusion

In this study, electronic state analysis was carried out using the SXES for visualizing elemental and chemical state mappings. First, electronic states of Li metal and oxides were investigated and then compared with PDOS of Li using DFT calculations. Characteristic Li–K $\alpha$  emissions from Li, Li<sub>2</sub>O<sub>2</sub>, and Li<sub>2</sub>O were detected in the low energy region of 47.5–54.0 eV. By utilizing the Li 1s core-level shift in Li<sub>2</sub>O, the chemical state mappings were successfully constructed. To overcome very weak signals of Li–K from Li oxides, it is proposed to set ROI in O–K $\alpha$  emissions for visualizing Li<sub>2</sub>O<sub>2</sub> and Li<sub>2</sub>O phases separately. Second, the SXES peak analysis was carried out to separately visualize N and Ti distributions in the Fe–Ti alloy samples immersed in liquid Li metal. The results indicated that N is trapped rapidly near the surface of alloy samples, and gradually diffused along the grain boundaries. The mean diffusivity of N in the Fe–Ti samples was estimated to be  $5 \times 10^{-16}$  m<sup>2</sup>/s from the results of the SXES line analysis.

## Acknowledgments

This work is partially supported by the Joint Usage/Research Program on Zero-Emission Energy Research, Institute of Advanced Energy, Kyoto University (ZE29A-21, ZE30A-09). This work is also carried out with the support and under the auspices of the QST Collaborative Research Program. Prof. Satoshi Konishi (Kyoto University), Toshiro Sakabe (JSPS research fellowship DC2, Kyoto University), and Prof. Kazuya Sasaki (Hirotsuki University) are thanked for helpful discussions.

## References

- [ 1 ] Terauchi, M.; Takahashi, H.; Handa, N.; Murano, T.; Koike, M.; Kawachi, T.; Imazono, T.; Koeda, M.; Nagano, T.; Sasai, H.; Oue, Y. Ultrasoft-X-ray emission spectroscopy using a newly designed wavelength-dispersive spectrometer attached to a transmission electron microscope. *J. Electron Microsc.* 2012, **61**, 1–8.
- [ 2 ] Takahashi, H.; Murano, T.; Takakura, M.; Asahina, S.; Terauchi, M.; Koike, M.; Imazono, T.; Koeda, M.; Nagano, T. Development of soft X-ray emission spectrometer for EPMA/SEM and its application. *IOP Conf. Ser. Mater. Sci. Eng.* 2016, **109**, 012017.
- [ 3 ] Kasada, R.; Mukai, K.; Chemical State Analysis of Light Elements in Nuclear Fission and Fusion Reactor Materials by Soft X-ray Emission Spectroscopy in Electron Probe Microanalyzer. *JEOL News* 2020, **55**, 32–35.
- [ 4 ] Park, C.; Nozawa, T.; Kasada, R.; Tosti, S.; Konishi, S.; Tanigawa, H. The effect of wall flow velocity on compatibility of high-purity SiC materials with liquid Pb–Li alloy by rotating disc testing for 3000 h up to 900° C. *Fusion Eng. Des.* 2018, **136**, 623–627.
- [ 5 ] Mukai, K.; Kasada, R.; Yabuuchi, K.; Konishi, S.; Kim, J.H.; Nakamichi, M. Valence Electron and Chemical State Analysis of Be<sub>12</sub>M (M = Ti, V) Beryllides by Soft X-ray Emission Spectroscopy. *ACS Appl. Energy Mater.* 2019, **2**, 2889–2895.
- [ 6 ] Kasada, R.; Ha, Y.; Higuchi, T.; Sakamoto, K. Chemical State Mapping of Degraded B<sub>4</sub>C Control Rod Investigated with Soft X-ray Emission Spectrometer in Electron Probe Micro-analysis. *Sci. Rep.* 2016, **6**(1), 1–6.
- [ 7 ] Mukai, K.; Kasada, R.; Sasaki, K.; Konishi, S. Occupied Electronic States of Li in Li, Li<sub>2</sub>O<sub>2</sub>, and Li<sub>2</sub>O Analyzed by Soft X-ray Emission Spectroscopy. *J. Phys. Chem. C* 2020, **124**, 9256–9260.
- [ 8 ] Omura, R.; Yagi, J.; Mukai, K.; Oyaidzu, M.; Ochiai, K.; Kasugai, A.; Konishi, S. Analysis of nitrogen distribution in iron-titanium alloys after nitrogen trapping in liquid lithium by using soft X-ray emission spectroscopy. *Fusion Eng. Des.* 2021, **170**, 112548.
- [ 9 ] Konishi, S.; Enoda, M.; Nakamichi, M.; Hoshino, T.; Ying, A.; Sharafat, S.; Smolentsev, S. Functional materials for breeding blankets—status and developments. *Nucl. Fusion* 2017, **57**(9), 092014.
- [10] Lai, J.; Xing, Y.; Chen, N.; Li, L.; Wu, F.; Chen, R. Electrolytes for rechargeable lithium–air batteries. *Angew. Chem. Int. Ed.* 2020, **59**(8), 2974–2997.
- [11] Perdew, J.P.; Burke, K.; Ernzerhof, M. Generalized gradient approximation made simple. *Phys. Rev. Lett.* 1996, **77**, 3865–3868.
- [12] Blöchl, P. E. Projector augmented-wave method. *Phys. Rev. B* 1994, **50**, 17953–17979.
- [13] Kresse, G.; Furthmüller, J. Efficient iterative schemes for ab initio total-energy calculations using a plane-wave basis set. *Phys. Rev. B* 1996, **54**, 11169–11186.
- [14] Heyd, J.; Scuseria, G.E.; Ernzerhof, M. Hybrid functionals based on a screened Coulomb potential. *J. Chem. Phys.* 2003, **118**, 8207–8215.
- [15] Léon, A.; Fiedler, A.; Blum, M.; Benkert, A.; Meyer, F.; Yang, W.; Bär, M.; Scheiba, F.; Ehrenberg, H.; Weinhardt, L.; Heske, C. Valence Electronic Structure of Li<sub>2</sub>O<sub>2</sub>, Li<sub>2</sub>O, Li<sub>2</sub>CO<sub>3</sub>, and LiOH Probed by Soft X-ray Emission Spectroscopy. *J. Phys. Chem. C* 2017, **121**, 5460–5466.
- [16] Sato, S.; Kasugai, A.; Ochiai, K.; Masuda, K.; Nakamura, M.M.; Ohta, M.; Oyaidzu, M.; Kwon, S.; Sakamoto, K.; Ishida, S. Conceptual design of advanced fusion neutron source (A-FNS) and irradiation test modules. *Nucl. Fusion* 2021, **61**(10), 106026.
- [17] Lyublinski, I.E.; Evtikhin, V.A.; Pankratov, V.Y.; Krasin, V.P. Numerical and experimental determination of metallic solubilities in liquid lithium, lithium-containing nonmetallic impurities, lead and lead-lithium eutectic. *J. Nucl. Mater.* 1995, **224**, 288–292.
- [18] Hirakane, S.; Yoneoka, T.; Tanaka, S. Control of nitrogen concentration in liquid lithium by iron–titanium alloy. *Fusion Eng. Des.* 2006, **81**, 665–670.
- [19] Bo H.; Wang J.; Duarte, L.; Leinenbach, C.; Liu, L.; Liu, H.; Jin, Z. Thermodynamic re-assessment of Fe–Ti binary system. *Nonferrous Met. Soc. China* 2012, **22**(9), 2204–2211.
- [20] Metals Data Book, 4th ed., Japan Institutes of Metals, 1993.



# Observation and Analysis of Micro-Textures in Mineral Samples with an Aberration Corrected STEM

Ichiro Ohnishi EM Business Unit, JEOL Ltd.

Reduction of electron beam irradiation damage is important to observe rock and mineral samples with an aberration corrected STEM. This paper describes the experimental conditions for reducing the damage, various techniques and methods under the conditions, followed by the examples of observation and analysis of crystal structures and micro-textures in mineral samples.

## Introduction

Spatial resolution of Transmission Electron Microscopy (TEM) and Scanning TEM (STEM) has been significantly improved with the development and progress of aberration corrected technologies. The microscope with the latest aberration corrector has achieved STEM image resolution of 40.5 pm [1], and realization of atomic resolution observation has become common with the correctors. In addition, chemical analysis in atomic level with Energy Dispersive X-ray Spectroscopy (EDS) and/or an Electron Energy Loss Spectroscopy (EELS) has been realized, owing to the correctors. Since state-of-the-art industrial materials such as semiconductor materials currently have extremely fine structures, aberration corrected S/TEM enables atomic resolved observation and analysis, which is useful for the research and development of various materials.

On the other hands, there are few applications of observation and analysis for natural samples such as rock and mineral using an aberration corrected S/TEM [e.g., 2]. The main reason is that rock and mineral samples are more sensitive to electron beam irradiation compared with general industrial materials, so high resolution observation, which requires a high electron dose, is difficult for rock and mineral samples. However, observation of rock and mineral samples by conventional TEM has been performed for a long time and it has been used for research on sample structures that are difficult to study with X-ray structure analysis, optical microscope and Scanning Electron Microscope (SEM). For instance, TEM is essential to investigate defects, modulated structure, and phase transition in mineral samples [e.g., 3]. Moreover, since most of extraterrestrial materials such as meteorites and comet dust are precious and have small amounts of samples, TEM observation and analysis, which does not require large amounts of samples, is very useful and has been used for studying texture and phase identification for a long time. Recently, TEM is counted as one of the important analytical methods for asteroid sample return missions such as Hayabusa in JAXA [5] and Osiris-Rex in NASA. It is expected that observation of return samples using aberration corrected STEM will be performed in the future.

Since High Angle Annular Dark Field (HAADF) method with an aberration corrected STEM can provide not only high spatial resolution observation, but also Z contrast imaging depending on atomic number, it enables to distinguish and directly observe each atomic site in sample, which is expected to provide us a great deal of knowledge about rock and mineral samples. Although there are few examples, the distinction of occupancy of cation sites [2] and direct observations of dislocation textures [6] in rock-forming minerals using an aberration corrected STEM have been reported so far. In addition, with the recent development of large-sized Silicon Drift Detector (SDD), X-rays from samples can be detected with high sensitivity and the samples can be analyzed even under low probe current conditions, enabling chemical analysis of rock and mineral samples that are easily suffered from electron beam damage. Moreover, low dose TEM imaging using highly sensitive direct detection camera [7] and low dose STEM imaging using high speed scanning technology and/or multi segmental detector [8] have recently been utilized, and then they are expected to be applied for high resolution imaging of rock and mineral samples.

Therefore, in this paper, I will introduce various techniques and methods for observing mineral samples using aberration corrected STEM, show the results of observation and analysis of mineral samples using it so far, and explain how effective an aberration corrected STEM is for mineral samples, including future prospects.

## Observation and analysis technologies and methods required to observe mineral samples

### 1) Acceleration voltage:

When an electron beam is irradiated to a material with covalent/ionic bonding properties such as ceramics and mineral samples, the electrons in the material are excited by the incident electrons, and some of atoms in the material are ionized, resulting in a series of reactions such as structural destruction and amorphization. This is so-called radiolysis, which is considered to be the main cause of electron beam damage to ceramics and mineral samples

[9]. In order to prevent the radiolysis, it is important to reduce the probability of electron-electron reaction due to electron beam irradiation, and reducing the ionization cross section, that is, making the sample thinner or increasing the acceleration voltage can be considered. Therefore, the acceleration voltage of 200-300 kV is more effective compared with 80 kV during observation of rock and mineral samples. The observation and analysis of mineral samples in the present study were performed at an acceleration voltage of 300 kV using JEM-ARM300F [10, 11] and JEM-ARM300F2 [12], which are aberration corrected S/TEM instruments equipped with a cold field emission gun. In addition, some kinds of mineral samples contain water molecules or structural water in their structures, and they are easily damaged by heating due to electron beam irradiation, so low probe current is also an important factor for observation [9].

## 2) Low dose STEM imaging and related methods:

When we observe a sample that is relatively strong to electron beam irradiation such as SrTiO<sub>3</sub> with an aberration corrected STEM at atomic resolution, we normally observe and record images at a magnification of 40-50 M, using a probe current of 30 pA, a pixel number of 512 × 512 pixels and a pixel time of 19-38 μs/pixel. However, if we use the same condition for observing mineral samples such as silicates, we cannot get a good STEM image due to electron beam damage. In the case of mineral samples, in order to obtain an atomic resolution STEM image, it is desirable to set the conditions at least the probe current down to 20 pA or less and the pixel time down to 10 μs/pixel or faster, although it depends on the magnification and the number of pixels. It is expected that the damage of the sample will be reduced by keeping low probe current and high-speed scanning, that is, observing under the low dose conditions.

However, under such conditions, the Signal to Noise (S/N) ratio of the obtained STEM image is poor and the quality of image cannot be expected so much. In order to improve that, the image is sometimes sharpened by performing image processing such as filtering the STEM image with poor S/N ratio (Figs. 1a, b). For instance, Kogure and Okunishi [2] applied low pass and Wiener filters to atomic resolution STEM images of mineral samples obtained with low probe current, and explained that the occupancy of cation sites in minerals can be distinguished. In addition, after continuously capturing a large number of scanned images with a low probe current and high speed, the multiple scanned images are aligned and superimposed, and then a STEM image with a high S/N ratio is finally able to be obtained (Figs. 1c, d). By acquiring the STEM image at high speed, it can be expected to suppress noise and image distortion, which are problems of the scanned image, and the method is now commonly used for normal samples other than those sensitive to electron beam damage.

## 3) Highly sensitive X-ray analysis and related methods:

Even when taking X-ray images with EDS, scanning with low probe currents and high speed is also very effective. Although it depends on the EDS manufacturer, it is possible to acquire high-speed X-ray images at the highest speed of 10 μs/pixel, and using the sample drift correction function, multiple high-speed X-ray images are superimposed to make the final X-ray image. In this case the S/N ratio of each X-ray image is important similar to STEM imaging, and it is necessary to collect X-ray signals with high sensitivity in order to obtain final X-ray image with high quality. For the SDD, which is the recent mainstream EDS detector, it is possible to design large size and highly flexible shape of the detection sensor. Thus, a large-sized SDD having the shape to fit inside the microscope can be set as close as possible

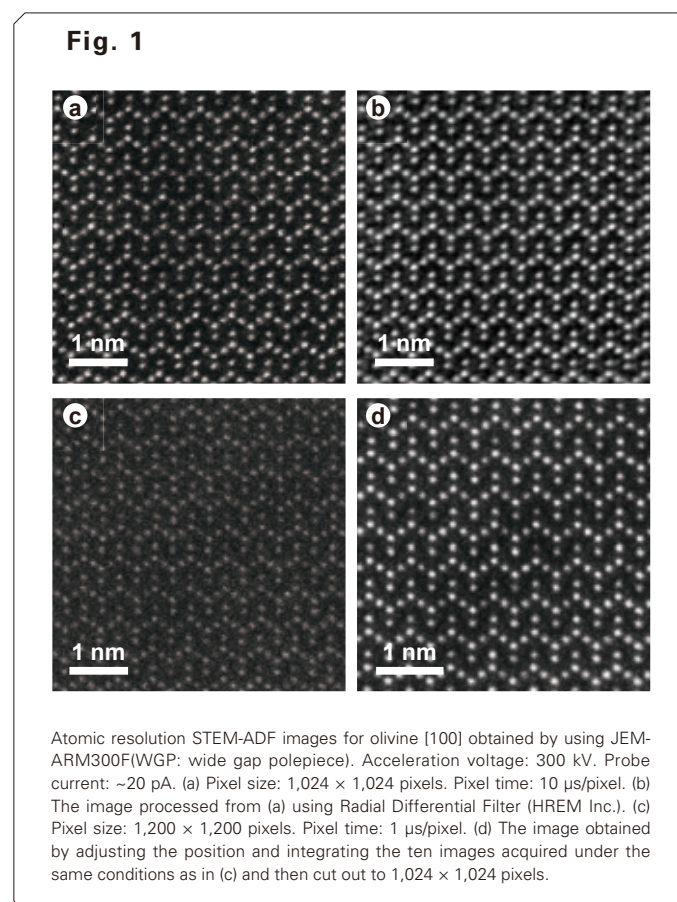
to the sample, and then it significantly improved the detection solid angle compared with the conventional Si (Li) detectors. The detection solid angle of the latest system, which is composed of two windowless SDDs with an area of 158 mm<sup>2</sup> for each sensor, reaches 2.21 steradians (sr) [13]. It achieves about 7 times higher detection sensitivity compared with the old Si (Li) detector whose detection solid angle was limited to 0.3 sr at the maximum. Thus, the SDD system with large detection solid angle allows us to take X-ray images with high S/N ratio even under the conditions with low probe currents and high-speed scanning.

Moreover, similar to STEM imaging, the image processes such as Gaussian and Wiener filters are also able to improve the quality of X-ray images. However, although the Wiener filter is very effective for periodically structured samples and fields of view, it can cause artifacts in X-ray images when used in other fields, such as the interface between two grains with different structures, and thus we need to be careful when using it. In addition, for taking atomic resolution X-ray image with high quality, other process is now also used, assuming a periodic structure and extracting a large number of images from the regions showing the same structure in the X-ray image with a large number of pixels, and finally each extracted image is aligned and superimposed to make a clear X-ray image [14].

## The results of observation and analysis for mineral samples using an aberration corrected STEM

### 1) Direct visualization of heavy and light elements in minerals using atomic resolution STEM-HAADF and ABF:

We can directly observe atomic sites in mineral samples by using an aberration corrected STEM. **Figure 2** shows atomic resolution





STEM-Annular Dark Field (ADF) and Annular Bright Field (ABF) images for [100] direction of olivine, which is one of the isolated silicate minerals. In ADF image, all the cation sites such as Mg, Fe, and Si are visualized (Fig. 2a), while, in ABF image, not only all the cation but also anion of O are visualized (Fig. 2b).

**Figure 3** shows atomic resolution STEM-ADF and ABF images for [001] direction of three kinds of amphibole, which is one of the chain silicate minerals, including grunerite, riebeckite, and tremolite-actinolite solid solution. In amphibole, there are four types of cation sites (A, B, C, and T sites) with different size, and the cation, which is suitable for each size, preferentially occupies in each site (Fig. 3g, **Table 1**). In ADF image, the difference in cation at the B and C sites is significantly observed (Figs. 3b, d, f). In grunerite, since all the seven sites in both B and C sites are occupied by Fe ions, they show the same brightness and no difference in contrast (Fig. 3b). On the other hand, in tremolite-actinolite solid solution, two B sites show brighter than five C sites (Fig. 3f). The B sites are occupied by calcium ion, which is a relatively heavy element, while the C sites can be occupied by both the light element of Mg ion and the heavy element of Fe ion. Since Mg is relatively rich in the sample, the B sites show darker than the C sites. Moreover, in riebeckite, since two B sites are occupied by the light element of Na ion and five C sites are occupied by the heavy element of Fe ion, the difference in contrast between B and C sites is large (Fig. 3d). In ABF image, not only heavy elements but also light elements such as O can be visualized and B sites (Na ion) in riebeckite, which are shown as very dark spots in ADF image, can be clearly observed (Figs. 3a, c, e).

**Figure 4** shows atomic resolution STEM-ADF and ABF images for [0001] direction of beryl (aquamarine), which is one of the ring silicate minerals. In ADF image, only Al and Si ions are observed, while in ABF image, the ultra-light element of Be is visualized as well as O, Al, and Si ions.

## 2) Direct visualization of elemental distribution in minerals using atomic resolution EDS:

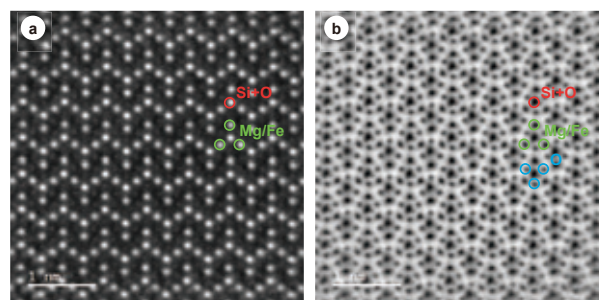
**Figure 5** shows atomic resolution STEM-ADF and ABF images for [001] direction of three kinds of pyroxene, which is one of the chain silicate minerals similar to amphibole, including diopside, hedenbergite and grossmanite. In ADF image, three types of cation sites (A, B, and T sites) (Figs. 5b, e, h, **Table 2**) are recognized similar to amphibole. In particular, the line profiles of ADF signals suggest that each cation sites show the brightness depending on atomic number (Figs. 5c, f, i).

**Figure 6** is the results showing atomic resolution EDS mapping for the boundary between diopside and hedenbergite. In diopside and hedenbergite, Ca ion occupies the A site, while, those occupy the B site are different, which are Mg and Fe, respectively. In the atomic resolution EDS map, the difference in the distribution of Mg and Fe is clearly observed at the boundary. In addition, both the Mg and Fe signals can be detected on the boundary, suggesting the possibility that both Mg and Fe ions coexist in the boundary.

**Figure 7** is the results showing atomic resolution EDS mapping for the grossmanite. Grossmanite is new pyroxene mineral, which was discovered in 2009 from Allende meteorite. Crystal structure analysis using Electron Back Scattered Diffraction (EBSD) and quantitative chemical analysis using electron micro probe analyzer have suggested that divalent Mg ion and trivalent Al and Ti ions coexist in the B site, and tetravalent Si ion and trivalent Al ions coexist in the T site in order to maintain the charge balance in the structure [15]. The atomic resolution EDS maps reveal that Mg, Ti and Al occur

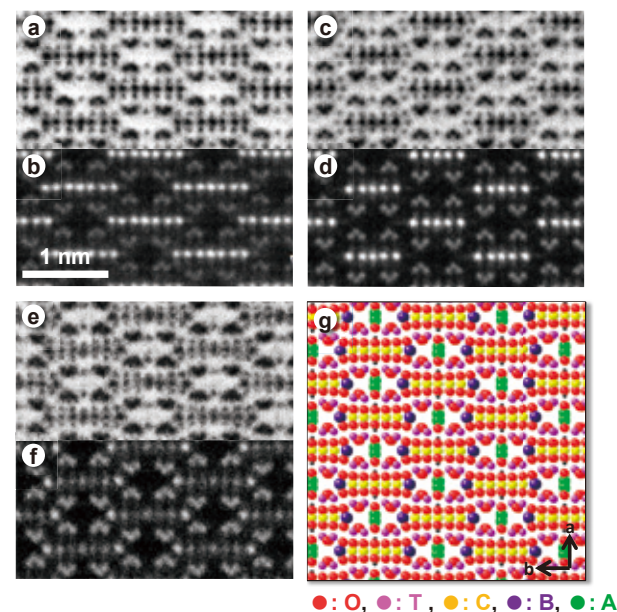
in the B site, while Al and Si occur in the T site. These results are consistent with the suggestion in the previous paper [15]. In

**Fig. 2**



Atomic resolution STEM-ADF (a) and ABF (b) images for olivine [100] obtained by using JEM-ARM300F(WGP). Acceleration voltage: 300 kV. Probe current: ~20 pA.

**Fig. 3**



Atomic resolution STEM-ADF (b, d, f) and ABF (a, c, e) images and ideal structure model (g) of three kinds of amphibole [001]. (a, b) Grunerite, (c, d) Riebeckite, (e, f) Tremolite-actinolite solid solution. The STEM images were obtained by using JEM-ARM300F(WGP) at an acceleration voltage of 300 kV and a probe current of ~15 pA.

**Table. 1 Chemical composition and ion species in each cation sites in three kinds of amphibole.**

Table 1	Grunerite	Riebeckite	Tremolite-Actinolite
Chemical Formula	$\text{Fe}^{2+}_7\text{Si}_6\text{O}_{22}(\text{OH})_2$	$\text{Na}_2(\text{Fe}^{2+}_3, \text{Fe}^{3+}_2)\text{Si}_6\text{O}_{22}(\text{OH})_2$	$\text{Ca}_2(\text{Mg}, \text{Fe}^{2+})_5\text{Si}_6\text{O}_{22}(\text{OH})_2$
A	□	□	□
B	$\text{Fe}^{2+}$	$\text{Na}^+$	$\text{Ca}^{2+}$
C	$\text{Fe}^{2+}$	$\text{Fe}^{2+}, \text{Fe}^{3+}$	$\text{Mg}^{2+}, \text{Fe}^{2+}$
T	$\text{Si}^{4+}$	$\text{Si}^{4+}$	$\text{Si}^{4+}$

Amphibole general chemical formula:  $\text{A}_{0-1}\text{B}_2\text{C}_5\text{T}_8\text{O}_{22}(\text{OH}, \text{F})_2$



addition, although it is a little unclear, even the X-ray image of O shows distribution reflecting the crystal structure of pyroxene.

### 3) Microstructure of olivine in meteorite:

**Figure 8** shows the results of the aberration corrected STEM observation and high-resolution EDS mapping for [001] direction of Fe-rich olivine in the matrix of Allende meteorite. Fe-rich olivine is a major constituent mineral of the Allende matrix and it occurs as fine grain (~a few micrometers in size) in the matrix. Recent study has reported that platy thin precipitates (1-2 nm in thickness) commonly occur in the olivine grains [16]. And aberration corrected STEM observations for TEM thin films from the specific orientations of the olivine grains, which were made by using the combination of EBSD and a focused ion beam method, have confirmed that the long direction of the precipitate is always oriented perpendicular to the *a*-axis of the host olivine [17]. The STEM-ADF images (Figs. 8b-d) indicate that the precipitates show brighter than the host olivine, suggesting that the precipitates are enriched in heavy elements compared with olivine. The results of EDS mapping show that the precipitates are rich in Fe, Cr, and Al and poor in Si and Mg compared with the host olivine (Figs. 8e-j), suggesting that the precipitate is probably Cr-rich Fe oxide (Cr spinel). Based on the previous study, such platy spinel precipitates, which occur perpendicular to the *a*-axis of the host olivine, are inferred to be formed by the oxidation of olivine at high temperature. Thus, it suggests that Allende matrix have experienced such oxidation process at high temperature [16]. In this way, phase identification of precipitates with a thickness of 1-2 nm is a unique result of using an aberration corrected STEM. I believe that an aberration corrected STEM is significantly useful for observation and analysis of microstructure in rock and mineral samples, including meteorite and so on.

## Summary and Future Prospects

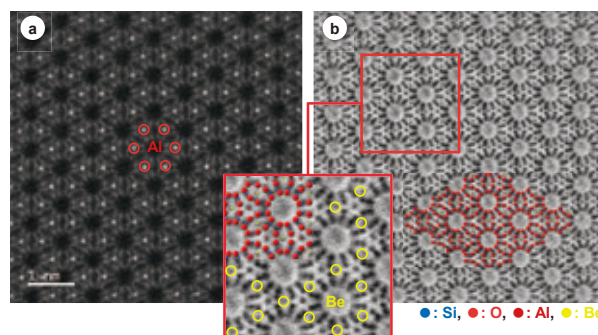
As mentioned above, an aberration corrected STEM is very effective method to study crystal structure, texture and elemental distribution at nanometer to sub-nanometer-sized level in rock and mineral samples. However, as explained before, it is important to reduce sample damage due to electron beam irradiation such as low dose conditions in order to observe and analyze them. It is expected that new technologies and methods such as EDM and OBF will help to reduce sample damage.

EDM is an abbreviation for Electron Dose Modulator, which is a technology that can arbitrarily change the current of electron beam irradiated on a sample by using an electrostatic shutter installed just under electron gun at the fastest speed of a few 10 ns. It is possible to synchronize with the scanning of STEM and control the amount of electron beam irradiation to the sample in one-pixel units. In principle, it is possible to irradiate different doses for each atom, and it is expected that the electron beam damage during observation and analysis of a sample will be further reduced.

OBF is an abbreviation for Optimum Bright Field, which is a new STEM observation method developed by university of Tokyo [8]. In the OBF method, a spatial frequency filter, which is optimized to maximize S/N ratio, is applied to each segmental STEM image obtained by multi-segmental STEM detector, and then it is possible to obtain the STEM image with higher sensitivity compared with conventional ADF and ABF methods. Thus, this method allows us to observe a sample under much lower dose conditions than before, and it starts to be applied to the observation of highly beam sensitive materials such as

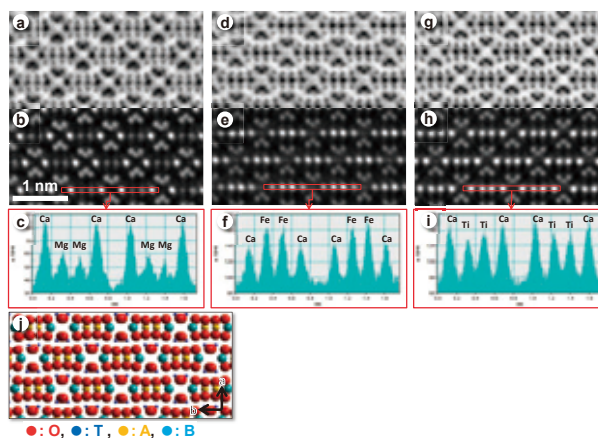
zeolite and MOF (Metal Organic Framework). **Figure 9** shows STEM-OBF image of pyroxene (enstatite) in the [001] direction obtained by using the combination of an aberration corrected STEM and an eight segmental STEM detector. The crystal structure of pyroxene has been clearly observed with very high S/N ratio even using a probe current of 2 pA, which is much

**Fig. 4**



Atomic resolution STEM-ADF (a) and ABF (b) images for beryl [0001] obtained by using JEM-ARM300F(WGP). Acceleration voltage: 300 kV. Probe current: ~5 pA.

**Fig. 5**



Atomic resolution STEM-ADF (b, e, h) and ABF (a, d, g) images and ideal structure model (j) of three kinds of clinopyroxene [001], and line profiles of ADF signals in A and B sites (c, f, i). (a, b, c) Diopside, (d, e, f) Hedenbergite, (g, h, i) Grossmanite. The STEM images were obtained by using JEM-ARM300F(WGP) at an acceleration voltage of 300 kV and a probe current of ~15 pA.

**Table. 2 Chemical composition and ion species in each cation site in three kinds of clinopyroxene.**

Table 2	Diopside	Hedenbergite	Grossmanite
Chemical Formula	$\text{CaMgSi}_2\text{O}_6$	$\text{CaFe}^{2+}\text{Si}_2\text{O}_6$	$\text{Ca}(\text{Mg}^{2+}, \text{Al}^{3+}, \text{Ti}^{3+})_2(\text{Al}^{3+}, \text{Si})_2\text{O}_6$
A	Mg	$\text{Fe}^{2+}$	$\text{Mg}^{2+}, \text{Al}^{3+}, \text{Ti}^{3+}$
B	$\text{Ca}^{2+}$	$\text{Ca}^{2+}$	$\text{Ca}^{2+}$
T	$\text{Si}^{4+}$	$\text{Si}^{4+}$	$\text{Al}^{3+}, \text{Si}^{4+}$

Clinopyroxene general chemical formula:  $\text{ABT}_2\text{O}_6$

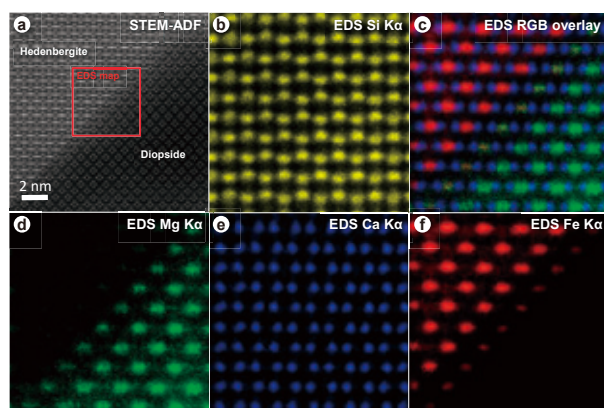
lower than before. Thus, the OBF method is also expected to be very useful for observing mineral sample.

The combination of an aberration corrected STEM, EDM and OBF method will be expected to enable us to directly observe atomic sites as well as micro-textures and crystal structures in mineral samples under much lower dose conditions. And thus, I hope that it can make a great contribution to research in the fields of Earth science and/or planetary material science.

## Acknowledgments

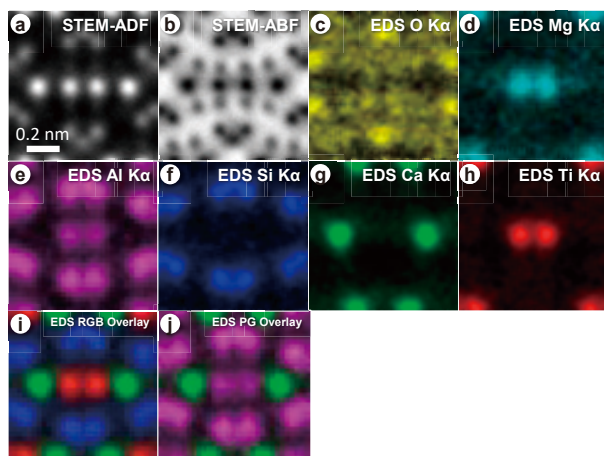
I am grateful to Prof. K. Tomeoka in Kobe University for donating the Allende meteorite sample. I also thank M. Kadoi in JEOL for the preparation of the TEM specimen of the Allende meteorite and Dr. M. Yoshitake in Japan Aerospace Exploration for the preparation of the TEM specimen of clinochlore using focused ion beam.

**Fig. 6**



Atomic resolution STEM-ADF image (a) for the boundary between diopside and hedenbergite and EDS elemental maps of red box in Fig. 6a (b-f) (b: Si K $\alpha$ , c: RGB Overlay (Red: Fe K $\alpha$ , Green: Mg K $\alpha$ , Blue: Ca K $\alpha$ ), d: Mg K $\alpha$ , e: Ca K $\alpha$ , f: Fe K $\alpha$ ). The STEM images and elemental maps were obtained by using JEM-ARM300F(WGP) and 158 mm<sup>2</sup> Dual SDD at 300 kV.

**Fig. 7**

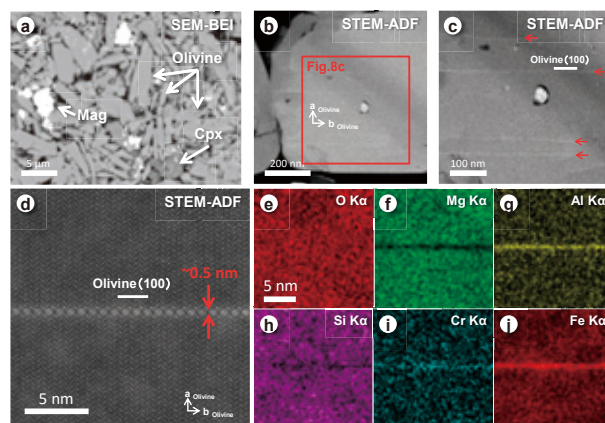


Atomic resolution STEM-ADF (a) and ABF (b) images and EDS elemental maps (c-j) for the grossmanite, obtained by using JEM-ARM300F(WGP) and 158 mm<sup>2</sup> Dual SDD at 300 kV (c: O K $\alpha$ , d: Mg K $\alpha$ , e: Al K $\alpha$ , f: Si K $\alpha$ , g: Ca K $\alpha$ , h: Ti K $\alpha$ , i: RGB Overlay (Red: Ti K $\alpha$ , Green: Ca K $\alpha$ , Blue: Si K $\alpha$ ), j: PG Overlay (Pink: Al K $\alpha$ , Green: Ca K $\alpha$ )). The STEM images and elemental maps were obtained by adjusting the position and integrating the 24 images with 64 × 64 pixels, having the same periodical structure, extracted from an original EDS map with 256 × 256 pixels.

## References

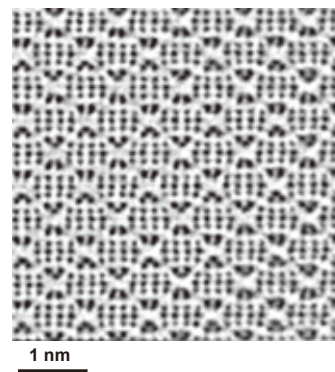
- [ 1 ] S. Morishita *et al.*, *Microscopy* **67** (2017) 46-50.
- [ 2 ] T. Kogure and E. Okunishi, *Microscopy* **59** (2010) 263-271.
- [ 3 ] H.-R. Wenk (Ed.), *Electron Microscopy in Mineralogy*, Springer-Verlag (1976).
- [ 4 ] M. Zolensky *et al.*, *Science* **314** (2006) 1735-1739.
- [ 5 ] T. Nakamura *et al.*, *Science* **333** (2011) 1113-1116.
- [ 6 ] A. Kumamoto *et al.*, *Microscopy* **63** (2014) Suppl i17.
- [ 7 ] Y. Zhu *et al.*, *Nature Materials* **16** (2017) 532-536.
- [ 8 ] K. Ooe *et al.*, *Ultramicroscopy* **220** (2021) 113133.
- [ 9 ] D.B. Williams and C. B. Carter, *Transmission Electron Microscopy A Textbook for Material Science*, Second Edition, Springer (2009).
- [ 10 ] H. Sawada *et al.*, *JEOL News* **49** (2014) 51-58.
- [ 11 ] E. Okunishi *et al.*, *JEOL News* **50** (2015) 58-63.
- [ 12 ] Y. Jimbo *et al.*, *JEOL News* **52** (2011) 30-35.
- [ 13 ] I. Ohnishi *et al.*, *e-J. Surf. Sci. Nanotech.* **16** (2018) 286-288.
- [ 14 ] A. Kumamoto, *AMTC4* **4** (107) (2014) 270.
- [ 15 ] C. Ma and G.E. Rossman, *American Mineralogist* **94** (2009), 1491-1494.
- [ 16 ] I. Ohnishi *et al.*, *Meteoritics & Planetary Science* **53** (2018), 6105.
- [ 17 ] Kadoi *et al.*, *JEOL News* **56** (2021), 50-55.

**Fig. 8**



Back-scattered electron image (BEI) of the Allende matrix (a) (Mag: magnetite, Cpx: Ca-rich pyroxene), STEM-ADF images (b-d) and high-resolution EDS elemental maps (e-j) for olivine in the matrix (e: O K $\alpha$ , f: Mg K $\alpha$ , g: Al K $\alpha$ , h: Si K $\alpha$ , i: Cr K $\alpha$ , j: Fe K $\alpha$ ). The STEM images and elemental maps were obtained by using JEM-ARM300F(WGP) and 158 mm<sup>2</sup> Dual SDD at 300 kV.

**Fig. 9**



Atomic resolution STEM-OBF image for Mg pyroxene [001], obtained by using JEM-ARM300F2(FHP2) with the eight segmental STEM detector at an acceleration voltage of 300 kV and a probe current of ~2 pA.



# New Semi-in-lens SEM JSM-IT800 Excellent for Semiconductor Device Observation

Motohiro Nakamura and Yuhei Nakajima EP Business Unit, JEOL Ltd.

We have developed two new versions, *i* and *is*, of the JSM-IT800, a Schottky field emission scanning electron microscope. Both are equipped with a new semi-in-lens objective lens and an upper in-lens detector (UID) optimized for the objective lens for efficient detection of secondary electrons. They continue to support the upper electron detector (UED) and scintillator backscattered electron detector (SBED) incorporated in the JSM-IT800 for simultaneous acquisition of multiple sets of specimen surface information. Furthermore, both feature low vacuum (LV) imaging, which was not supported by the conventional JSM-7610FPlus with a semi-in-lens objective lens, allowing for observation of insulator specimens without coating a specimen. With these functions, the JSM-IT800 *i*/*is* is effective for acquiring voltage contrast images (VC images) needed for semiconductor failure analysis and for high-resolution observation of specimen edges, tilt specimens, and insulators.

## Introduction

A scanning electron microscope (SEM) is designed for imaging the specimen surface by scanning an electron beam and detecting resulting secondary electrons and backscattered electrons. The JSM-IT800, JEOL's latest SEM, is equipped with an "In-lens Schottky Plus field emission electron gun," which enables high current high-resolution imaging, "Neo Engine", a next generation electron optics control system, and "SEM Center," an intuitive GUI fully integrated with JEOL's proprietary EDS [1]. It also supports a wide range of specimen sizes, featuring a maximum mountable specimen size of up to 200 mm in diameter and 55 mm in height.

The JSM-IT800 series offers different models depending on the type of objective lens used; hybrid lens *HL*, which is a general-purpose SEM with an objective lens superimposes electromagnetic field on electrostatic field, and super hybrid lens *SHL*/*SHLs* for a high-end SEM with the same objective lens (**Fig. 1**). *SHL* and *SHLs* have better spatial resolution than *HL* because of stronger electric field applied to the objective lens. In addition to these, we have developed *i* and *is* featuring a new semi-in-lens objective lens.

In this article, we will introduce major features of the JSM-IT800 *i*/*is*, including its objective lens and detectors, as well as analytical data acquired from semiconductor devices utilizing these features.

## 1. Characteristics of JSM-IT800 *i*/*is*

The JSM-IT800 *i*/*is*, which was developed based on the JSM-7610FPlus, is a conventional semi-in-lens SEM featuring high resolution imaging and acquisition and selecting of electrons by a secondary electron detector in its objective lens. The JSM-

IT800 *i*/*is* integrates the objective lens and detection system of the JSM-7610FPlus, which have been upgraded.

### 1.1. Semi-in-lens Objective Lens and UID Detector

The semi-in-lens objective lens used in the JSM-IT800 *i*/*is* features an objective lens yoke designed to form a magnetic field near the specimen to reduce aberrations. Although the magnetic field present around the specimen compromises low magnification observation and EBSD analysis, it also provides advantages in signal detection, which will be described

**Fig. 1 External View of JSM-IT800.**



This photo shows the *i*.



later. On the other hand, <HL> and <SHL>/<SHLs> use an electromagnetic field superimposed objective lens, which reduces aberrations by superimposing electric and magnetic fields. In this structure, an electrode is provided inside the magnetic field created by an out-lens objective lens, constructing an electrostatic lens. In the electromagnetic field superposed lens, the objective lens magnetic field around the specimen is extremely small compared with the semi-in lens, making it especially suitable for low magnification imaging and EBSD analysis.

The lens magnetic field around the specimen can be used to collect and detect secondary electrons efficiently. In the out lens, if the electromagnetic field around the specimen is negligible, secondary electrons emitted from the specimen travel straight, most of which collide with and are absorbed by the specimen chamber or objective lens outer yoke. In the semi-in lens, where a strong magnetic field exists as described above, secondary electrons generated from the specimen surface are spirally rotated and sucked into the objective lens. This characteristic is also effective for capturing secondary electrons generated from a largely inclined specimen surface and walls or a bottom of a large uneven structure, resulting in clear secondary electron images of these surfaces.

The JSM-IT800 <i>/<is> is equipped with a UID detector in the objective lens in order to efficiently detect electrons sucked into the objective lens (Fig. 2). The UID detector is composed of an ET (Everhart-Thornley) detector inserted into holes on the objective lens yoke and UID filter electrodes placed in the lower part and inside of the objective lens for collecting and selecting electrons. Since the energy range of the detected electrons changes according to the voltage setting of these electrodes, the image acquired by the UID detector also changes. In the SE+BE mode (Fig. 2 (a)), a positive voltage is applied to the lower electrode. The positive voltage and the magnetic field of the semi-in-lens can efficiently draw numerous secondary electrons

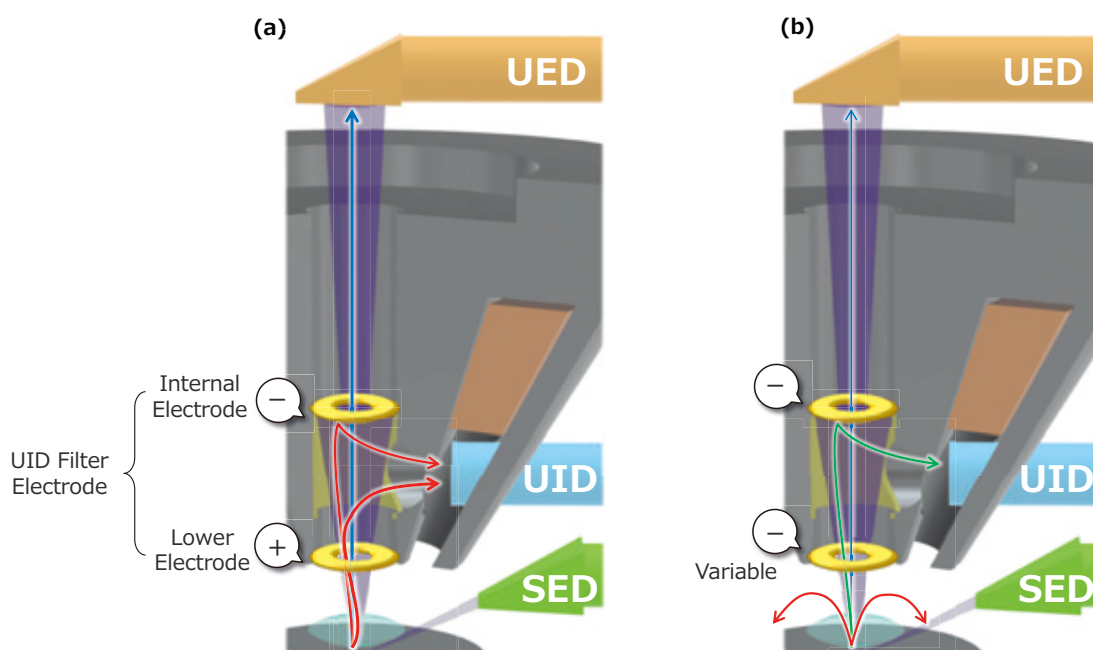
and part of backscattered electrons into the objective lens, making it possible to observe secondary electron dominated images with a large amount of signals suitable for shape observation. On the other hand, in the BE mode (Fig. 2 (b)), a negative voltage is applied to the lower electrode, preventing electrons with low energy from penetrating the objective lens. This makes it possible to remove electrons with low energy, which are susceptible to charging, and acquire a backscattered electron image that shows topography and composition. In addition, the UID detector, being installed in the objective lens, can efficiently guide and detect electrons in the objective lens at a short working distance (WD), which can further reduce aberrations of the primary electron beam, resulting in high-resolution imaging.

Such characteristics of the semi-in-lens and UID allows the <i>/<is> to identify wiring defects using VC images needed for semiconductor failure analysis. Furthermore, the <i>/<is> is superior in high-resolution observation of tilted specimens necessary for examination of semiconductor writing patterns and cross sections of semiconductor devices fabricated by FIB.

## 1.2. Specimens Stage Bias Voltage

The JSM-IT800 <i>/<is> has a function of applying a negative bias voltage to the specimen stage (Beam Deceleration: BD). This reduces aberrations of the electron beam and enables high spatial resolution imaging even at low acceleration voltage by decelerating the primary electron beam just before it enters the specimen. Since the applicable bias is up to -2 kV for <i>/<is> and up to -5 kV for <i>/<is>, <i>/<is> can perform higher resolution observation than <i>/<is>. In other versions, the applicable stage voltage is up to -2 kV for <HL> and <SHLs>, and up to -5 kV for <SHL>. The BD mode is effective because when the specimen is not tilted, the primary electron beam is decelerated

**Fig. 2 Structure of Semi-in-lens Objective Lens and UID Detector.**



(a) Electron orbital in the SE+BE mode designed to detect secondary electrons and backscattered electrons with the UID. Backscattered electrons emitted at a high angle (blue arrow), being less affected by the UID filter electrodes, are detected by the UED. Secondary electrons (red arrows) are drawn into the objective lens by a positive potential of the UID lower filter electrode, guided to the internal electrode, and detected by the UID. (b) Electron orbital in the BE mode designed to detect backscattered electrons by the UID. Backscattered electrons emitted at a high angle (blue arrow) are detected by the UED in the same manner as in the SE+BE mode. Secondary electrons (red arrows) do not enter the objective lens and return to the specimen or are detected by the SED detector when the lower electrode of the UID filter is set to a negative potential. The orbit of the backscattered electrons (green arrow) is controlled by the internal electrode of a negative potential and detected by the UID.

by a uniform electric field just before the specimen. However, the BD mode is less effective for highly tilted specimens or specimen edges due to astigmatism resulting from the disturbance of the electric field, unsuitable for high-resolution observation. Even in such cases, the semi-in-lens objective lens of *<i>/</i>*, with its small aberrations, makes high-resolution observation possible without applying a stage bias voltage.

### 1.3. Detectors Supported

The JSM-IT800 *<i>/</i>* supports the detectors shown in Fig. 3 besides the UID. The secondary electron detector (SED) is an ET detector, which captures relatively energetic secondary electrons emitted from the specimen and backscattered electrons emitted at a low angle close to the specimen surface, and visualizes surface topography and specimen edges.

The UED is arranged above the objective lens. The UED, located above the UID, detects electrons that have passed through the UID filter electrodes. The detected electrons are secondary electrons and backscattered electrons emitted from the specimen at a near-vertical angle when no specimen stage bias voltage is applied. At this point, it is also possible to acquire only the backscattered electron image by eliminating low energy electrons by the energy filter provided in the UED detector. The backscattered electron image thus obtained strongly reflects the composition and crystal orientation with less surface irregularities. When a specimen stage bias voltage is applied, it accelerates secondary electrons, allowing the UED to detect secondary electrons efficiently and acquire high-resolution images.

The SBED is a detector inserted between the objective lens and specimen as needed to acquire backscattered electron images. The SBED can detect backscattered electrons at an angle range that cannot be detected by the SED or UED, acquiring images that integrate topography and composition information. In addition, the SBED is characterized by its excellent responsiveness during live image observation and high sensitivity at low acceleration voltages.

The SED, UED and SBED are common to all models of the IT800 series [2].

### 1.4. Low Vacuum Mode

Like other models of the IT800 series, the JSM-IT800 *<i>/</i>* features the low vacuum (LV) mode, which was not supported in the conventional JSM-7610FPlus. Normally, SEM observation is performed with a high vacuum (up to  $10^{-4}$  Pa)

around the specimen. The LV mode is a method of observing in a pressure range from 10 Pa to 300 Pa by introducing nitrogen gas into the specimen chamber (Fig. 4). Since the inside of the SEM column must be kept at a high vacuum, a differential pumping orifice is inserted into the lower part of the objective lens. Secondary electrons emitted from the specimen ionize nitrogen gas molecules to produce more electrons. These electrons are amplified by electron avalanche caused by the bias-voltage applied to a low-vacuum secondary electron detector (LVSED), and are detected and imaged as an absorbed current. Furthermore, backscattered electrons, which have a longer mean free path than the secondary electrons due to their high energy, can be imaged by utilizing the mechanism of the backscattered electron detector for high vacuum in the LV mode. The JSM-IT800, featuring a low-vacuum backscattered electron detector (LVBED) integrated in the lower part of the differential pumping orifice, acquires backscattered electron images at a short WD in the LV mode. Since nitrogen ions neutralize the negative charges of the specimen, the LV mode is effective for observing charge-sensitive specimens.

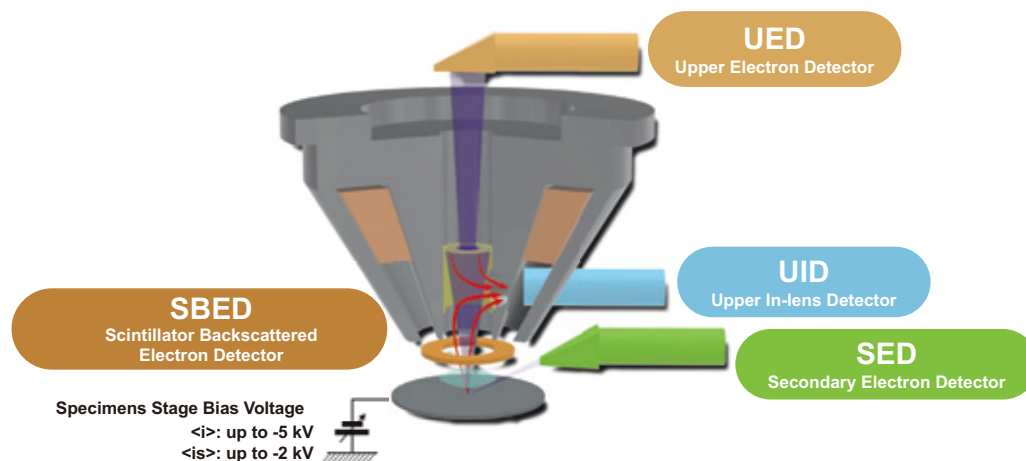
## 2. Observation of Semiconductor Devices by Various Detectors

As described so far, the detectors for the JSM-IT800 *<i>/</i>* acquire various information by separating electrons emitted from the specimen according to the energy and emission angle. In this section, we will introduce useful information obtained by selecting detectors appropriate for the research objective of various semiconductor devices.

### 2.1. Polished Surface of a Semiconductor Chip (SRAM) (Detectors Used: UID, UED, SED)

Various information can be acquired from the surface of a semiconductor chip polished to expose plugs using the UID, UED, and SED on the JSM-IT800 *<i>/</i>*. Figure 5 shows the surface of tungsten (W) plugs exposed by polishing a SRAM. Figure 5 (a) shows a VC image acquired by the UID [3]. Bright W-plugs (marked by yellow arrows) indicate low resistance, while dark W-plugs (marked by white dotted line arrows) indicate high resistance. Such contrast occurs due to the potential difference between W-plugs by electron beam irradiation because the resistance of W-plugs varies according to the conductivity of the substrate. Therefore, the potential difference determines

Fig. 3 Detection System of JSM-IT800 *<i>/</i>*.



the generation efficiency of secondary electrons. Since detection efficiency is high for low energy secondary electrons, the UID can demonstrate the difference in generation efficiency of secondary electrons, resulting in the VC image shown in Fig. 5 (a).

**Figure 6** shows a defect of a plug structure identified in the VC image. While bright and dark plugs are observed in a regular pattern according to the conductive state, the defect is marked by a bright plug where a dark plug should be. Figure 5 (b) shows a compositional contrast obtained from high-angle backscattered electrons detected by the UED showing the difference in mean atomic number. W-plugs, having a large mean atomic number, are bright, while SiO<sub>2</sub>, which is an insulator around W-plugs, is dark. The compositional difference reflects the positions of W-plugs. Figure 5 (c) shows a topographic image obtained from secondary electrons and low-angle backscattered electrons with relatively high energy detected by the SED. The image shows fine unevenness of the specimen surface caused by polishing (marked by arrows). As shown above, the JSM-IT800 can acquire multiple signals simultaneously allowing for efficient examination of specimen surface information.

## 2.2. Semiconductor Pattern (Detector Used: UID)

In semiconductor failure analysis, the specimen is cleaved and its tilted cross-section is observed to examine the shape of sides or bottom of a deeply recessed trench. However, in this case, it is necessary to detect the secondary electrons generated from the sides or bottom of the trench efficiently. The UID is effective for this application since it detects secondary electrons efficiently after they are sucked into the objective lens by a magnetic field formed in the vicinity of the specimen. **Figure 7** shows the observation result. At the bottom of the trench on the semiconductor pattern is residual resist (marked by yellow dotted circles) on the Si substrate, which should have been removed.

## 2.3. Cross-section of Laminated Semiconductor Chip Processed with FIB (Detector Used: SBED)

A semiconductor laminated chip has a structure in which fine elements and wires are laminated. In order to confirm whether the structure is made as designed, a cross-section is created and observed by SEM. Here, a cross-section of a SRAM is ion-milled by the focused ion beam (FIB) into a box-shape, and

**Fig. 4 Principle and Structure of Low Vacuum System.**

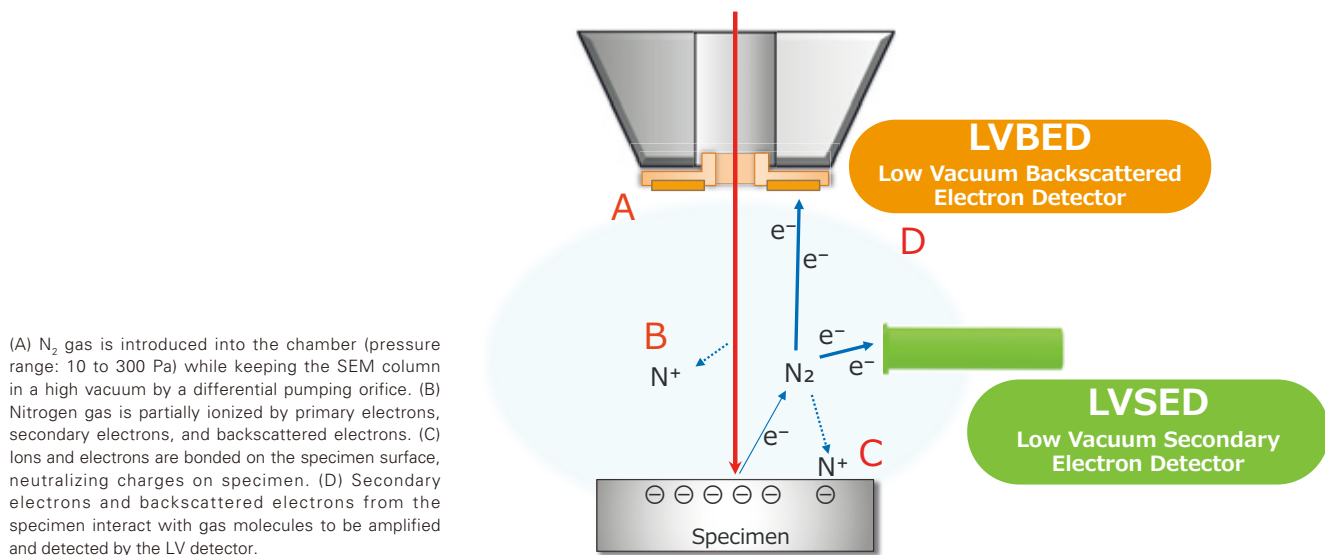
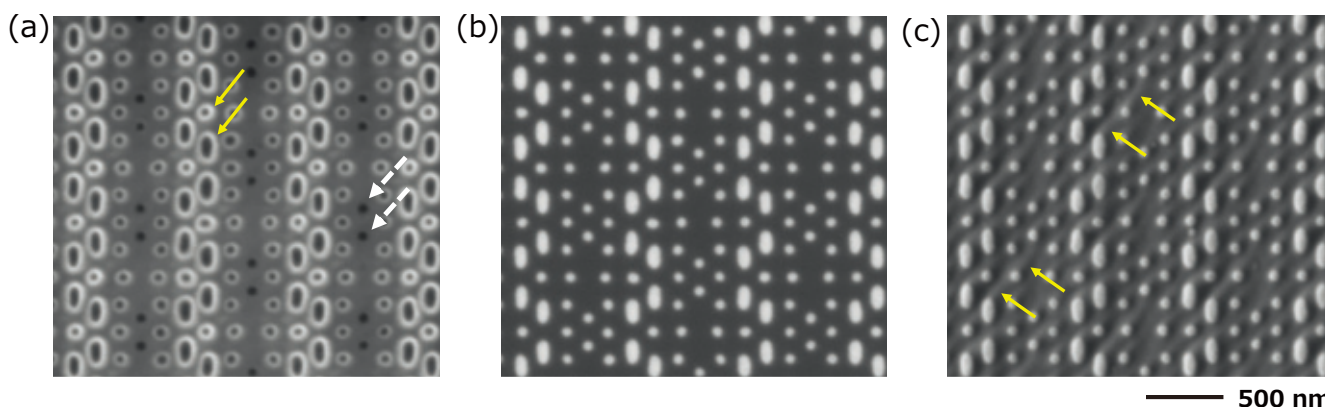


**Fig. 5 Observations of Polished Semiconductor Chip (SRAM) Using UID, UED, and SED.**



Signals from three detectors were acquired simultaneously. Landing voltage: 1 kV.

(a) Voltage contrast indicating the difference in resistance between plugs acquired by UID. Plugs with a bright rim (marked by yellow arrows) have low resistance, while plugs with a dark rim (marked by white dotted arrows) have high resistance. (b) Compositional image acquired by UED. W-plugs are bright while the insulator, SiO<sub>2</sub> is dark, reflecting the difference in generation efficiency of backscattered electrons. (c) Topographic image acquired by SED. The image shows fine unevenness on the specimen surface generated by polishing (marked by yellow arrows).



was observed while tilted. Observation by the SBED, which can detect backscattered electrons, is useful for obtaining compositional and topologic information of this cross-section.

**Figure 8** is a backscattered electron image of the SRAM cross-section processed with FIB and observed by the SBED. The image demonstrates the compositional contrast between Aluminum (Al) wires, W-plugs, and interlayer dielectrics (SiO<sub>2</sub>) as well as the topographic contrast of the shape of a void in the center of the W-plug.

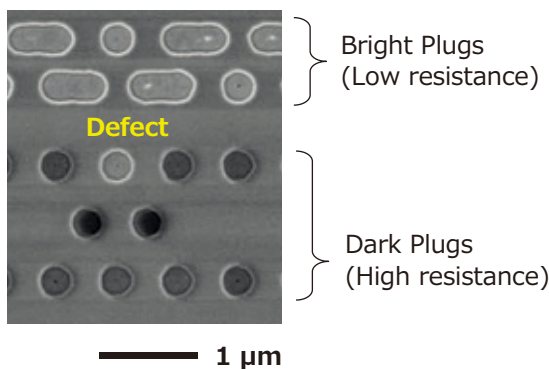
**2.4. Defect on Gold Plating (Detectors Used: UED, SBED)**

Gold plating is used to form terminals or pads of connectors in semiconductor devices. Any surface contamination on gold plating results in conduction failure. Therefore, it is important to examine surface information from gold plating. **Figure 9** (a) shows an optical microscope image of a stain-like defect (marked by an arrow) on gold plating. To confirm the composition contrast of the surface of this defect, it is effective to obtain an image with enhanced composition contrast by the UED.

Also, in order to observe the specimen surface, observation at low landing voltage is effective, since the region of scattered electrons in the specimen is smaller at low landing voltage. **Figure 9** (b) and (c) show the results of observing the defect on this gold plating with the UED at landing voltages of 5 kV and 700 V respectively. There are areas with darker compositional contrast (marked by yellow arrows) in the UED compositional image at 5 kV in (b) than the surroundings. This suggests that there are substances with a smaller mean atomic number than Au. Moreover, the UED compositional image at 700 V in (c) shows compositional information of the upper surface that was acquired at 5 kV, confirming the substance having a smaller average atomic number than Au in wider areas (dark portion inside yellow dotted circles). Here, attention was focused on areas A, B, and C on the gold plating. A is bright on the compositional image at 5 kV and shows dark compositional contrast at 700 V. B shows both dark contrast at 5 kV and 700 V. C is brighter than B on the compositional image at 5 kV and shows dark compositional contrast at 700 V.

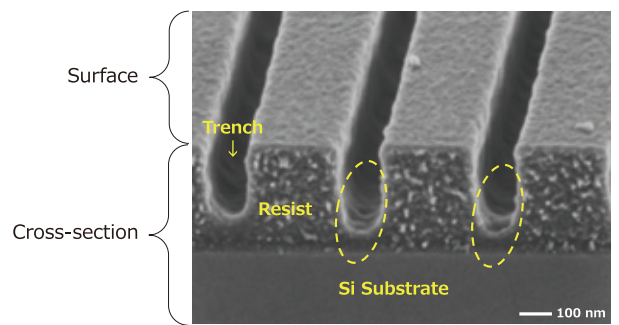
Cross-sections were fabricated with FIB for each, and layered

**Fig. 6 Identification of a defect of Semiconductor Chip (SRAM) Using UID.**



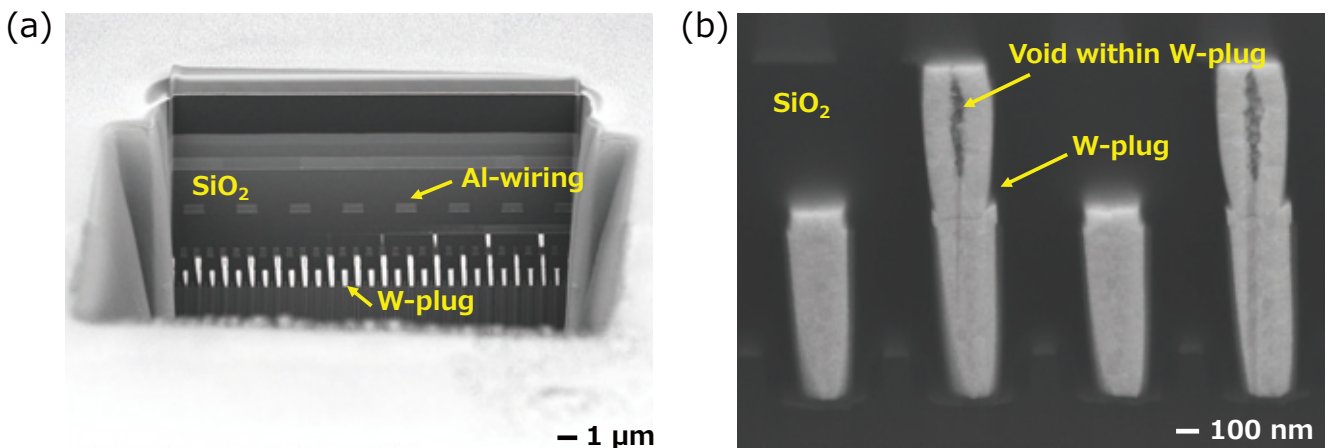
The voltage contrast detected by the UID shows bright plugs and dark plugs in a regular pattern according to the conductive state of the W plugs exposed by polishing. A defect was identified by a bright plug located where a dark plug should be. Landing voltage: 1 kV.

**Fig. 7 Observation of Semiconductor Pattern Using UID.**



A fractured semiconductor pattern was observed while tilted. The specimen was osmium-coated to reduce charge accumulation. The image shows the surface and cross section of resist as well as the fine topographic contrast of the sides and bottom of the trench. Close observation of the trench reveals residual resist (marked by yellow dotted line circles) on the Si substrate. Landing voltage: 1 kV.

**Fig. 8 Observation of a Cross-section of FIB-processed Semiconductor Laminated Chip Using SBED.**



A cross section of a semiconductor laminated chip processed by FIB was observed while tilted. (a) Compositional contrast of W-plugs, Al-wiring, inter layer dielectrics (SiO<sub>2</sub>), etc. was confirmed. Landing voltage 3 kV. (b) Compositional contrast of W plugs as well as topographic contrast indicating the shape of the void in the center was confirmed. Landing voltage: 10 kV.

structures were observed with the SBED (Fig. 9 (d)). Before cross-sectional preparation by FIB, tungsten (W), chromium (Cr), and carbon (C) were deposited on the specimen surface to protect it from the ion beam. It is confirmed that, in all of the cross sections of A, B, and C, there is a layer having a smaller mean atomic number shown by a dark compositional contrast between the Au layer and the W protective deposition of the specimen. The layer is thicker in the order of  $B > C > A$ . Figure 9 (e) shows the results of EDS elemental analysis of the cross section of B. Ni and O were detected from the layer between the Au layer and the W protective deposition.

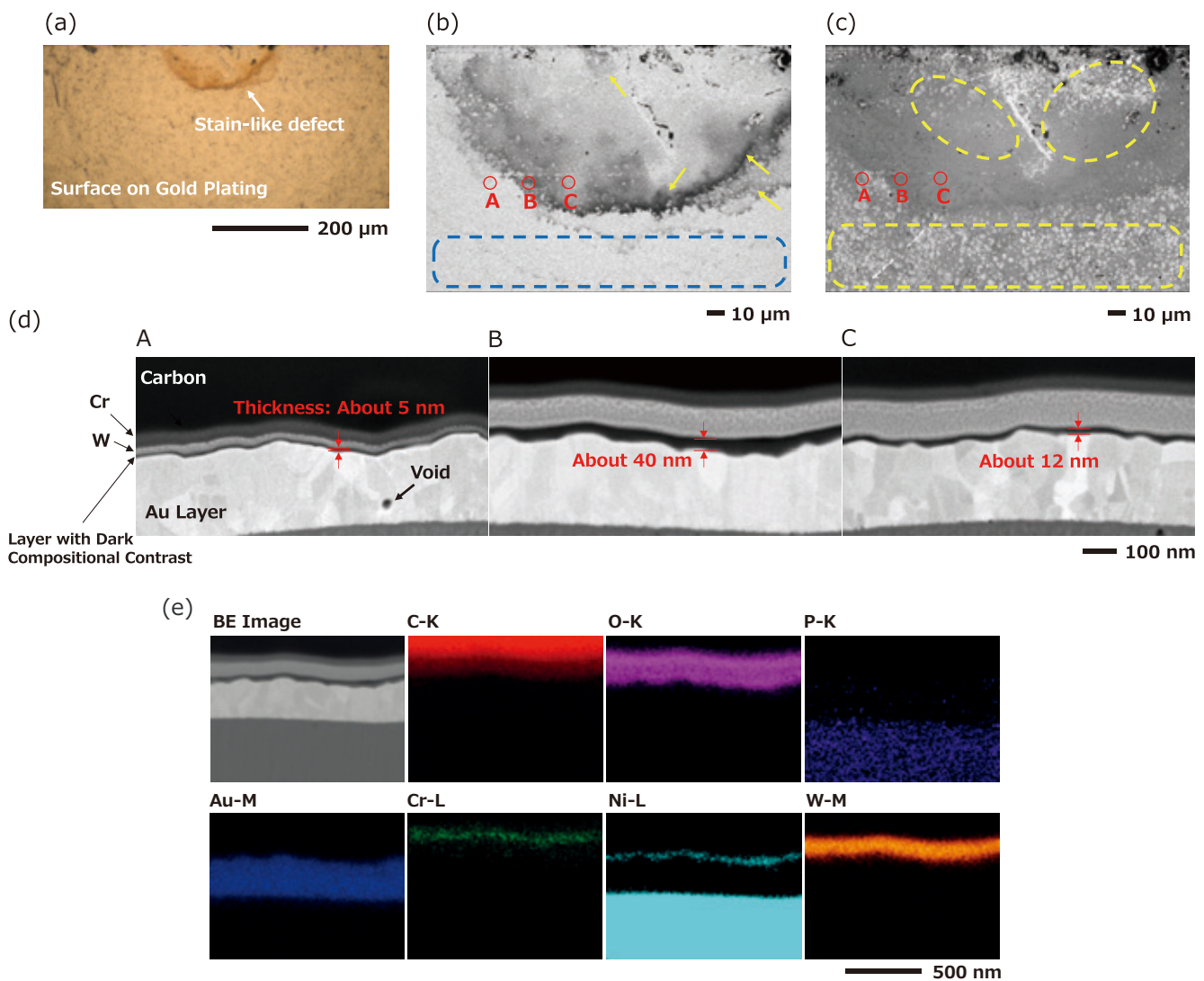
The Monte Carlo simulation software CASINO v2.51 was used to simulate the penetration depth of the incident electron beam when electrons were irradiated into nickel oxide (NiO) at landing voltages of 5 kV and 700 V (Fig. 10). The results show that at 5 kV, the maximum penetration depth of incident electron beam is about 200 nm, while at 700 V, it is shallower and about 12 nm.

When the specimen surface is covered with a Ni and O layer, even if it is 40 nm thick as at B in Fig. 9 (d), the incident electron beam scatters deeper and reaches the Au layer. At A, where Ni and O layer is about 5 nm thick and at C, where Ni and O layer is about 12 nm thick, more incident electrons reach the Au layer while more backscattered electrons are generated from the Au layer. Therefore, on the compositional image at 5 kV in Fig. 9 (b), the compositional contrast is brighter in the order of  $A > C > B$ . On the other hand, on the compositional image at 700 V in Fig. 9 (c), the maximum penetration depth of the electron beam is smaller, and even the thin Ni and O layer at A is darkened in contrast.

## 2.5. Anodic Oxide Film in Low Vacuum Mode

Semiconductor devices are composed of a combination of fine semiconductors, conductors and insulators. The LV mode is one of the methods to reduce charge accumulation due to electron beam irradiation, allowing for observation of insulators by SEM.

**Fig. 9 Observation of a Defect on Gold Plating Using UED and SBED.**



(a) Stain-like defect (marked by an arrow) on gold plating observed by an optical microscope. (b) Defect observed by UED. Landing voltage 5 kV. The defect (marked by yellow arrows) has darker compositional contrast than the gold plating (area framed by a blue dotted line). (c) Defect observed by UED. Landing voltage 700 V. At low landing voltage, information on the surface was captured more clearly than at 5 kV, showing larger areas of dark compositional contrast (areas framed by yellow dotted lines). (d) Cross-sections processed by FIB at areas A, B, and C in (b) and (c) and observed by SBED. Landing voltage 3 kV. A layer indicated by dark compositional contrast was identified on top of the bright Au layer. Carbon, Cr, and W were deposited before cross-sectional fabrication with FIB for specimen surface protection. The topographic contrast representing the shape of a void in the Au layer in A was also confirmed. (e) Backscattered electron image and EDS element maps of the cross section at B. The backscattered electron image was obtained using the SBED and EDS elemental maps by a X-Max<sup>®</sup> Extreme (Oxford Instruments EDS). Landing voltage 4 kV, irradiation current 1 nA. Ni and O were detected from the layer with dark compositional contrast in the EDS elemental map.

**Figure 11** is a backscattered electron image of an aluminum anodic oxide film (alumite) observed in the LV mode. Alumite is an insulator with a fine porous structure formed on the surface. In the LV mode, which facilitates observation of insulators, the electron beam scatters through the interaction of the incident electron beam with the gas molecules in the specimen chamber unlike in a high vacuum. This increases the size of the incident electron beam, likely to compromise resolution. The JSM-IT800, however, successfully identified the porous structure 10 nm to 100 nm in size on the alumite surface in the LV mode utilizing its In-lens Schottky Plus field emission electron gun featuring high brightness and a small light source.

**Summary**

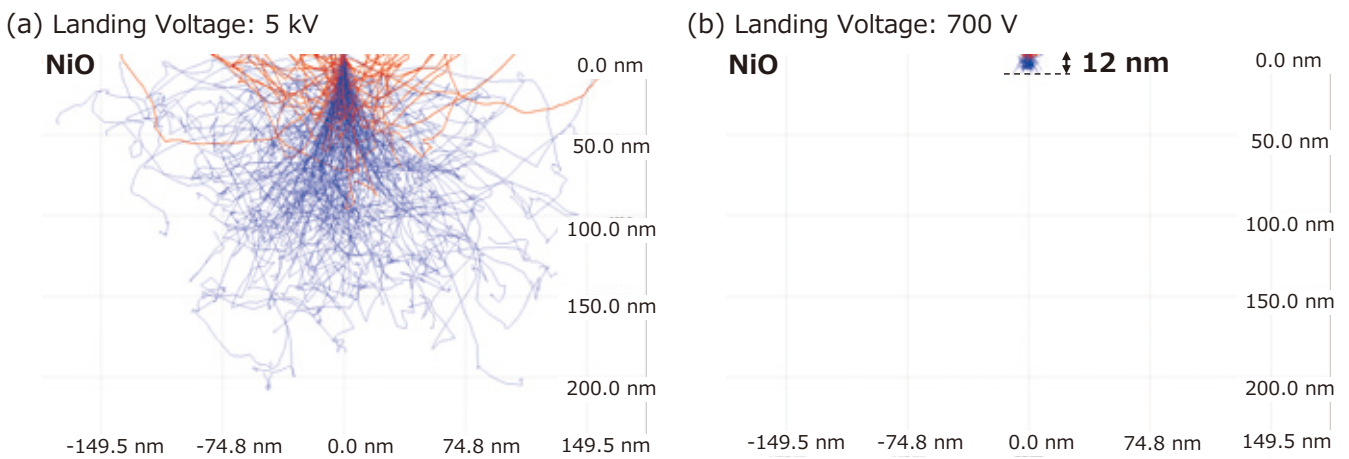
In this paper, we introduced the features of the new semi-in-lens SEM, JSM-IT800 and various images and analytical data acquired. The JSM-IT800 features a semi-in-lens objective lens with low aberrations for high-resolution imaging and a signal-selecting function for separating

electrons emitted from the specimen depending on the energy and angle. It is a powerful tool for semiconductor defect analysis, being capable of high resolution VC imaging to examine micro specimen shapes such as top and bottom surfaces, cross sections, and sides of inclined specimen, simultaneous acquisition of multiple signals, and imaging of insulator specimens without coating a specimen.

**References**

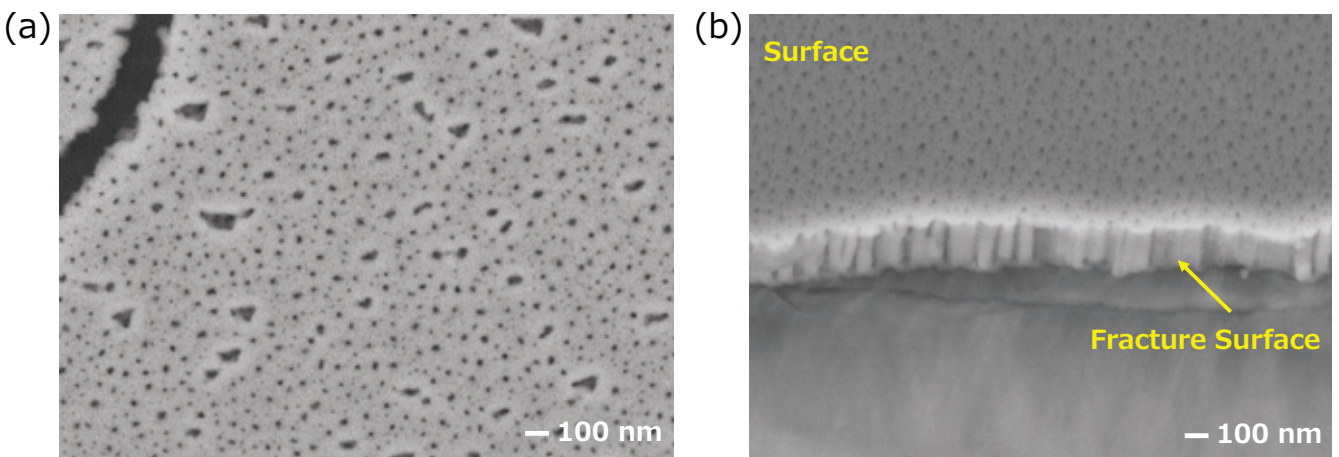
- [ 1 ] O. Suzuki, M. Inoue, Y. Yamaguchi, Various Analyses of Fine Structures using Multipurpose High Throughput Analytical FE-SEM: JSM-IT800, *JEOL News*, Vol.55, No.1, 49-55 (2020).
- [ 2 ] The New Detection System of High-End FE-SEM JSM-IT800 Super Hybrid Lens (SHL), *JEOL News*, Vol.56, No.1, 42-49 (2021).
- [ 3 ] Ruediger Rosenkranz, Failure localization with active and passive voltage contrast in FIB and SEM, *Journal of Materials Science: Materials in Electronics* (2011)22, 1523–1535.

**Fig. 10 Simulation of Penetration Depth of Incident Electrons in Specimen NiO bulk specimen.**



Simulation results of the incident electron penetration depth when the stain-like defect was assumed to consist of nickel oxide (NiO). CASINO v2.51 used for simulation. Blue line represents the trajectory of incident electrons and red line the trajectory of backscattered electrons within the specimen. (a) At a landing voltage of 5 kV, the maximum penetration depth of incident electrons was about 200 nm. (b) At a landing voltage of 700 V, the maximum penetration depth of incident electrons was about 12 nm.

**Fig. 11 Observation of Aluminum Anodic Oxide Film in LV Mode.**



The LV mode allows for observation of aluminum anodic oxide film, an insulator, by reducing charge accumulation. Landing voltage: 5 kV. (a) Surface observation. Backscattered electron image. Fine pores 10 to 100 nm in size were observed. (b) Fracture surface observation. Backscattered electron image.



# Automated TEM lamella Preparation with JIB-4700F

Yoshitaka Ishihara, Tomohiro Mihira  
EP Business Unit, JEOL Ltd.

JIB-4700F is a Multi-beam processing and observation system equipped with SEM (Scanning Electron Microscope) and FIB (Focused Ion Beam). The main applications of this system are to prepare cross-sectional samples by FIB, to prepare TEM (Transmission Electron Microscope) samples, and to observe and analyze FIB cross-section by SEM. Particularly, TEM sample preparation has been carried out manually by operators in the past, but in recent years, automation using various techniques has been developed, which has led to labor saving for operators. In this article, the functions of automated TEM sample preparation by FIB will be described.

## Introduction

FIB is an instrument which can scan a fine ion beam on a sample, and can specify a position by observing a sample at a high magnification, and can carry out precise processing. Due to its advantages, it is mainly used for preparing TEM and SEM samples.

In order to achieve the desired accuracy, the FIB processing must be proceeded by changing the acceleration voltage and the probe current step by step so as to reduce the sample damage caused by beam irradiation. Therefore, it is required to adjust the optical axis, focus, and beam position of the ion beam for each acceleration voltage and probe current prior to processing. Since the beam position moves with and without the specimen approaching the accessory equipment such as a gas nozzle for deposition and a manipulator probe for pickup, pre-adjustment of this movement is also necessary. In order to prepare TEM samples, it is necessary to process various samples into a thin film with a thickness of 100 nm or less, which requires a high degree of skill for the operator. Since it is necessary to change the processing conditions step by step in the process of thinning, the operator could not leave the instrument room, the work efficiency was very low.

We have developed an automated TEM lamella (thin film) preparation function “STEMPLING” with the aim of making samples without relying on operators' skills and automatically producing many samples with high throughput. This function makes it possible for anyone to quickly, stably and easily fabricate high-quality samples, thus improving the work efficiency with limited human resources.

## JIB-4700F FIB-SEM Multi-beam System

JIB-4700F is a FIB-SEM instrument on which the SEM and FIB optical columns are mounted (**Fig. 1**). SEM column is equipped with a Schottky-Field-Emission electron source that enables high-resolution observations at low acceleration voltages (resolution of 1.6 nm @ 1 kV). Combination of “In-

lens-Schottky” electron gun and “Aperture-angle-Control-Lens” (ACL) can maintain high resolution even at high currents, enabling high-speed observation and analysis. FIB column is equipped with a high-current Ga (gallium)-ion source of up to 90 nA, which covers from large-area high-speed processing to fine processing of specimens. Since SEM and FIB are combined into a single instrument, the internal structure of the specimen processed by FIB can be immediately observed by SEM, and in addition, the cross section during processing can also be observed by SEM in real time. It is also possible to sequentially acquire SEM images and EDS maps while slicing with FIB, and to reconstruct the data in three dimensions later.

JIB-4700F can be equipped with the gas injection system. When an ion beam is irradiated while an organic gas is injected on the specimen surface from this system, a protective film can be made in the beam irradiated region by a chemical reaction.

In-situ nanomanipulator (optional) allows easy and reliable pick-up of the fabricated TEM lamellas in the specimen chamber. By adding “STEMPLING” function, many TEM lamellas can be fabricated automatically.

## Conventional Manual TEM Lamella Preparation Workflow

The procedures from TEM lamella preparation by FIB to observation by TEM are shown below.

- A) Preparation of protective film (carbon film) (**Fig. 2**).  
In order to prevent unintentional damage caused by ion beam irradiation to the region to be prepared, a protective film is deposited by the ion beam induced deposition using a gas injection system. At the same time, creation of a marker for beam drift compensation is made. The marker is a square deposition film with three small holes drilled by the ion beam processing.
- B) Cutting out sample chunk (**Fig. 3**).  
Cut out a slightly larger block (chunk) of the sample, being careful not to lose the protective film. Slope-shaped processing is performed at the back and front sides of

the area to be left using a large current beam, and then rough-finishing processing is performed to adjust the shape of the sample piece using a small current beam. After completion, the specimen stage is tilted so that the side of the chunk is visible, and bottom cutting and side cutting operations are performed to cut off the sample pieces from the base material. At this time, leave a bridge part for connecting a portion of the chunk with the base material.

- C) Pickup chunk with nanomanipulator (**Fig. 4**).  
Move the manipulator to bring the tungsten probe into contact with the chunk, then perform ion beam deposition (tungsten film) on the contact point between the sample piece and the tungsten probe, and adhere them. Then, the bridge part is cut by FIB, and the manipulator is moved upward to pick up the sample piece.
- D) Fix chunk to the FIB grid (**Fig. 5**).  
Move the sample stage to bring the sample post section of the FIB grid into the FIB field of view. Move the manipulator to bring the picked sample piece into contact with the sample post, and adhere them together with the tungsten deposition. After bonding, separate the tungsten probe and sample pieces by FIB. Then move the manipulator to retract the tungsten probe to a safe position.
- E) Thinning of chunk to fabricate TEM lamella (**Fig. 6**).  
The chunk is thinned by repeatedly processing the front and back sides. In order to maintain the mechanical strength, it is thinned stepwise from the edge of the sample toward the center. TEM lamella is completed when the thickness of the specimen central portion becomes 100 nm or less.

After completion of thinning, the FIB-grid is detached from the FIB and it is attached to TEM specimen holder. Then TEM holder is transferred to TEM for TEM observation.

As described above, the procedure for preparing a TEM sample by FIB is very complicated because a single lamella is prepared by repeating several tens of FIB processing. Until now, the operator had to manually specify processing conditions such as location, shape, size, beam current, total dose, scanning method and scanning direction at each lamella fabrication site.

In addition, pre-adjustment such as optical axis adjustment, focus adjustment and beam position adjustment are important to perform FIB processing with high accuracy. When the beam position is shifted by changing the beam current or inserting the gas nozzle of deposition, the processed sample is broken. Therefore, careful adjustment is necessary so that the beam position is not shifted.

Manual TEM lamella fabrication required operators to fully understand these situations, which requires high-level skills. Furthermore, operators were unable to leave the instrument while the above numerous manual operations were finished. This work was highly inefficient. The automatic TEM lamella preparation system “STEMPLING” automates the workflow of A), B), and E) described above.

## Outline of STEMLING

The automatic TEM lamella preparation system “STEMPLING” is an optional attachment to the Multi-beam FIB-SEM system JIB-4700F and the Single-beam FIB system JIB-4000PLUS. The system was developed for allowing anyone to easily prepare TEM specimens without relying on their

skills, and allowing multiple samples to be prepared basically unmanned except for the insertion of sample holder to the instrument and the designation of lamella preparation positions.

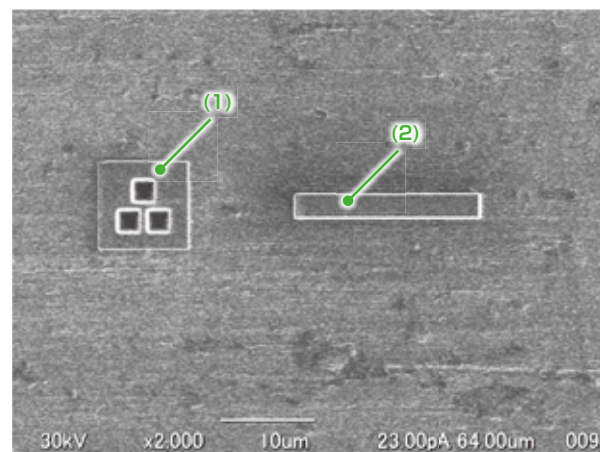
In STEMLING, it is possible to prepare various samples such as thicker samples (chunks) for pick-up (**Fig. 7 (a)**), thinned lamellas from chunks (**Fig. 7 (b)**), lamellas for picking up by a glass probe (**Fig. 7 (c)**), cross-sectional SEM observation sample (**Fig. 7 (d)**), pre-processing of the sample for three-dimensional SEM observation (**Fig. 7 (e)**). For TEM lamella fabrication, FIB processing with an acceleration voltage of 30 kV enables automatic processing up to 100 nm thick.

When using automatic sample preparation, it is important to keep the performance of the instrument above a certain level.

**Fig. 1 Appearance of JIB-4700F.**



**Fig. 2 Preparation of protective film and marker using deposition.**



(1) Drift Compensation Marker, (2) Protective film

STEMPLING is equipped with a function that automatically adjusts the probe current, adjusts the focus, and adjusts the beam position when changing the beam-conditions, which was previously done manually. Now these can be done automatically, the time and skills required for adjustment are no longer required.

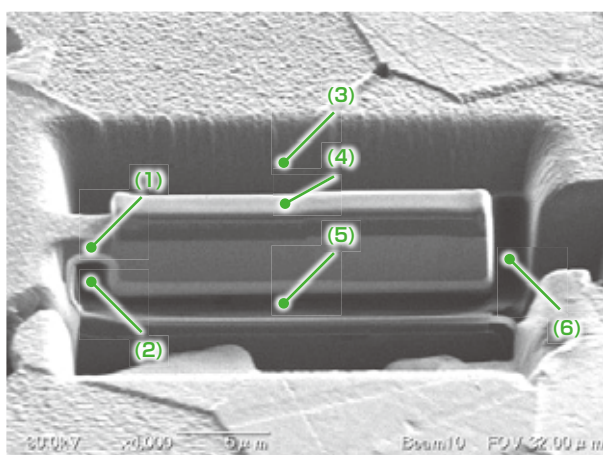
And, FIB beam stability is also important for long-time automated processing. In the past, only beam drift correction was performed but it was not sufficient. It is important to make the probe current and the focus more stable. In addition to that, maintaining the image brightness after switching the beam condition was also a problem in performing image processing. To solve these problems, we have newly developed and installed

the automatic probe current adjustment function (at the same time, the focus is also adjusted) and the automatic brightness correction function of the image using a new algorithm. As a result, stable FIB processing for a long time was possible. With STEMLING, a large number of samples could be prepared using multiple stage coordinates in a single operation.

### Sample preparation that does not depend on the user skills

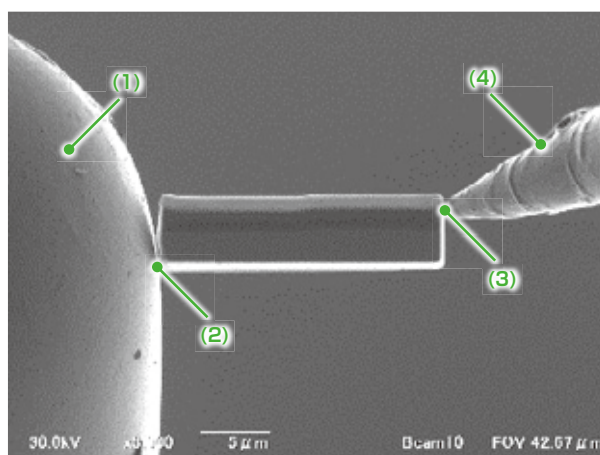
In STEMLING, the default recipes are prepared according to the sample shapes to be processed. Optimal processing parameters are automatically set simply by setting the sample size and

**Fig. 3 Cutting out a specimen block (chunk).**



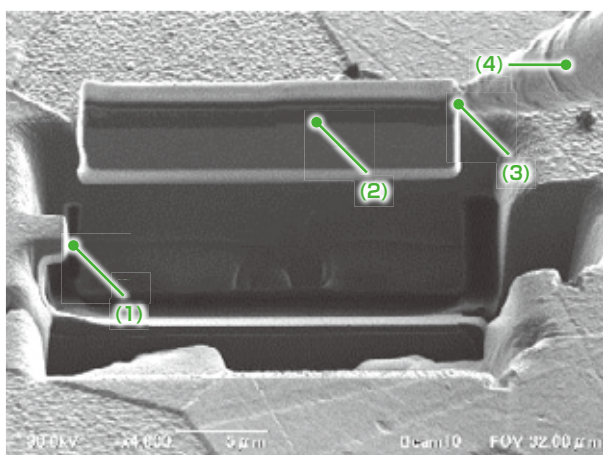
(1) Bridge part, (2)(6) Side cutting, (3) Slope processing area (The back and front sides of the sample block are processed into slopes.), (4) Cut-out block (Chunk), (5) Bottom cutting

**Fig. 5 Fixing a chunk to FIB-grid.**



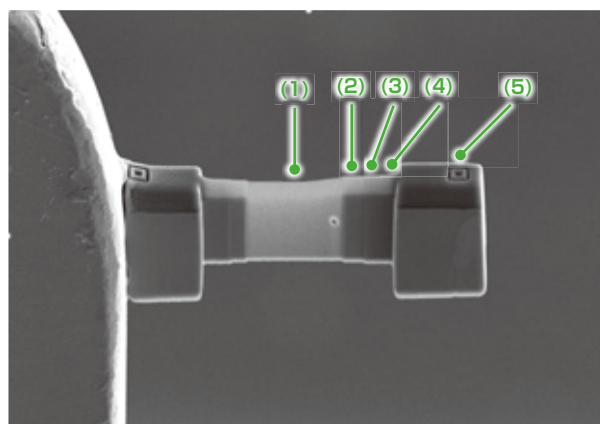
(1) Sample post section of FIB grid (TEM grid for FIB), (2) Adhere chunk and post by tungsten deposition. (3) After bonding to the post, cut off here by FIB. (4) Tungsten probe

**Fig. 4 Picking-up a chunk by nanomanipulator.**



(1) Bridge part disconnected by FIB, (2) Chunk, (3) Adhere probe and chunk by tungsten deposition. (4) Tungsten probe of nanomanipulator

**Fig. 6 Thinning of a chunk fixed to FIB grid.**



(1) Thinned section (100 nm thick), (2)(3)(4) To maintain strength, gradually reduce the thickness. (5) Drift compensation markers: Since beam drift compensation is especially important for automated processing, markers are drawn at the specimen edge by FIB and used to measure the amount of beam drift by image processing.



material type to be produced. As a result, a sample preparation function that does not depend on the user's skill has been realized.

**Figure 8** shows an example of sample preparation using a recipe of TEM lamella processing for some materials. TEM lamellas were processed on Silicon wafers, Copper plates and GaN-LED. 100-nm-thick TEM samples were successfully fabricated on all materials with ready-made recipes. If ready-made recipes cannot accommodate materials with extremely low etch rates or extremely heat-sensitive materials, the recipe sets can be customized (e.g., adjusting probe current and dose).

**Figure 9** shows TEM images of Magnesium alloy lamella prepared by STEMLING. (a) shows a transmission electron microscope image (TEM image), (b) shows a bright-field scanning transmission electron microscope image (BF-STEM image) and (c) displays a high-angle annular dark-field scanning transmission electron microscope image (HAADF-STEM image). In the figures (a) to (c), there are regions where the brightness differs in the lateral direction, because the thickness of the lamella is changed stepwise to maintain the strength as described in Fig. 6. The central part of the TEM sample was 4 μm wide, 7 μm high and was uniformly processed to about 100 nm thickness. It was not affected by the contamination due to redeposition after the FIB processing. Figure 9 (d) and (e) show the magnified HAADF-STEM images. The figure (e) is a further enlargement of the area indicated by the yellow circle in (d). The crystalline lattice of Mg was clearly observed in the specimen automatically prepared by STEMLING.

## Unmanned and multiple sample preparation

**Figure 10** shows an example in which 10 TEM lamellas were fabricated unmanned for about 8 hours. It can be seen that all of the lamellas can be prepared in the same shape, and it can be considered that stable automatic sample preparation has been performed. If the processing is set and started before the end of the day, it is possible to automatically prepare samples in the night.

**Fig. 8 Various TEM lamellas fabricated automatically using STEMLING.**

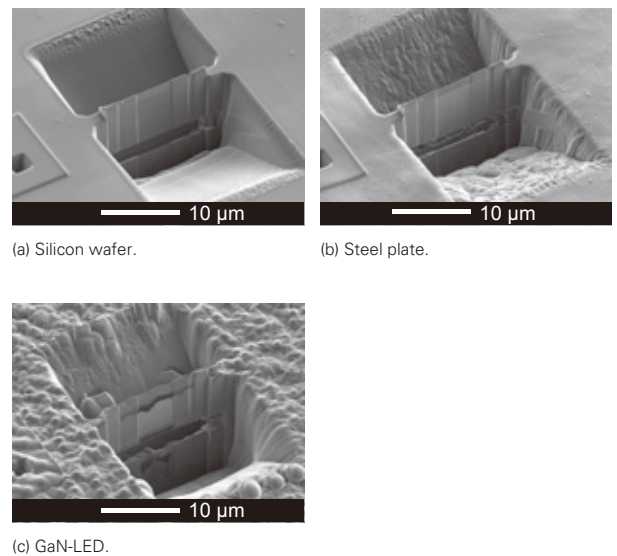


**Fig. 7 Types of sample shapes that can be made with STEMLING.**

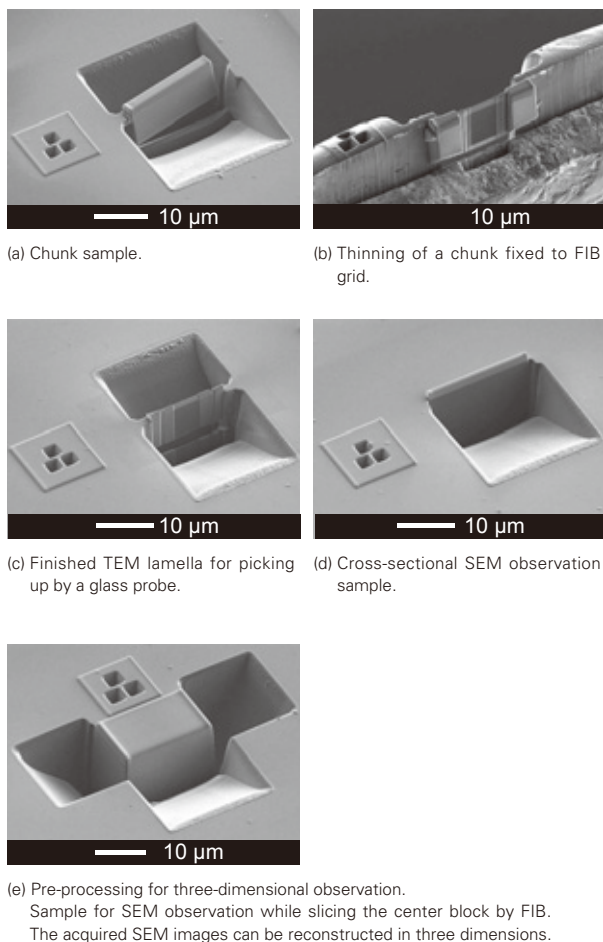
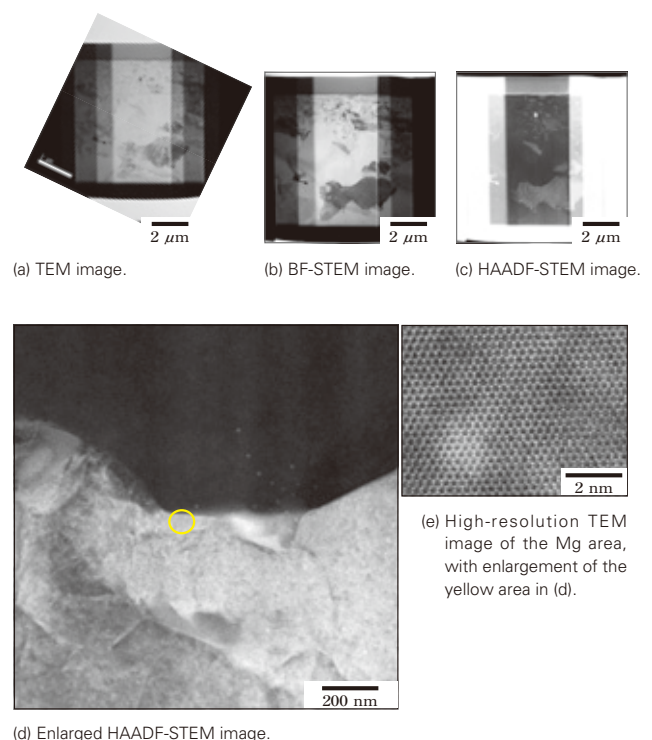


**Fig. 9 TEM observation images of Magnesium alloy.**

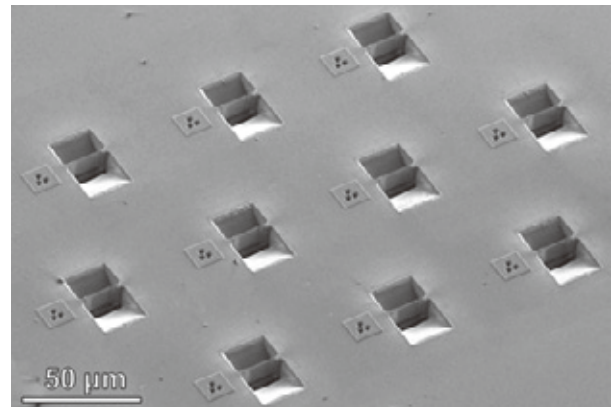


STEMPLING is capable of making multiple samples not only in one field of view but also in distant areas. When preparing samples at multiple locations, it is necessary to consider the height difference depending on the location. If there is a height difference, not only the problem of out-of-focus but also the problem of large misalignment arises when performing bottom cutting the chunk or lamella after tilting the stage. As the countermeasure, automatic tilt-eucentric adjustment function was implemented. Using this function, the height of the sample stage is automatically adjusted, and stable sample preparation become possible even for samples with steps. **Figure 11** shows TEM lamellas automatically prepared continuously on a piece of Silicon wafer and on a copper TEM grid with openings. A copper grid with a thickness of about 70  $\mu\text{m}$  was placed on a Silicon wafer piece. TEM lamellas were prepared cleanly without positional displacement even in the Silicon wafer section (a) below the step of the grid opening and on the copper grid above the step (b).

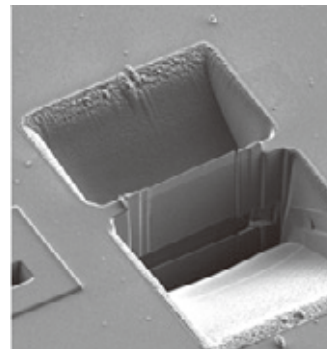
## Summary

An automated TEM sample preparation software system STEMLING has been developed as an optional attachment for JIB-4700F. This software automates the daily FIB adjustments such as probe current, focus, beam position shift when changing the beam condition. In addition, the processing settings have been simplified, making it possible to achieve diversified applications, such as preparation of samples of various shapes, processing various materials, processing in multiple locations and processing samples with steps. With STEMLING, anyone can easily prepare TEM samples without depending on operator skills. Furthermore, the time required for operators in front of the instrument can be greatly reduced. In a typical example, it took about 1 hour to process one TEM sample, but the operation time for the operator was about 10 minutes for preparation. Since it can operate automatically and stably, the efficiency of TEM sample preparation work is greatly improved.

**Fig. 10** Continuously and automatically prepared TEM lamellas (Sample: Silicon wafer).

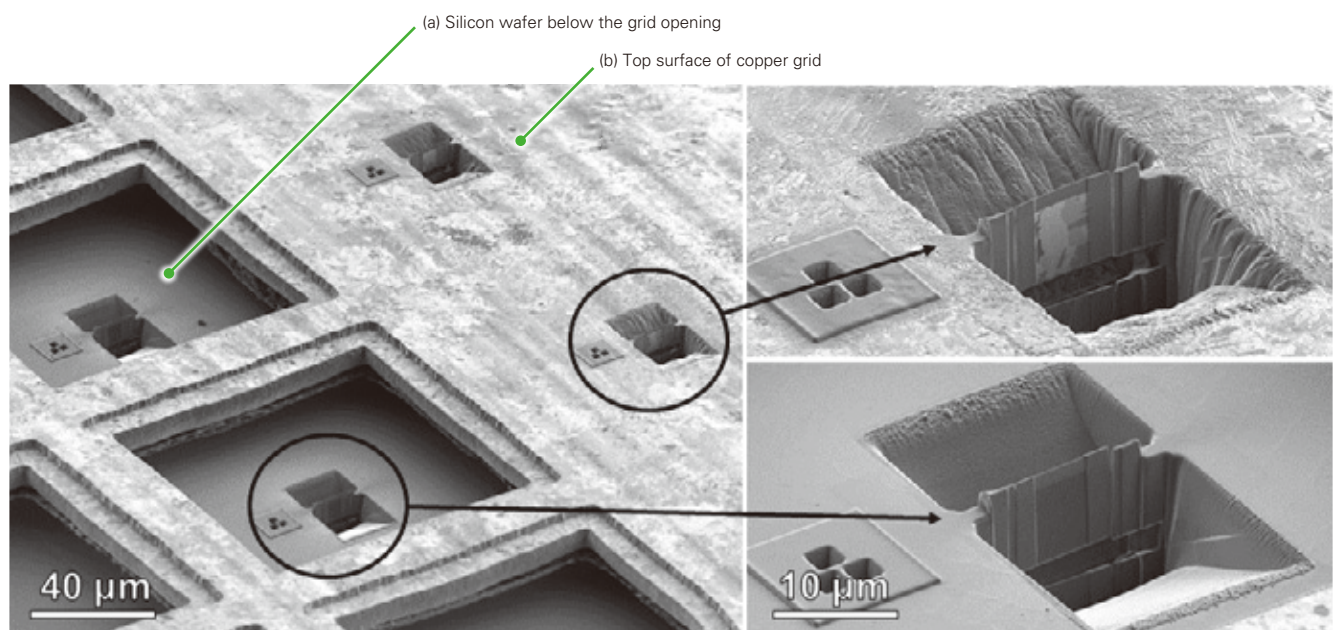


(a) 10 TEM lamellas fabricated in one operation (Processing time 8 hours).



(b) Magnified image of a lamella.

**Fig. 11** TEM lamellas automatically prepared from samples with step differences.



Specimen: Copper TEM sample grid on Silicon wafer piece

The upper right is a magnified image of TEM lamella made on the top surface of Copper grid.

The lower right is a magnified image of TEM lamella made on the Silicon wafer piece through the opening.

# Spectrum Imaging for Secondary Electrons and Backscattered Electrons Using Band Pass Filter with Variable Energy Resolution

Tatsuya Uchida<sup>1</sup>, Konomi Ikita<sup>1</sup>, Akihiro Tanaka<sup>1</sup>, Kazushiro Yokouchi<sup>1</sup>,  
Nobuyuki Ikeo<sup>1</sup>, Kenichi Tsutsumi<sup>1</sup>, Noboru Taguchi<sup>2</sup>

<sup>1</sup>JEOL Ltd. <sup>2</sup>National Institute of Advanced Industrial Science and Technology (AIST)

Scanning electron microscope (SEM) equipped with an electron analyzer makes it possible to perform both compositional analysis and chemical state analysis by utilizing analytical methods such as Auger electron spectroscopy (AES) and reflection electron energy-loss spectroscopy (reflection EELS, or REELS). As the electron analyzer selectively detects electrons with limited energy range at one time, it needs iterative detection with changing the analyzer condition in order to acquire electron spectra with an energy range of around 1000 eV or more. The wider the measurement energy range, the longer the measurement time. Therefore it is not a practical technique to acquire a spectrum image with an electron spectrum in each pixel of a secondary electron image because of tremendous acquisition time. However, we developed a new electron spectrum imaging method which enables us to enhance throughput while coping with sample drift. This paper introduces this method and some application cases.

## Introduction

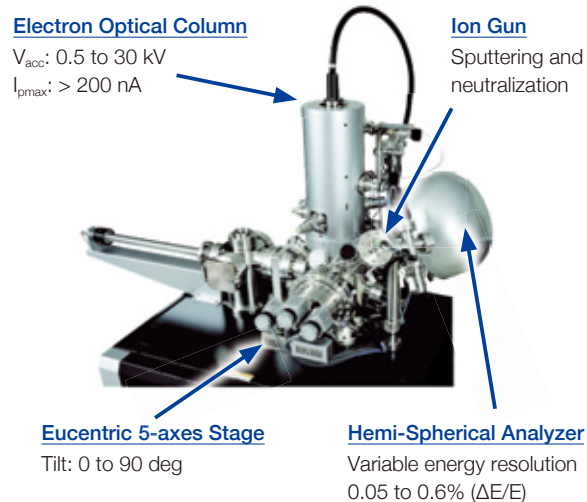
SEM can scan a focused electron beam and irradiate it on a sample surface to create images of secondary electrons (SEs) and backscattered electrons (BSEs) excited from the sample. The information is different among detected electrons. Secondary electrons mainly reflect surface morphology, while BSEs show topographic and compositional information. It is also possible to independently equip several detectors for multiple acquisitions at one time. When it comes to generic SEM, it is popular to use both a secondary electron detector and a backscattered electron detector for electron detection.

Electron spectrometers enable us to detect electrons exited from the sample with high energy resolution. Specifically, Hemi-Spherical Analyzer (HSA) can acquire electron spectra with optionally selective energy resolution for multiple purposes such as high energy resolution for chemical state analysis, standard energy resolution for elemental analysis and so on. Instruments for X-ray photoelectron spectroscopy are often equipped with HSA. SEM equipped with HSA is generally called scanning Auger electron microprobe (SAM) or AES. JEOL offers AES named JAMP-9500 series such as JAMP-9500F and JAMP-9510F (Fig. 1).

By the way, one of the most popular elemental analysis techniques in SEM is energy dispersive X-ray spectroscopy (EDS). Electron probe irradiation to the sample surface excites not only electrons but also X-rays so that elemental analysis

is possible by using energy differences of characteristic X-rays. Nowadays, area analysis in EDS acquires a data cube for spectrum imaging. After acquisition, operators can view the X-ray spectrum at any position in the measured area on

**Fig. 1 Auger microprobe JAMP-9510F.**





dedicated software. Data reconstruction of X-ray intensity mapping is also possible. These analytical schemes are user-friendly, which contributes to generalization of measurement method.

We believe that the functions mentioned above for EDS are also useful for AES. Moreover, we desire to evolve measurement technique unique to AES. These are the reasons why we developed spectrum imaging method derived from electron spectra using JAMP-9500 series. Now that newly developed techniques are applicable as options of JAMP-9500 series, we introduce the method with some application cases in this paper.

## 1. Working principle

### 1.1. Difference between EDS analyzer and electron analyzer

EDS analyzers detect X-rays, while electron analyzers detect electrons. When we focus on the detection depth under common analytical conditions, the detection depth of electrons is much shallower than that of X-rays. Therefore, analyses by electron analyzers are said to be surface sensitive and are easily affected by surface contamination.

In view of hardware controls, one of the differences between EDS and electron spectroscopy is parallel detection mechanism. X-rays coming to a detector for EDS are counted separately by the control circuit depending on X-ray energy. The detector has thousands channels so that wide energy range signals are simultaneously detected to get an X-ray spectrum at one time. On the other hand, analyses by electron analyzers need the energy sweep function which is described later.

**Figure 2** shows the diagram of the electron analyzer in JAMP-9500 series. SEs and BSEs emitted from a sample are decelerated in LENS system. Then, they are dispersed between hemispherical electrodes and finally reach an electron detector. Since the analyzer works as a band pass filter to electron energy, the electrons having certain kinetic energy are detected by the specific detector. Although the energy range detected at one time is limited, it is possible to designate both electron energy ( $E_0$ ) and electron energy resolution ( $\Delta E$ ) by controlling decelerating and dispersing conditions of the analyzer. The detector has fewer channels compared to that of the EDS analyzer. Therefore, the electron analyzer needs the energy sweep function which changes analyzer conditions between iterative electron detections to acquire an electron spectrum. Instead, we can execute data acquisition under optimal measurement conditions from elemental analysis condition to chemical state analysis condition because of variable energy resolution at electron spectrum acquisition (**Fig. 3**).

### 1.2. Spectrum imaging by electron analyzer

As for energy sweeps during electron spectrum acquisition, applied voltage of lens electrodes in the analyzer is shifted to change electron spectroscopic condition. This action needs settling time. The larger the time constant of the analyzer, the longer the settling time. We assumed the lens power source of the electrodes as a first-order linear time-invariant system and calculated the time constant of the system. **Figure 4** shows the step response at the hemispherical electrodes. The black line is a measurement result, and the red line is a calculation result. These results demonstrate that the time constant is around 17 msec. Incidentally, the settling time is automatically designated in JAMP-9500 series so that operators do not have to pay attention to the time constant or settling time.

As the measured energy points increase with the acquisition of the electron spectrum by the electron analyzer, we must wait for more settling time. Let's say that the settling time is 17 msec and the energy sweep executes 500 ch detections to acquire an electron spectrum. In this manner, the total waiting time approaches 8.5 sec because of 17 msec multiplied by 500 ch. If an area analysis like spectrum imaging acquiring spectra of all

**Fig. 2 Diagram of HSA.**

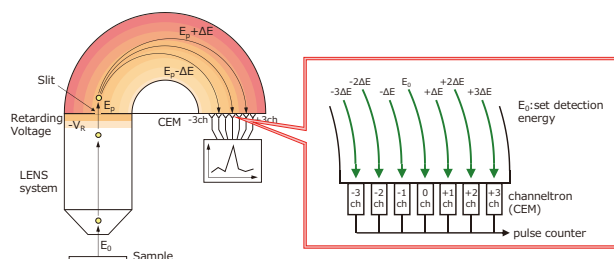


**Fig. 3 Electron spectra of Si with different energy resolution.**

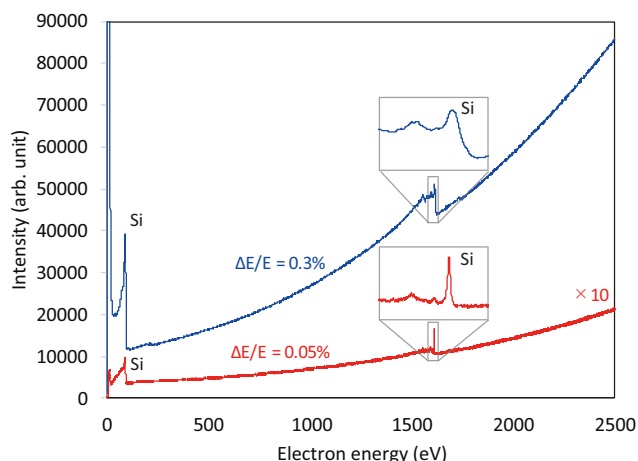
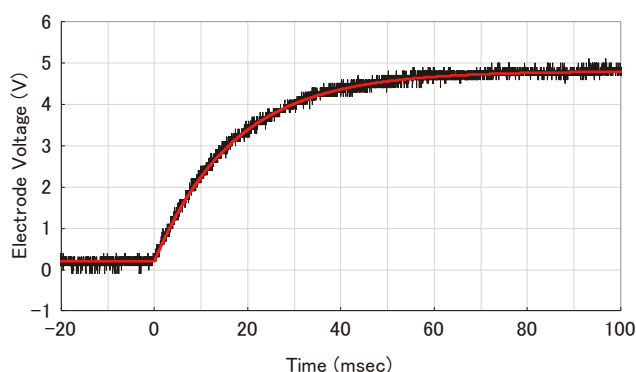


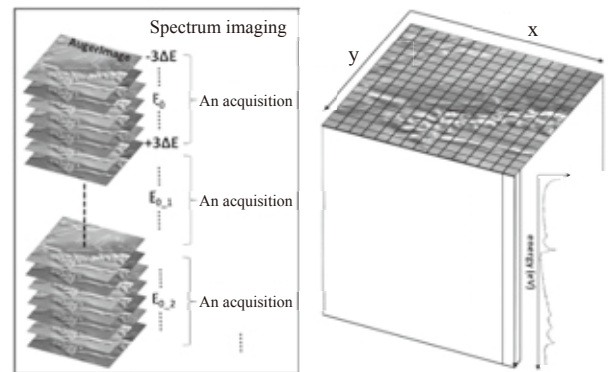
**Fig. 4 Transient response of lens power source.**



pixels obtains a data cube with 100 pixel × 100 pixel, the waiting time sums up to be 24 hours, which is 10000 times longer than that of an spectrum. So, reducing the number of the sweeps shortens the time of measurements in electron spectroscopy.

The sweep action mentioned above has hints to realize suitable acquisition method; that is, it is advantageous to firstly scan electron probe and get spectroscopic image under fixed analyzer condition and to secondly change analyzer condition for next spectroscopic images so as to suppress the number of the waiting for stabilization when we attempt to perform spectrum imaging by electron analyzers. **Figure 5** illustrates spectrum imaging scheme using iterative image acquisition. JAMP-9500 series can simultaneously detect 7 channel signals at one signal acquisition. This means measurement energy range is  $7 \times \Delta E$  which is the result of multiplication of an energy range at single channel ( $\Delta E$ ) by the number of channel (7). Therefore, it is best to shift the measurement energy by  $7 \times \Delta E$  between image acquisitions to minimize the number of waiting that occurs in spectrum imaging scheme. Each signal is detected by one of the 7 channels depending on electron energy.

**Fig. 5 Spectrum imaging with repetition of image acquisition.**



## 2. Electron spectroscopic spectrum imaging

### 2.1. Gain correction among detector channel

The spectrum imaging scheme treats 7 different signals from 7 channels as the different intensity of the spectra. In this case, intensity correction is necessary because of the sensitivity difference between detecting channels. **Figure 6** is an example of plotting a spectrum around 200 eV acquired by a 7-channel detector. The spectrum is acquired using the above scheme and each of the intensity is counted from one of the channels. The electron spectrum in Fig. 6 presents a pseudo-periodic artifact, the period of which corresponds precisely to the number of the detecting channels. This is because each channel has own detection sensitivity respectively. **Figure 7** indicates the sensitivity ratio among channels. The centered channel (0 ch) illustrated in Fig. 2 has higher sensitivity, and the channels positioned at the end has lower sensitivity.

If we know the sensitivity ratio between channels, we can correct sensitivity using the knowledge, thus canceling the pseudo-periodic artifact. However, the sensitivity varies as detecting electron energy changes. The irradiation position of the electron probe on the sample also affects the sensitivity. Unfortunately, there is not a good idea to measure additional data for grasping the channel sensitivity because it takes longer measurement time. Here we attempted to calculate the sensitivity ratio from the data cube acquired for spectrum imaging analysis.

Figure 6 denotes that intensity variation has strong periodicity but the degrees of variation is slightly influenced by the change of measurement energy. Therefore, we divided a spectrum into 7 spectra according to the detecting channels (**Fig. 8**). The intensity difference between these spectra represents the channel sensitivity, which can be used for sensitivity correction. During the correction process, we exclude the characteristic peaks as outliers from the spectra. Moreover, we applied smoothing to the spectra for reduction of statistical fluctuation.

**Figure 9** is the result of sensitivity correction between channels. The sensitivity correction effectively reduces the pseudo-periodic artifact [1].

### 2.2. Drift correction among images

Spectrum imaging by the electron analyzer repeats image acquisition the number of which depends on both measurement

**Fig. 6 Electron spectrum around 200 eV.**

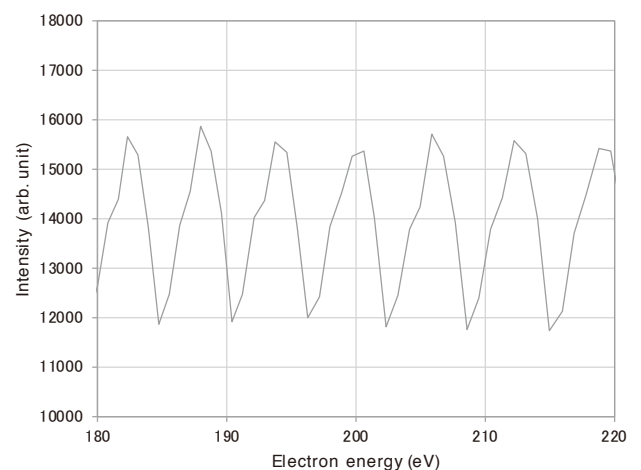
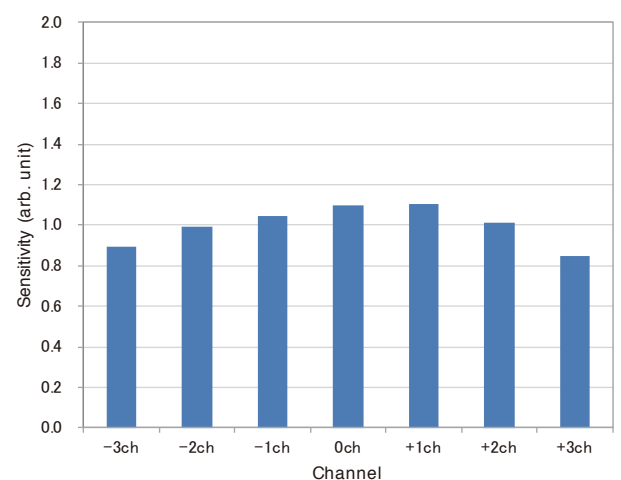


**Fig. 7 Sensitivity ratio between channels around 200 eV.**



energy range and measurement energy resolution. When a data cube is reconstructed from voluminous images, we need to pay attention to sample drift.

**Figure 10** shows a spectrum imaging result of the lead-free solder measurement. The left side of point 1 is a Cu-enriched phase, while the right side of point 1 is a Sn-enriched phase. The spectrum at point 1 drawn in Fig. 10 indicates that the intensity rapidly goes up and down as the energy changes. This phenomenon occurs every 7-measurement cycles because the field of view of the image drifts during iterative acquisition. The drift of analysis position affects spectrum intensity. We confirmed the drift by overlaying the electron spectroscopic images at 595 eV with the images at 615 eV because intensity variation is steep between 595 eV and 615 eV. **Figure 11** illustrates RGB synthesized image; the image at 595 eV is assigned to red, and the image at 615 eV is assigned to green. The contrast and brightness of the images are properly adjusted to clearly visualize the drift. The synthesized image indicates that the green image drifts about 1 pixel to the lower-left compared to the red image at point 1.

When we activate the probe tracking function to reveal the sample drift for electron probe position control during image acquisition at each measuring energy, we can compensate the drift just after the execution of the probe tracking function. If the drift changes over time, the amount of the drift is accumulated unless the probe tracking function is done again. It is important to minimize the influence of the sample drift at every pixel in the field of view for construction of data cube in spectrum imaging.

Aiming at minimizing the influence of the drift, we tried to correct the drift by not only the probe tracking function but also image data processing to the images. The data processing includes nonrigid image registration for local nonlinear distortion after applying translation and linear transformation (rotation, scaling and shear mapping). **Figure 12** shows the data processing result of the drift correction, which reveals that sample drift at every pixel is accurately removed. We applied this data processing to all images measured in spectrum imaging and reconstruct data cube. After the reconstruction, we checked the spectrum at point 1 in Fig. 10 (**Fig. 13**). Figure 13 proves that the intensity variation arising from the sample drift is reduced enough so that we can apply elemental analysis by characteristic electron peaks.

**Fig. 9 Electron spectrum before and after the sensitivity correction.**

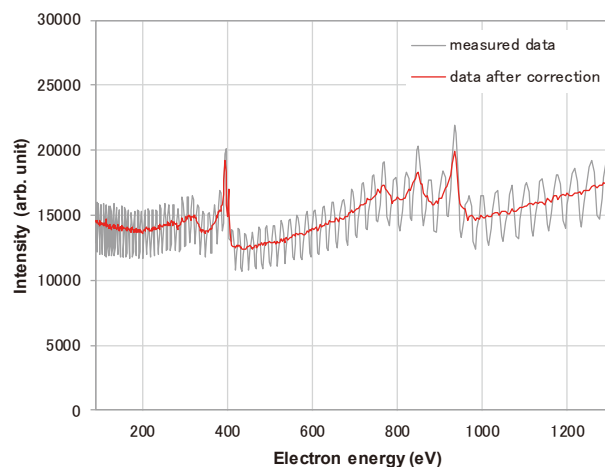


**Fig. 10 Electron spectrum around a boundary surface.**

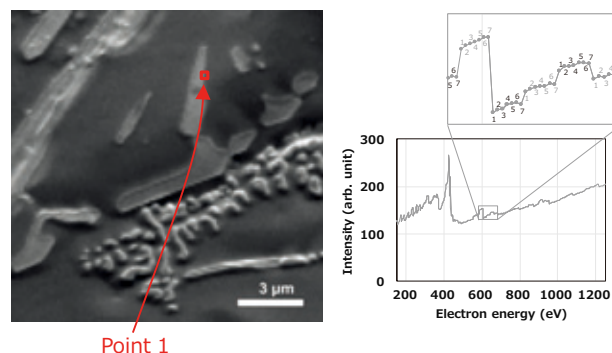


**Fig. 8 Electron spectra divided according to the detecting channels.**

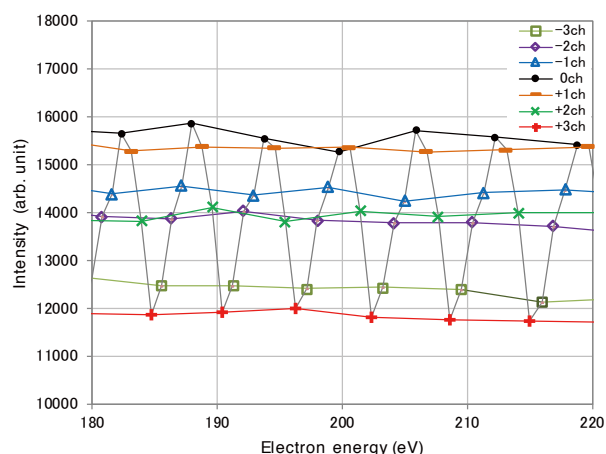
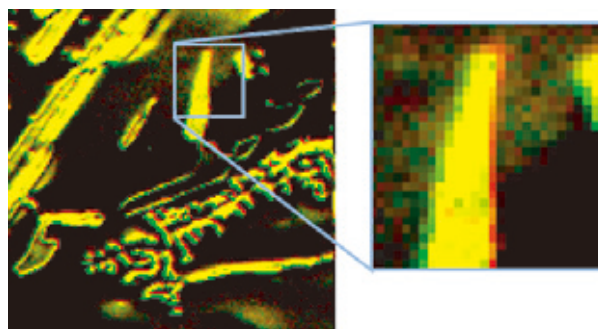


**Fig. 11 Drift visualization during iterative image acquisition.**





### 3. Application examples

Here, we will introduce measurement examples unique to electron spectroscopy.

#### 3.1. Measurement example using secondary electron spectroscopy

In ordinary secondary electron images and EDS analysis, information from different depths is obtained by changing the acceleration voltage. As shown in the schematic diagram in **Fig. 14**, the penetration depth of electron beam depends on the acceleration voltage of the incident electron beam. When the acceleration voltage is high, the information inside the sample is obtained. When acceleration voltage is low, the information near the sample surface is obtained. On the other hand, in the case of electron spectroscopy, it is possible to perform an analysis focused on the energy of electrons emitted from samples. **Figure 15** shows a graph called universal curve with the X-axis as electron energy and Y-axis as the mean free path. Estimating that the escape depth of electrons from the inside of the sample is about 3 times the mean free path, the escape depth of 50 eV electron is about 0.9 nm, and the that of 1000 eV electron is about 6 nm. In this way, since the escape depth depends on the kinetic energy of electrons, it is considered that information on different depths can be obtained using electron spectroscopy without changing the acceleration voltage.

**Fig. 12** Drift visualization after the image data processing.

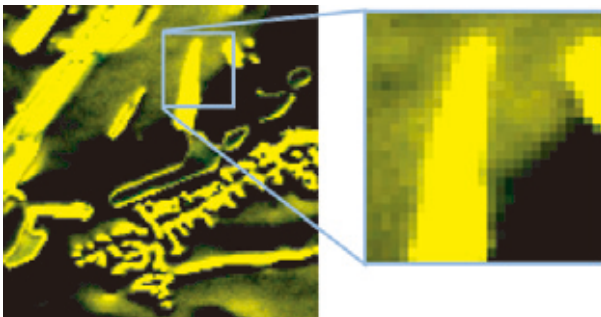
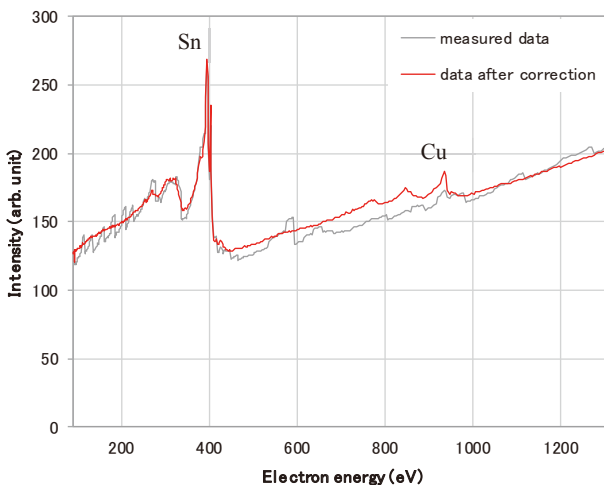


**Fig. 13** Elemental analysis of the spectrum after drift correction.



Therefore, we measured a test sample in which a TEM grid with supporting film was placed on the semiconductor pattern marked "20" as shown in **Fig. 16**. When the sample is observed with a normal secondary electron detector at an acceleration voltage of 30 kV, the character of the underlying pattern can be clearly observed. On the other hand, at 5 kV, the underlying character is not visible, and contaminations on the supporting film are observed with dark contrast (**Fig. 17**).

Next, **Figure 18** shows the results of observing the same sample by Spectrum Imaging at an acceleration voltage of 30

**Fig. 14** Schematic of electron beam diffusion.

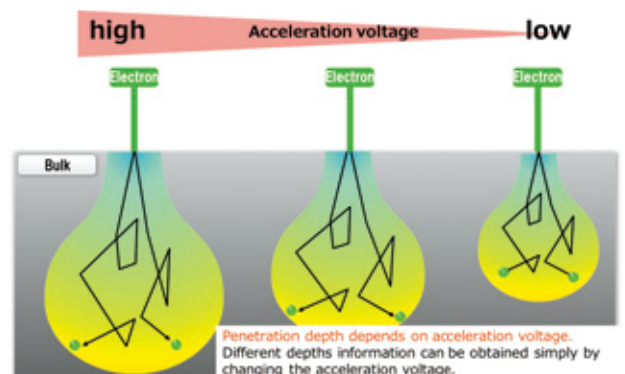


**Fig. 15** Relationship between electron energy and mean free path.

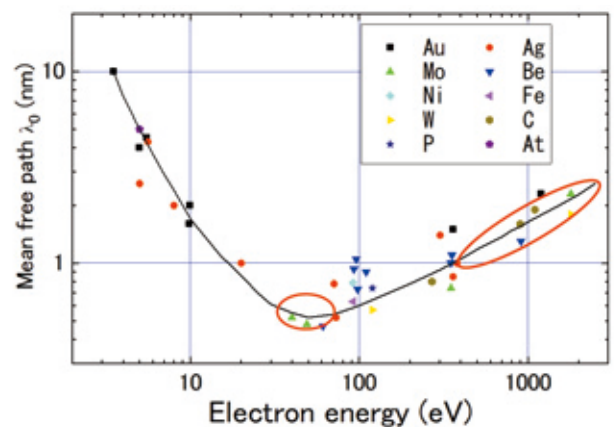
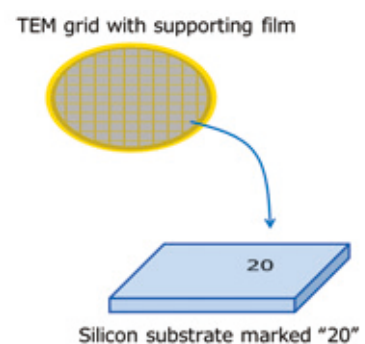


**Fig. 16** Schematic of the sample.



kV which has deep electron penetration depth. The measurement was performed with an irradiation current of 20 nA and an energy resolution of  $\Delta E/E = 0.5\%$ . Figure 18 (a) shows the average spectrum of the analysis area, where carbon, which is a component of the supporting film, is mainly detected. An electron spectroscopic image of any kinetic energy can be extracted from the data cube. Figure 18 (b) is an electron image taken in the energy range of 20 to 30 eV, and Fig. 18 (c) is that of around 2000 eV. Since the escape depth of electrons of 20 to 30 eV is shallow, an image in which the structure of the supporting film on the surface becomes prominent is obtained. However, since the excitation by backscattered electrons occurs, the underlying characters are also slightly observed. On the other hand, when electrons with higher energy of 2000 eV are selected, the components of the electrons that have escaped from the deeper side of the sample increase, the structure of the supporting film is no longer observed, and the information on the semiconductor pattern at the deeper part becomes prominent.

As described above, by using Spectrum Imaging using electron spectroscopy, it is possible to extract necessary information later. Even if a highly accelerated electron beam is used, a surface-sensitive image can be selected and acquired.

### 3.2. Measurement example using backscattered electrons

First, EELS using backscattered electrons will be described. In recent years, measurements using a transmission electron microscope have been actively performed, but in the case of AES, backscattered electrons are used to measure the amount of energy lost from incident electrons. It has been used for the battery material [2,3] and two-dimensional materials [4]. The energy of the dispersed electrons is expressed by equation (1).

$$E_{LOSS} = E_p - \Delta E \dots\dots\dots(1)$$

Here,  $E_{LOSS}$  is the energy of detected electron,  $E_p$  is the energy of the incident electron and  $\Delta E$  is the energy used for the transition. Since the energy used for electron transition differs depending on the electronic state and crystal structure of the sample, it is possible to obtain information that cannot be obtained by ordinary AES by performing EELS. This report focuses on the bandgap in the electronic state.

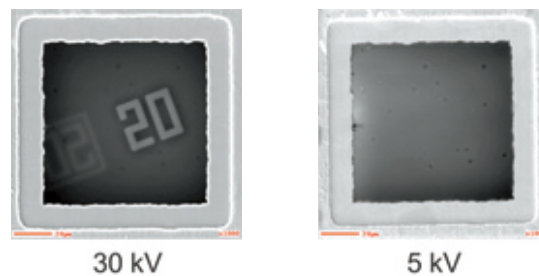
As shown in Fig. 19, the band gap corresponds to the energy difference from the upper end of valence band to the lower end of conduction band in semiconductors or insulators. Since a loss peak occurs when an electron in the valence band transitions to the conduction band by getting the energy of the incident electron, the minimum loss energy, that is, the first onset of the loss energy corresponds to the band gap.

For the sample, an antireflection film in which  $\text{SiO}_2$  and  $\text{TiO}_2$  were alternately formed on a glass substrate as shown in Fig. 20 was used. From the SEM image, each film thickness is around 100 to 200 nm.

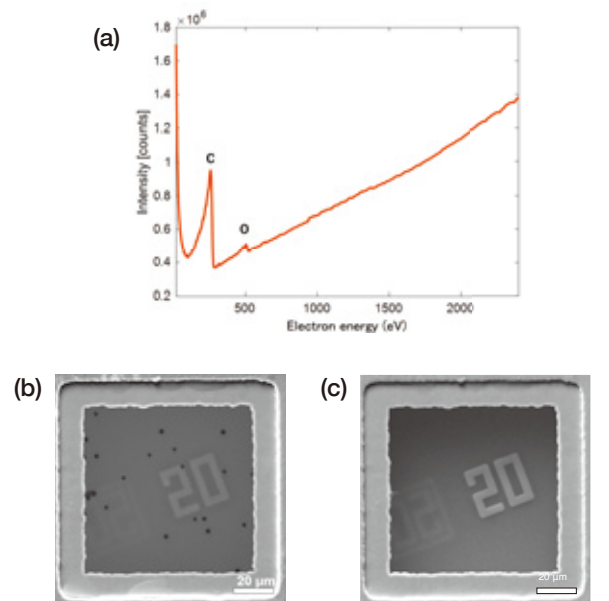
Figure 21 shows the loss spectra of  $\text{TiO}_2$  and  $\text{SiO}_2$  obtained from the reference sample. The acceleration voltage was 2 kV, the irradiation current was 10 nA, and the pass energy was 10 eV. The half width of the Gauss fit to the backscattered electron peaks were 0.86 eV and 0.80 eV for  $\text{SiO}_2$  and  $\text{TiO}_2$ , which roughly matches the energy width of the Schottky type electron gun. The band gaps were determined by curve fitting at the first onset of the loss peaks. For determination, Gaussian function is used and the half width is fixed to that of the backscattered electron peaks calculated above respectively. As a result, 5.0 eV and 9.3 eV for the  $\text{TiO}_2$  and  $\text{SiO}_2$  were estimated.

Figure 22 shows the measurement results of the IR filter sample using Spectrum Imaging. The acceleration voltage was 2

**Fig. 17 Secondary electron images of the sample.**



**Fig. 18**



(a) average spectra of the analysis area, and electron images of (b) 20 ~30 eV and (c) 2000 eV.

**Fig. 19 Schematic of how electrons occupy a band.**

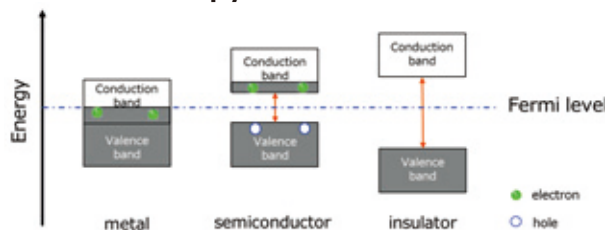
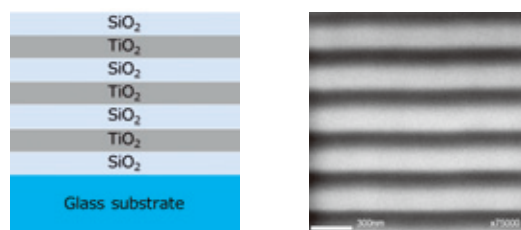


**Fig. 20 Schematic of the sample (left) and SEM image (right).**



kV that is the same as used in the previous spectrum. From the spectrum of Fig. 22(a) extracted from the Spectrum Imaging, there was a difference in the first onset position of the loss peak between SiO<sub>2</sub> layer and TiO<sub>2</sub> layer. Therefore, the results of visualizing the difference in bandgap by using this energy difference are shown in Fig. 22(b), (c) and (d). It can be seen that the SiO<sub>2</sub> layer and the TiO<sub>2</sub> layer are alternately formed.

**3.3. Measurement example with high energy resolution**

Here, an example of visualizing the difference in chemical and electronic states such as the shift of the Auger electron peak is shown. A pnp epitaxial planar transistor as shown in Fig. 23 was used as the measurement sample. In the electron spectroscopic spectrum using HSA, it has been known for a long time that energy value of the Auger electron peak differs between p-type semiconductors and the n-type semiconductors as shown in Fig. 24 [5, 6, 7, 8]. Since the energy difference in this case is within the band gap of the sample, it is often minute and requires analysis with high energy resolution.

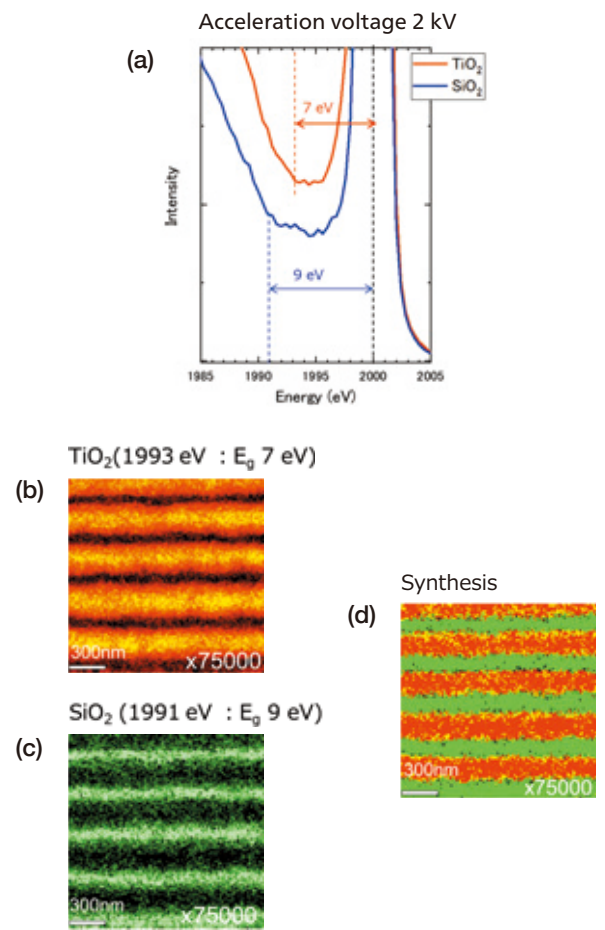
The reason why such energy difference occurs is explained using Fig. 25 and equation (2). Figure 25 schematically shows the relationship between Fermi level and work function of intrinsic, p-type and n-type semiconductors. The position of the Fermi level of the intrinsic semiconductor is located approximately in the center between the valence band and the conduction band, but in the p-type semiconductor, there are holes because the acceptors are doped, and the position of the Fermi level is lower than that of the intrinsic semiconductor. On the other hand, the case of n-type semiconductor, there are conduction electrons because the donors are doped, and the position of the Fermi level is higher than that of the intrinsic semiconductor. Since the position of the vacuum level does not change, the work function which is the energy difference from the Fermi level to the vacuum level, is larger in the p-type semiconductor and smaller in the n-type one.

Equation (2) shows the kinetic energy of Auger electrons. E<sub>x</sub> on the right side is the energy of the electron shell, and φ is the work function.

$$E_{KL_1L_{2,3}} = (E_K - E_{L_1}) - E_{L_{2,3}} - \phi \dots\dots\dots(2)$$

The energy of the electron shell is constant regardless of the dopant, but the work function differs depending on the dopant as explained above. Therefore, the peak position of the p-type semiconductor shifts to the high energy side, and that of the n-type one shifts to the low energy side. It is known that this shift amount depends on dopant concentration. In this way, it is also possible to

**Fig. 22**



(a) Spectrum extracted from the Spectrum Imaging data, and images revealing (b)TiO<sub>2</sub> layer, (c) SiO<sub>2</sub> layer, (d) synthesis image.

**Fig. 23 Schematic of the sample.**

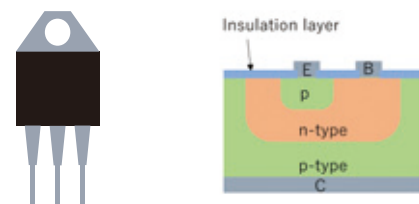


**Fig. 21 Zero loss peak of TiO<sub>2</sub> (left) and SiO<sub>2</sub> (right).**

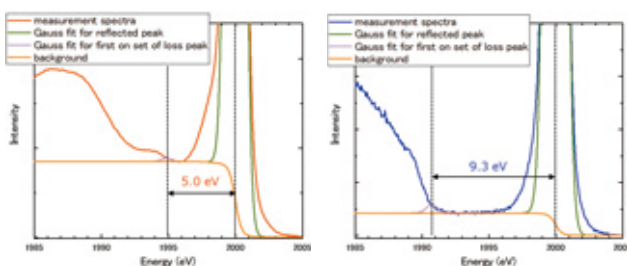
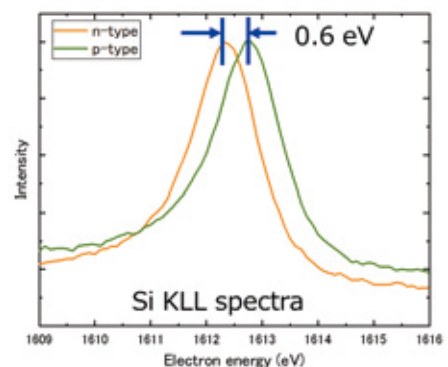


**Fig. 24 Si KLL spectra of p-type Si and n-type Si.**





know the electronic state of the sample using electron spectroscopy.

**Figure 26** shows the results of analyzing the Si KLL peak of a transistor sample using Spectrum Imaging. The measurement conditions were an acceleration voltage of 20 kV, an irradiation current of 30 nA, and a pass energy of 10 eV. The sample was prepared by mechanical polishing. And, as can be seen from the SEM image in Fig. 26 (b), the surface shape is slightly rough. In addition, ion etching was not performed during measurement, and an oxide layer of about 1 nm was formed on the sample surface. In the SEM image, the contrast is constant in the Si region except for the bonding area, and it is not possible to determine where the p-type or the n-type exists. However, as shown in Fig. 26 (c), it can be seen that the positions of Si KLL peaks are different in the spectra extracted from the regions surrounded by the orange and green squares. It is possible to extract the information to be known from the data processing by using Spectrum Imaging. Figure 26 (d) and (e) show the results of visualizing the surface distribution of p-type and n-type regions using the peak position difference. It can be confirmed that the n-type Si region is sandwiched between the p-type one. By using Spectrum Imaging with electron spectroscopy in this way, it is possible to visualize differences in work functions that cannot be discriminated by secondary or backscattered electron images.

## Conclusion

Spectrum Imaging of the electron spectrum has become possible at high speed due to the development of correcting the difference in the sensitivity of the channeltrons and the technology for correcting the sample drift. The newly developed Spectrum Imaging method is provided as optional software for JAMP-9500F and JAMP-9510F [9], and operations from Spectrum Imaging measurement to data analysis can be easily performed. As applications, this paper introduced examples such as separation of secondary electron images due to differences in escape depth of electrons, EELS measurement and visualization of the surface distribution due to differences in work function. We expect the techniques will facilitate further utilization as an Auger microprobe and as an SEM device equipped with an electron spectrometer.

## Acknowledgement

The content of this paper is the result of joint research with AIST. We would like to thank everyone involved in the development.

## References

- [ 1 ] N. Taguchi, T. Uchida, K. Ikita, A. Tanaka, N. Ikeo, K. Yokouchi, K. Tsutsumi: *Ultramicroscopy* **233** (2022) 113450.
- [ 2 ] N. Taguchi et al., ECASIA (2019).
- [ 3 ] N. Taguchi, H. Sakaebe, S. Tanaka: *Surf. Interface Anal.* **52** (2020) 335.
- [ 4 ] A. Tanaka et al., IPFA (2018).
- [ 5 ] R. Pantel, F. Arnaud D'Avitaya, Ph. Ged and D. Bois: *Scanning electron microscopy/1982/II* 548 SEM Inc., AMF O'hare(Chicago), IL 60666, USA.
- [ 6 ] D. V. Klyachko, S.A. Kozikov and V.G. Kriegl: *Surf. Interface Anal.* **18** (1992) 181.
- [ 7 ] W.S.M. Werner, H. Lakatha, H.E. Smith, L.LeTarte, V. Ambrose and J. Baker: *J. Vac. Sci. Technol.* **B16** (1998) 420.
- [ 8 ] M. Kudo, Y. Sakai, T. Ichinokawa: *J. Surf. Anal.* **7** (2000) 188.
- [ 9 ] [https://s3-ap-northeast-1.amazonaws.com/jeol/catalog/AP/spectrumimage\\_j\\_01.pdf](https://s3-ap-northeast-1.amazonaws.com/jeol/catalog/AP/spectrumimage_j_01.pdf)

**Fig. 25 Schematic of work function.**

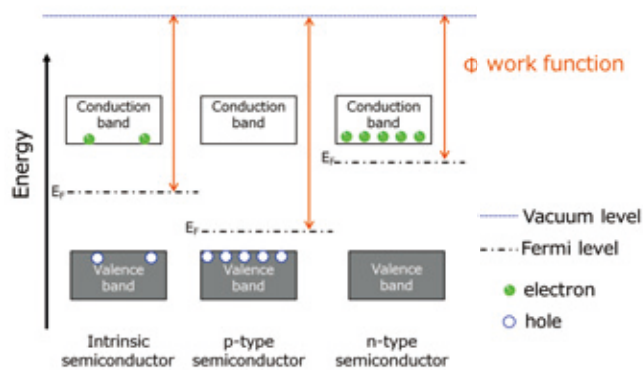
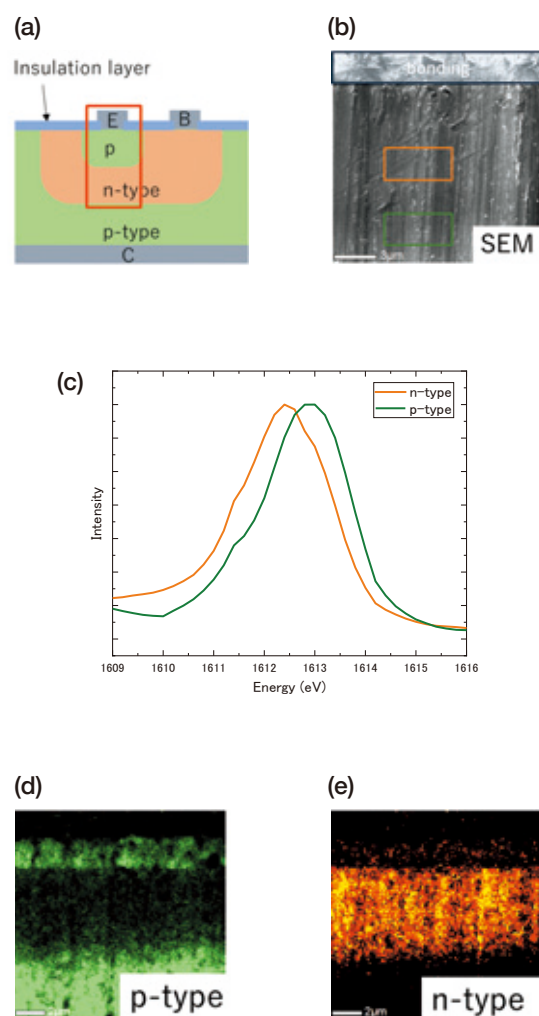


**Fig. 26**



(a) analysis area, (b) SEM image, (c) spectra extracted from orange and green squares in (b), (d) p-type Si distribution, (e) n-type Si distribution.

# Developing an Electron-Beam Metal 3D Printer JAM-5200EBM

Ayumu Miyakita 3D Additive Manufacturing Project, JEOL Ltd.

Additive manufacturing (3D printer) is expected as a manufacturing technique of the next generation. In March 2021, we began sales of "JAM-5200EBM" Powder-bed metal 3D printer using an electron beam as a heat source (3D-EBM), by utilizing the technologies we have cultivated in the development of electron microscopes and electron-beam lithography systems for semiconductor manufacturing. In addition to the high power, high speed scanning, and high vacuum inherent to the electron beam method, this equipment is characterized by long cathode life, beam correction, powder scattering prevention, and melting time control. In this paper, we will introduce the features and functions of the JAM-5200EBM, as well as some application examples of the 3D print.

## Introduction

3D printer is an instrument that converts a 3D model (CAD and other) into slice data, and then stacks these slice layers to create a 3D structure. For metal materials, there are some methods: the powder bed method, in which metal powders are laminated, and the deposition method, in which metal powders are melted while being directly sprayed. The melting of metal powders can be broadly classified into two types according to the difference in the heat source: laser beam and electron beam. Features of the electron beam method include: high power for high melting point materials, high throughput due to high scanning speed, reduced contamination due to forming under vacuum, and low strain due to the hot process.

We were responsible for the development of the electron beam powder-bed metal 3D printer (3D-EBM) at Technology Research Association for Future Additive Manufacturing (TRAFAM) for five years from 2014, and started to sell a 3D-EBM system JAM-5200EBM (Fig. 1), for industry in March 2021. JAM-5200EBM consists of a single crystal LaB<sub>6</sub> electron source mounted on an electron gun at the top of the electron beam column. The electron beam emitted from the source is controlled in diameter and

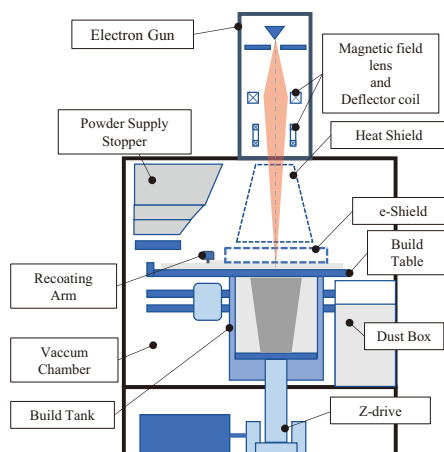
scanning range by the lower magnetic field lens and deflector coil. The maximum output of the electron gun is 60 kV - 6 kW, which enables fast metal melting. The vacuum chamber consists of a powder supply hopper that supplies metal powder, a recoating arm that pushes the metal powder dropped from the fixed quantity supply unit to the forming surface by comb teeth and smoothed it, a heat shield that keeps the temperature of the forming surface warm and prevents metal deposition to the surroundings, a Z-stage that raises and lowers the forming surface, and a build tank that stores the metal powder melted and temporarily sintered on the forming surface as the Z-drive unit descends.

## Features of JAM-5200EBM

### 1. Long life of the electron source

Since the 3D-EBM machine uses electron beams for both heating and melting processes, it is necessary to have an electron source that can output a high-power electron beam stably for a long time. The electron source of the JAM-5200EBM is a flat type LaB<sub>6</sub> electron source with a tip diameter of a few millimeters in order to achieve a maximum emission current of 100 mA. The electron source life of

**Fig. 1 Appearance, configuration and specifications of the electron beam metal 3D printer JAM-5200EBM.**



Manufacturing method	Powder bed fusion
Manufacturing dimensions	Maximum 250 mm (Dia.) × 400 mm (H)
Electron beam output	Maximum 6 kW
Lifetime of cathode	1,500 h or longer
Chamber pressure (during melting)	0.01 Pa or lower
Inert gas (for charging prevention)	Not required
Manufactured product cooling system	Equipped
Powder dispersal prevention system	e-Shield
Beam correction	Automatic (Focus, Astigmatism, Distortion)
Power supply	3-phase, 200 V (±10%), 35 kVA
Weight	4,900 kg

this machine is over 1,500 hours, compared to less than 1,000 hours for other products. The long lifetime is due to the optimization of the heating temperature of the electron source, the high vacuum of the electron gun chamber (Fig. 2) and the mitigation of the ion bombardment (Fig. 3).

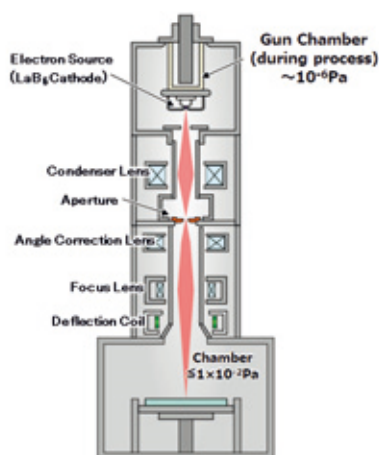
## 2. Beam correction function

When the electron beam emitted from the electron gun is scanned over a wide area in the modeling area, there will be a shift in the scanning position, as well as out-of-focus and astigmatism of the electron beam depending on the scanning position. For this reason, it is necessary to carry out a correction process according to the scanning position in order to achieve a high degree of accuracy. JAM-5200EBM has a correction function to measure the beam directly (Fig. 4).

## 3. Helium-free and powder dispersal prevention "e-Shield".

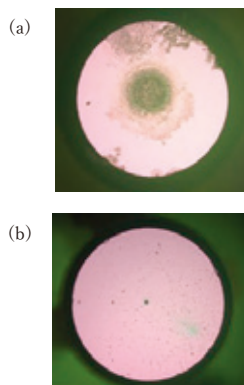
Powder scattering (so-called "Smoke") is caused by electrically isolated powder charges on the powder bed [1]. One method of controlling this is to introduce a small amount of helium gas, which is ionized by the electrons and then neutralized by the ions, but the

**Fig. 2 Electron optics system and differential pumping.**



An aperture between the electron gun chamber and the vacuum chamber allows the differential pumping of gases generated during the forming process to be blocked and the vacuum in the electron gun chamber to be maintained at  $10^{-6}$  Pa.

**Fig. 3 LaB<sub>6</sub> surface state after use.**



(a) without ion reflector (used for 60 hours) (b) with ion reflector (used for 1,500 hours). The instrument is equipped with a mechanism to suppress the penetration of positive ions into the electron gun in order to reduce ion impact.

introduction of gas causes significant degradation of the cathode electron source. We have developed a new powder scattering prevention mechanism called "e-Shield" (Fig. 5) to suppress this charge and prevent powder scattering in the unsintered area, thus achieving helium-free operation.

## 4. Melting time control

The melting of the surface in the additive manufacturing process is done by drawing melting lines at regular intervals and filling the specified area. In the case of melting short line with high-current and high-speed scanning, such as 3D-EBM, the next melting line is made before the first line has solidified, resulting in a disturbed melting surface and defects. JAM-5200EBM is equipped with a function to control the melt-solidification time for long and short melt lines.

## Modeling examples of 3D-EBM

### 1. Titanium alloy

Titanium alloys are light, strong and rust resistant, but have a high melting point and require high power for melting. Since 3D-EBM uses an electron beam as its energy source, it can melt at high power and is applicable to titanium alloys. An example of a prototype made with this machine is the electron gun chamber part made of titanium alloy (Fig. 6).

The tensile strengths of the Ti-6Al-4V alloys produced by the machine all meet the ASTM F136 standard and are equal to or better than the bulk material (Fig. 7). In addition, the metallurgical structure of the bulk material is a rather coarse equiaxial  $\alpha+\beta$  mixture, whereas the modeling material has a fine needle-like structure. The melting process in this machine involves the repeated formation and solidification of a local melt-pool by electron beam irradiation. This gives a different metallurgical structure than that of the bulk material (Fig. 8).

**Fig. 4 Auto-adjustment to measure the direct electron beam.**

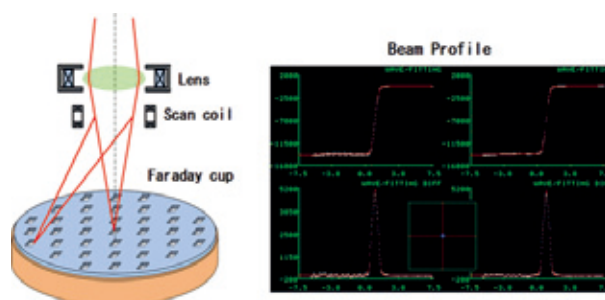


**Fig. 5 Powder dispersal prevention "e-Shield".**



The e-Shield prevents the charging caused by scattered electrons and allows stable building to continue without large-scale smoke.



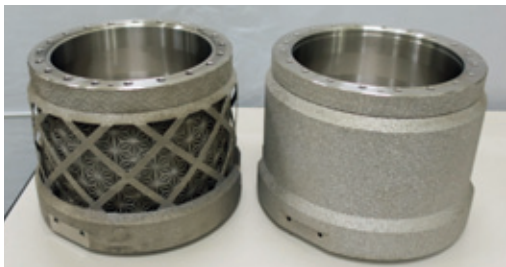
## 2. Pure copper

Pure copper must be manufactured in a more heat-retaining environment to ensure that its high thermal conductivity is not compromised. 3D-EBM can be used to melt materials in a high vacuum without compromising performance. As an example, a heat sink is shown in Fig. 9.

## 3. Nickel-based superalloys

Many nickel-based superalloys are difficult materials to cut and process. In addition, Ni-based superalloys, which require age-hardening treatment, do not provide sufficient creep property when layered in the cold process. By using 3D-EBM, it has been reported that high creep property can be obtained in the as-built [2]. As an example, the turbine-blade is shown in Fig. 10.

**Fig. 6 Prototype of a Ti-6Al-4V practical component.**



Electron gun chamber (height 173 mm / secondary machining) Lightweight (left), conventional (right). The building object is around 25% lighter by weight than before.

**Fig. 7 Results of tensile tests on Ti-6Al-4V alloy 3D-EBM objects.**

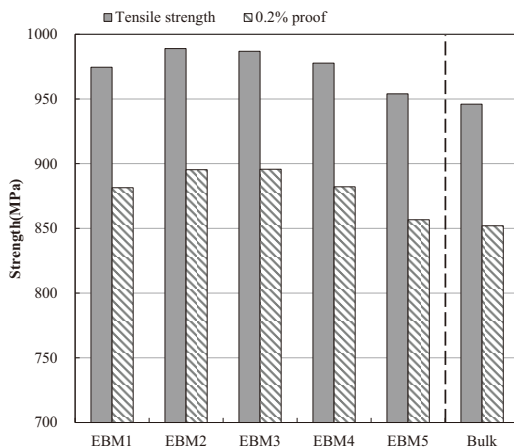
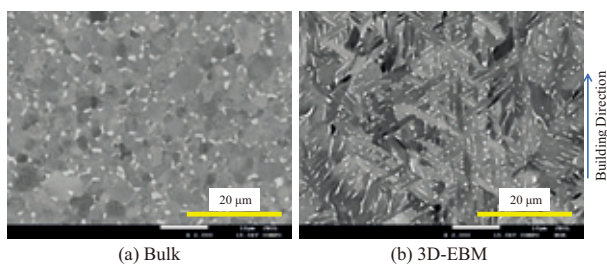


**Fig. 8 Observation of the metallurgical structure of Ti-6Al-4V alloy objects.**



## Conclusion

JAM-5200EBM uses the electron beam control technology that we have developed over the years to enable high quality, highly repeatable forming. This machine enables the integration of multiple components, weight reduction to reduce fuel consumption and increase power output, reduce costs and shorten development time. In the future, we plan to further improve the stability of operation and throughput, as well as develop the machine so that it can be used as a safe and reliable instrument for a wide range of customers, including the modeling of materials that can demonstrate the effectiveness of the electron beam method.

## Acknowledgments

The development of this technology was supported by the “Technology Research Association for Future Additive Manufacturing” commissioned by the Ministry of Economy, Trade and Industry (METI) from 2014 to 2016, and the “Development and Commercialization of Modeling Technology for Next-Generation Industrial 3D Printers” commissioned by NEDO from 2017 to 2018.

## References

- [ 1 ] M. Sigl, S. Lutzmann, M. F. Zäh: Transient Physical Effects in Electron Beam Sintering, in ‘Solid Freeform Fabrication Symposium Proceedings 17, Austin, TX, 2006, pp. 397-405.
- [ 2 ] A. Kamigaichi, K. Kakei: Microstructure and creep properties of Inconel 718 fabricated by electron beam additive manufacturing, Tokyo Metropolitan University, 2019.1.10.

**Fig. 9 Prototype Pure Copper Components: Heat Sinks.**



It is made of pure copper and is capable of forming complex, hollow shapes.

**Fig. 10 Prototype nickel-based superalloy (718) component: turbine blade.**



It is also possible to form nickel-based superalloys, which require preheating to temperatures of 1100 °C or higher.

# Gas Chromatograph - Quadrupole Mass Spectrometer, JMS-Q1600GC UltraQuad™ SQ-Zeta

Yoshio Abe and Masaaki Ubukata MS Business Unit, JEOL Ltd.

The new JEOL “JMS-Q1600GC UltraQuad™ SQ-Zeta” is a 6<sup>th</sup> generation high-performance GC-QMS that can be used for a variety of applications involving both qualitative and quantitative analysis. Additionally, the basic high-performance capabilities offered by this system have been further improved with the addition of the “EPIS” ion source and “msFineAnalysis iQ” software. The high-performance “EPIS” ion source is a high sensitivity EI source that was specifically designed to lower the detection limits of the system for improved quantitative analysis, and the “msFineAnalysis iQ” software is designed to improve qualitative analysis results by combining GC-EI and GC-Soft Ionization data to automatically generate an integrated qualitative analysis report.

## Introduction

We are pleased to announce the release of the new “JMS-Q1600GC UltraQuad™ SQ-Zeta”, a 6<sup>th</sup> generation JEOL gas chromatography-quadrupole mass spectrometer (GC-QMS) that further builds upon the 1<sup>st</sup> generation “JMS-K9” launched in 2003. The appearance and features of each successive JEOL GC-QMS are shown in **Fig. 1**. The JMS-Q1600GC has the highest sensitivity commercially available within the GC-QMS market and provides a wide dynamic range that makes it suitable for both qualitative and quantitative analysis for a wide variety of applications and samples. As for the software, MSPRIMO™ provides an intuitive user-interface for instrument operation, and Escribe™ provides an optimized user-interface for multi-component and multi-specimen quantitative analysis. In addition, the JMS-Q1600GC can be equipped with an optional high-performance ion source “EPIS” to enable highly sensitive electron ionization (EI) measurements and optional “msFineAnalysis iQ” software to enable automatic qualitative analysis of GC-QMS data using many of the same features implemented in our highly successful “msFineAnalysis” software that was originally designed for gas chromatography-high resolution time-of-flight mass spectrometry (GC-HRTOFMS) data. In this article, we will be discussing the new JMS-Q1600GC with a specific focus on these new options.

## High-Performance Ion Source “EPIS”

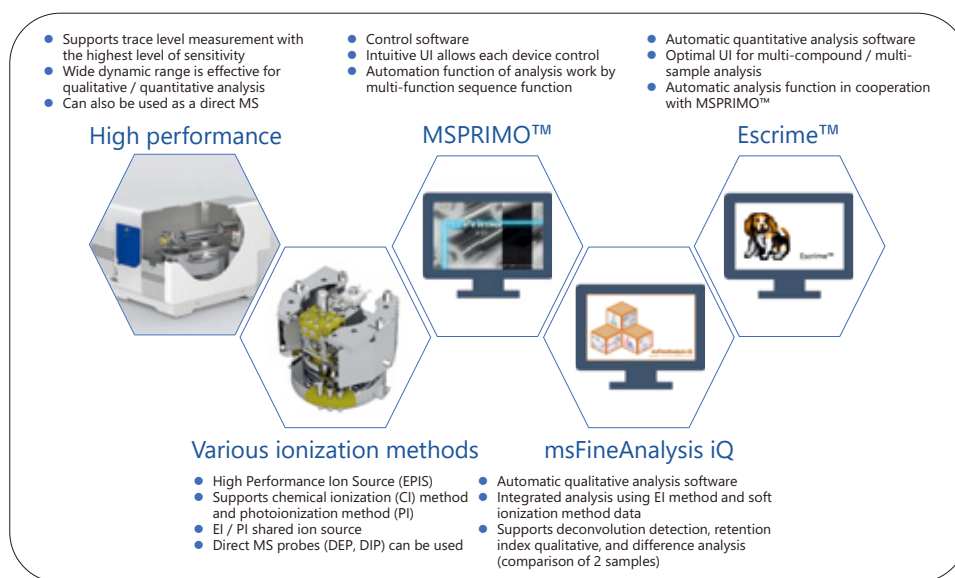
The “Enhanced Performance Ion Source” (EPIS) is an optional EI ion source that enables highly sensitive GC-EI measurements due to improvements to the design of the ion source chamber (**Fig. 2**). The instrument detection limit (IDL) when using the EPIS for octafluoronaphthalene (OFN), which is commonly used for GC-MS sensitivity measurements, is 1 fg or less. This is more than a five-fold improvement in sensitivity when compared with the IDL using the standard EI ion source which has an IDL value of 5 fg. **Figure 3** shows the selected ion monitoring (SIM) chromatograms for 8 consecutive 5 fg OFN measurements in which the IDL calculated from the peak areas is 0.6 fg.

Therefore, despite the fact that the JMS-Q1600GC is capable of high-sensitivity GC-MS measurements with the standard EI ion source, the EPIS can provide even higher sensitivity results when used on the system.

## Japan Water Quality Standards Testing Using Scan Measurement Mode and Dual GC Column Configuration in a Single GC-MS System

In this work, we used a JMS-Q1600GC equipped with an EPIS to do a study showing that this GC-MS system can measure all chemical compounds required for Japanese water quality standards testing. These standards are specified in Japan by the “Ministerial Ordinance on Water Quality Standards” based on Article 4 of the Waterworks Law and requires that 19 chemical compounds must be tested by using GC-MS. Additionally, these 19 chemical compounds are classified into five sub-groups that include volatile organic compounds (VOCs), mold odor-causing substances (mold odors), haloacetic acids, formaldehyde, and phenols. To further complicate this situation, the VOCs and mold odor compounds require a mid-polarity GC column while the haloacetic acids, formaldehyde, and phenols require a nonpolar GC column (see **Fig. 4**). As a result, when measuring all of these compounds, it is normally necessary to exchange the GC columns when using a single GC-MS system. Also, when two GC columns are simultaneously connected to an MS (even if only one column is used), the Helium carrier gas must be supplied to both columns which then reduces both the MS vacuum level as well as the sensitivity of the system. However, the JMS-Q1600GC equipped with an EPIS can maintain the required sensitivity for all analytes while being simultaneously connected to a medium polar column (VOCs and mold odor) and a non-polar column (haloacetic acids, formaldehyde, and phenols). Furthermore, the sensitivity of the EPIS is such that Scan measurements can be used for these protocols instead of SIM measurements, thus improving the work efficiency of the GC-MS measurement for water quality testing. SIM quantitation measurements start with a Scan measurement of the standard sample to determine the best ions for monitoring the analytes. Afterwards, a SIM method is setup to monitor each ion of interest, and then the

**Fig. 1 Photos and features for all JEOL GC-QMS models, including the new JMS-Q1600GC.**



standard samples are measured for a calibration curve followed by measuring the real samples for quantitative analysis. In contrast, Scan quantitation greatly simplifies the analysis when compared to SIM quantitation in that it eliminates the SIM setup step and allows the analyst to directly measure the standard samples and the real samples by using Scan mode. Typically, Scan measurements provide poorer sensitivity measurements when compared to SIM measurements so it is typically not possible to do high sensitivity testing of low-level analytes. However, the JMS-Q1600GC equipped with an EPIS improves the Scan mode sensitivity to a sufficient level for testing protocols that previously required SIM methods. For this work, all compound peaks were detected with enough intensity, indicating that the Scan sensitivity was enough for water quality testing. **Figure 5** shows the extracted chromatograms for 1,4-Dioxane, 2-Methylisoborneol, chloroacetic acid, and 2,4,6-Trichlorophenol which are generally difficult to measure with high sensitivity.

In addition to the low-level detection of the target compounds, the Japanese Water Quality Standards protocol also requires that the GC-MS must be capable of measuring concentrations of 1/10 or less of the action limit for each target compound with a coefficient of variation of 20% or less. In this study, we were also able to confirm that the coefficient of variation was below 20% for all 19 compounds tested at the required concentrations below the lower limit, and the results are shown in **Table 1**. Since the coefficient of variation for all compounds was less than 20%, it can be concluded that the JMS-Q1600GC with EPIS and two GC column configuration in this study

**Fig. 2 Image of high-performance ion source "EPIS".**



can be applied to the measurement of water quality standards using the simpler Scan mode method.

**“msFineAnalysis iQ” – Integrated Qualitative Analysis Software**

“msFineAnalysis” was first released in 2018 as an integrated qualitative analysis software package that combines the analysis results of EI and Soft Ionization (SI) methods measured by gas chromatography-high resolution time-of-flight mass spectrometry



(GC-HRTOFMS) to automatically generate a qualitative analysis report. This software was specifically written for high resolution data analysis and has steadily improved with each successive version of the software. With the release of “msFineAnalysis iQ”, this highly acclaimed software has now been expanded to the qualitative analysis of low-resolution data from a GC-QMS (JMS-Q1600GC).

Typically, qualitative analysis by GC-QMS only involves library database (DB) searches using EI data. However, if qualitative analysis is performed using only the similarity score to the library spectrum, it is not uncommon to have multiple candidates with high scores for some unknowns which can then result in the wrong candidate being selected by the analyst. Alternatively, if the sample has also been measured using soft ionization (SI), then it is possible to narrow down the DB searches by using the molecular ion information for each analyte. However, this adds another data set for the analyst to work with, further complicating the overall analysis. msFineAnalysis iQ addresses this situation by automatically combining the EI DB search results with the molecular ion information from the SI data to produce a high-quality qualitative analysis report.

With this in mind, it is important to have both GC/EI and GC/

SI in order to use the capabilities provided by msFineAnalysis iQ. The JMS-Q1600GC comes equipped with a standard EI source and has optional SI methods that include an EI/PI (Photoionization) combination ion source as well as a traditional Chemical Ionization (CI) ion source. The EI/PI source is particularly useful for this situation because switching between EI and PI does not require breaking vacuum. Additionally, the PI method relies on photons for ionization, making it simpler to use than CI which requires the selection of a reagent gas. That being said, CI is an effective SI method that can be very sensitive for a wide variety of analytes and only requires an ion volume exchange to switch from EI to CI.

The work-flow of the integrated qualitative analysis in msFineAnalysis iQ is shown in Fig. 6. Once the data is acquired by GC/EI and GC/SI, the peaks in the total ion chromatogram (TIC) are detected to create the mass spectra. For the peak detection, the deconvolution function is used to detect each peak, including deconvolving peaks with insufficient separation. Afterwards, each EI and SI mass spectrum is associated with a corresponding chromatographic peak retention time, and then the EI and SI mass spectra with the same retention times are assigned as the same

**Fig. 3 SIM chromatograms and peak area values for 5 fg of OFN measured continuously (n=8).**

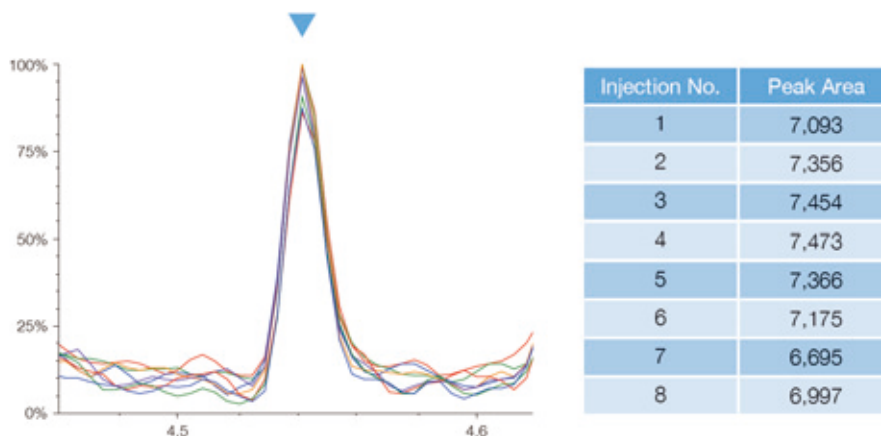
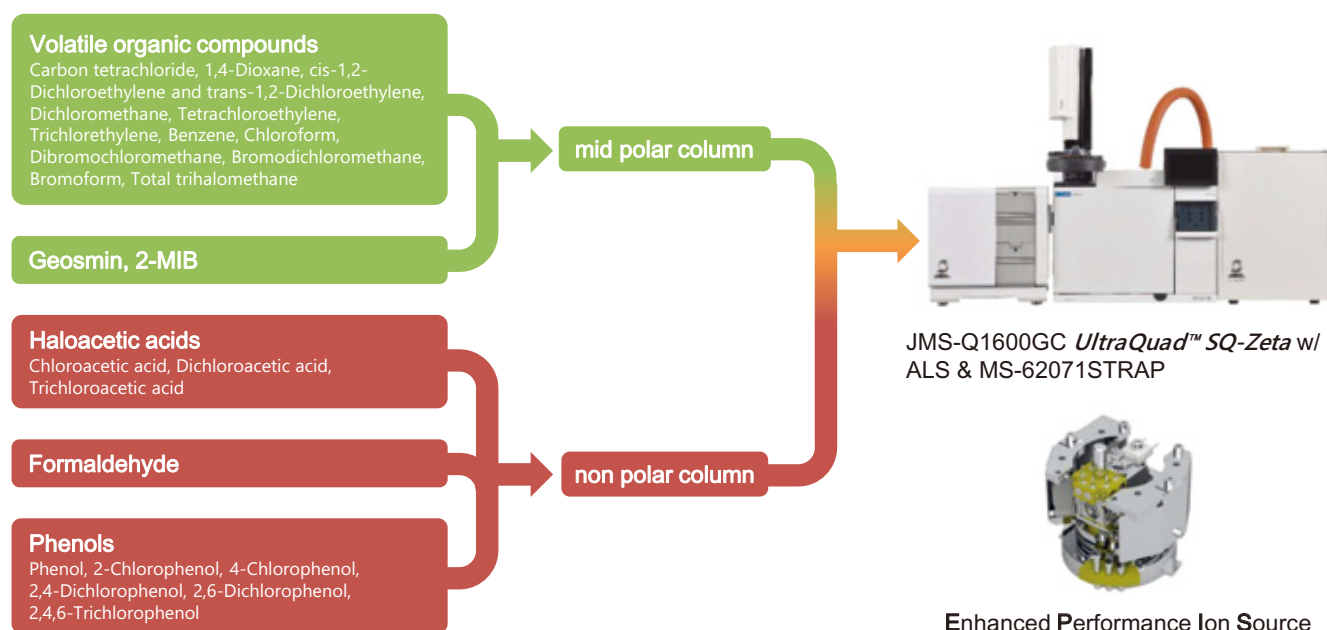


**Fig. 4 19 chemical compounds measured for Japanese Water Quality Standards GC-MS method.**



component. The EI mass spectra are then library searched for matches, and the candidates are further narrowed down using the retention index (RI) search. RI is effective in determining compounds that are difficult to identify by mass spectra alone, such as isomers. The NIST DB has about 350,000 RI values for about 70,000 compounds by column polarity and GC conditions. The SI mass spectra are then used to determine the molecular ions for each candidate, and the observed molecular ions are compared to the DB search results. Finally, all of these analysis results are integrated together into a qualitative analysis report for the peaks detected in the sample.

Another important feature of msFineAnalysis iQ is the variance components analysis function in which two similar samples can be directly compared in order to identify sample differences. This analysis function statistically compares two samples while also utilizing all of the normal msFineAnalysis iQ qualitative analysis capabilities described previously. Variance components analysis can be particularly useful for comparing complex materials that have subtle differences. In particular, this capability could be critically important for addressing changes in material synthesis or manufacturing processes in which product quality is critically important.

## Using msFineAnalysis iQ for the Qualitative Analysis of Commercial Polypropylene Products Measured by Pyrolysis GC-MS

In this study, we have measured two commercial polypropylene products by using pyrolysis GC-MS, and then analyzed the results by using msFineAnalysis iQ. The samples were commercially available non-woven polypropylene masks and antibacterial sheets for lunch boxes. A JMS-Q1600GC equipped with the EI/PI combination ion source and a pyrolyzer system (PY-3030D, Frontier Labs, Inc.) was used for the sample measurements. Each sample was measured  $n=5$  for the EI method and  $n=1$  for the PI method. Afterwards, msFineAnalysis iQ was used to compare the samples to each other.

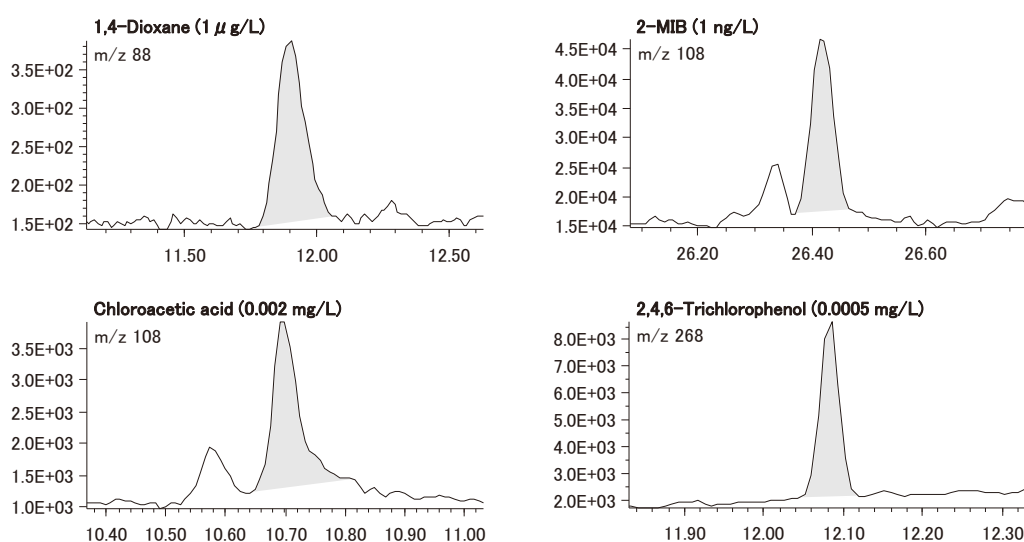
The Volcano plot comparing the non-woven masks and antibacterial sheets to each other as well as the integrated analysis results for several components specific to each sample identified from the Volcano plot are shown in Fig. 7. In the Volcano plot, each spot corresponds to one compound, and the overall spot size indicates the area value. The vertical axis in the volcano plot is the negative of the logarithm of the p-value, where the larger the value, the more reproducible the component. The horizontal axis is the logarithm of

**Table 1 Coefficients of variation values for 19 chemical compounds in the Japanese water quality standards.**

Compound Name	C.V. (%)	Sample Conc. ( $\mu\text{g/L}$ )	Standard Value ( $\mu\text{g/L}$ )
Carbon tetrachloride	0.1	2.0	2
1,4-dioxane	1	3.4	50
trans-1,2-dichloroethylene			
cis-1,2-dichloroethylene			
1,2-dichloroethylene	0.2	0.8	40
Dichloromethane	0.1	3.4	20
Tetrachlorethylene	0.1	0.9	10
Trichlorethylene	0.1	1.4	10
benzene	0.1	1.0	10
Chloroacetic acid	2	2.6	20
Chloroform	0.1	1.0	60
Dichloroacetic acid	2	1.9	30
Dibromochloromethane	0.1	2.6	100

Compound Name	C.V. (%)	Sample Conc. ( $\mu\text{g/L}$ )	Standard Value ( $\mu\text{g/L}$ )
Total trihalomethane	0.4	1.6	100
Trichloroacetic acid	2	0.8	30
Bromodichloromethane	0.1	1.8	30
Bromoform	0.1	2.5	90
Formaldehyde	1	0.7	80
2-Methylisoborneol	0.001	4.3	0.01
Geosmin	0.001	1.6	0.01
Phenol	0.5	0.9	5
2-Chlorophenol	0.5	0.5	
4-Chlorophenol	0.5	0.6	
2,6-dichlorophenol	0.5	0.9	
2,4-dichlorophenol	0.5	0.2	
2,4,6-Trichlorophenol	0.5	3.7	

**Fig. 5 SIM chromatograms at lower concentration limit for 1,4-Dioxane, 2-Methylisoborneol, Chloroacetic acid, and 2,4,6-Trichlorophenol.**

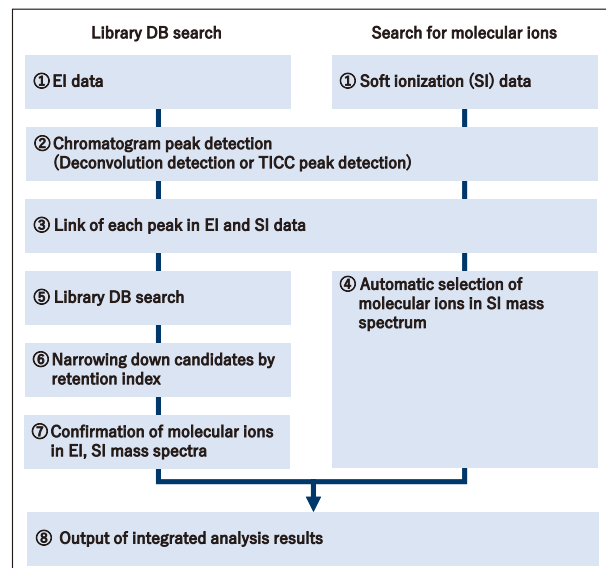


the intensity ratio between the two samples (Fold-change), where the larger absolute value indicates a larger gap in the peak area between the specimens. Additionally, the compounds plotted on the left side of the volcano plot are specific to non-woven masks, while those

compounds plotted on the right side are specific to antibacterial sheets. Also worth noting, the compounds plotted near the center were interpreted as common compounds that were found in both samples. In this example, the volcano plot shows that the majority of compounds detected were common to both samples.

For each compound in the volcano plot, msFineAnalysis iQ also performed an integrated qualitative analysis using the workflow shown in Figure 6. Afterwards, the software creates an integrated report in which the compound with the best match is automatically selected as the best candidate. As an example, the characteristic component “Compound 1” in the non-woven masks was identified as 2,4-Di-tert-butylphenol which is known as a raw material for antioxidants. The characteristic component “Compound 2” in the antibacterial sheet was identified as Benzene, 1,3-disocyanato-2-methyl-(2,6-TDI) which is known as a raw material for polyurethane and suggests the presence of polyurethane in the antibacterial sheet. As this work shows, msFineAnalysis iQ makes it simple to extract and identify components that are different between two samples.

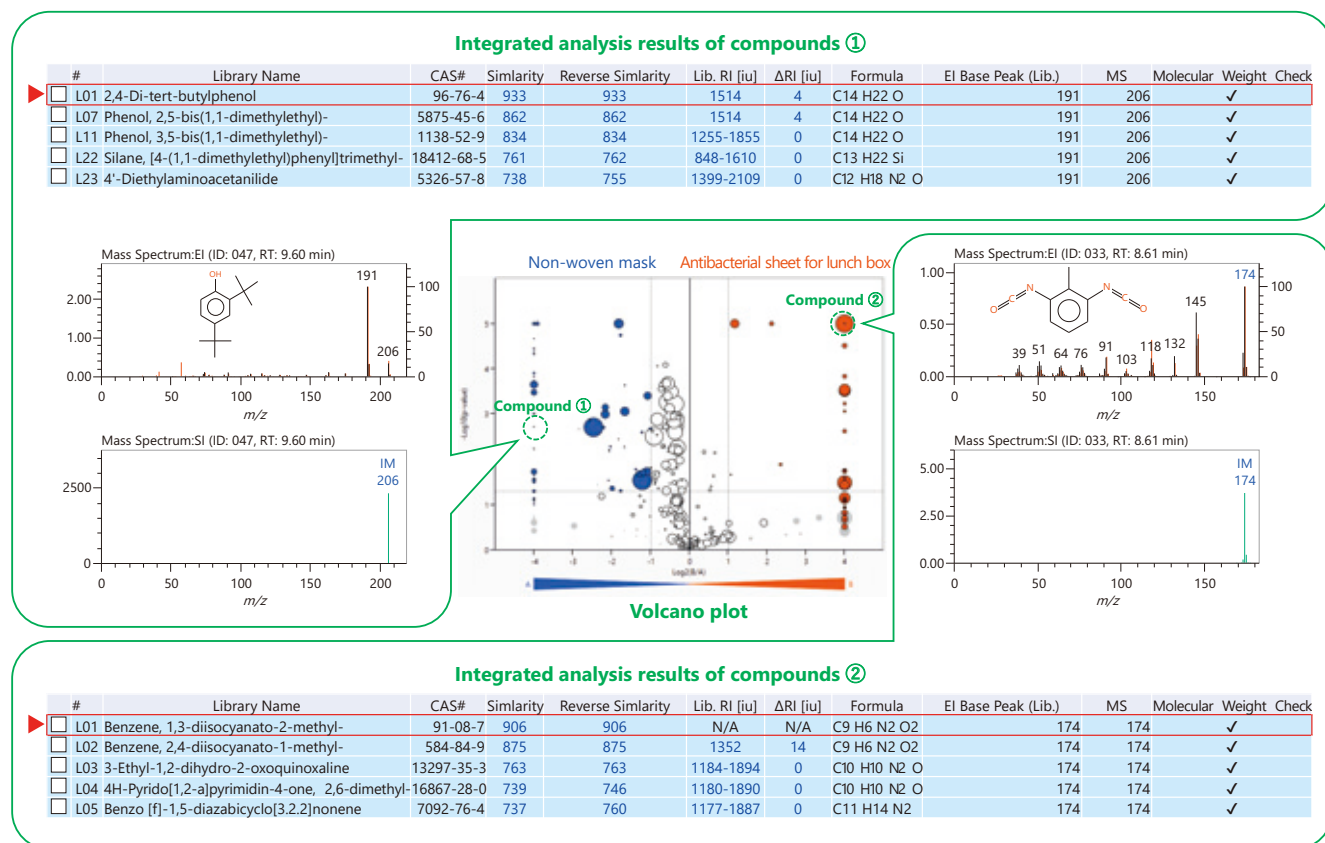
**Fig. 6 Integrated qualitative analysis work-flow on the msFineAnalysis iQ.**



## Conclusion

The “JMS-Q1600GC UltraQuad™ SQ-Zeta” is a GC-MS system that provides a variety of solutions for both qualitative and quantitative analysis. Furthermore, the addition of both the “EPIS” high-performance ion source and “msFineAnalysis iQ” automated qualitative analysis software provides unique capabilities that are not available with other GC-QMS systems. The JMS-Q1600GC provides powerful hardware and software solutions that can uniquely help with a variety of analytical applications and challenges.

**Fig. 7 Volcano plot of non-woven masks and antibacterial sheets, and integrated qualitative analysis result for specific compounds.**





# Introduction of JEOL Products

## Electron Beam Metal 3D Printer

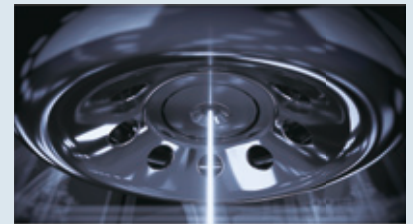
# JAM-5200EBM



Using electron beam control technology of the world's highest level performance electron microscope and electron beam lithography system for semiconductor manufacturing, JEOL has developed an "Electron Beam Metal 3D Printer" with high power, high speed and high density manufacturing. Enables mass production with high quality and high reproducibility.

### Long-life Cathode

The Long-life Cathode which lasts over 1,500 hours, can greatly reduce downtime for cathode replacement.



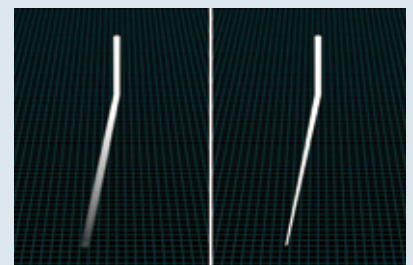
### Helium-Free and powder dispersal prevention system "e-Shield"

No helium gas is required to prevent scattering of powder. In addition, JEOL's unique powder dispersal prevention system avoids the scattering phenomenon. Thanks to the helium-free environment, not only can parts be manufactured in a clean space at a low cost, but "the surface of the cathode is also less susceptible to damage, allowing the electron beam to remain stable." As a result, the manufacturing quality can be maintained until the end of the cathode's lifetime.



### Automatic Electron Beam Correction

The focus and spot shape of the electron beam are automatically corrected according to the irradiation position by the technology developed in our electron beam lithography system for semiconductor manufacturing.

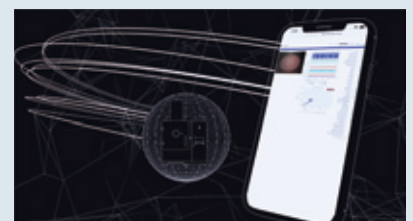


Uncorrected

Corrected (JEOL)

### Remote Monitoring System

The manufacturing status and the machine conditions can be checked from a remote location at any time. An alarm notification function is also available.



# Introduction of JEOL Products

## NMR Spectrometers

# JNM-ECZL series (ECZ Luminous)

## Lineup of ECZ Luminous

ECZ Luminous is available in three different models to meet a wide variety of user needs.

All models feature high performance digital high frequency technology and user-friendly Delta software.

### ECZL G series

This is a flagship model that supports diversified, cutting-edge applications. The footprint of the spectrometer has been reduced to less than 60% of that of ECZR, while maintaining the expandability needed to support a wide range of applications. It is flexible in terms of expansion, with support for three or more channels, high power amplifiers, and high power magnetic field gradients, allowing for future functional expansion even when installed in the minimum configuration. It is an adaptable FT-NMR system that can respond to changes in user applications and the introduction of the latest applications.



Dual rack configuration



### ECZL R series

This model is a compact spectrometer that is compatible with magnetic fields of up to 600 MHz. The footprint is less than 50% of that of ECZR, and it can also be used for solid-state measurements.



### ECZL S series

This is an entry-level model dedicated to 400 MHz solution NMR while incorporating the high performance digital high frequency technology of the ECZL series.



## More compact spectrometer

ECZ Luminous has achieved a significant reduction in size while enhancing the performance of the spectrometer. The volume of the R series has been reduced to about 1/3 of that of the previous equivalent.



Size comparison with previous models with equivalent performance

	ECZL G series	ECZL R series	ECZL S series
Frequency	400 MHz to 1.3 GHz	400 MHz to 600 MHz	400 MHz
Sample type	solution/solid	solution/solid	solution
Number of channels	2 ch (standard)	2 ch	2 ch
	Expandable up to 8 channels		
High frequency power amplifier	100 W (standard) 200/500/1000 W (as option)	100 W	50 W
Low frequency power amplifier	300 W (standard) 500/1000/2000 W (as option)	300 W	150 W
Magnetic field gradient amplifier	10 A (standard)	10 A	10 A
	30/50 A (as option)		
Console size (W × D × H)	600 × 855 × 1,279 mm	536 × 730 × 855 mm	536 × 730 × 855 mm



Certain products in this brochure are controlled under the "Foreign Exchange and Foreign Trade Law" of Japan in compliance with international security export control, JEOL Ltd. must provide the Japanese Government with "End-user's Statement of Assurance" and "End-use Certificate" in order to obtain the export license needed for export from Japan. If the product to be exported is in this category, the end user will be asked to fill in these certificate forms.

**ARGENTINA**  
COASIN S.A.C.I.F.  
Virrey del Pino 4071,  
C14300AH-Buenos Aires  
Argentina  
Tel. 54-11-4552-3185  
Fax. 54-11-4555-3321

**AUSTRALIA & NEW ZEALAND**  
JEOL (AUSTRALASIA) Pty.Ltd.  
Suite 1, L2 18 Aquatic Drive  
- Frenchs Forest NSW 2086  
Australia  
Tel. 61-2-9451-3855  
Fax. 61-2-9451-3822

**AUSTRIA**  
JEOL (GERMANY) GmbH  
Gute Aenger 30  
83306 Freising, Germany  
Tel. 49-8161-9845-0  
Fax. 49-8161-9845-100

**BANGLADESH**  
A.O. CHOWDHURY SCIENCE & SYNERGY PVT. LTD.  
87, Suhrawardy Avenue, Floor 2  
Bardhara, Dhaka1212  
Bangladesh  
Tel. 88-02-222262272  
Fax. 88-02-222264228

**BELGIUM**  
JEOL (EUROPE) B.V.  
Planet II, Gebouw B  
Leuvensesteenweg 542,  
B-1930 Zaventem  
Belgium  
Tel. 32-2-720-0560  
Fax. 32-2-720-6134

**BRAZIL**  
JEOL Brasil Instrumentos Cientificos Ltda.  
Av. Jabaquara, 2958 5º andar conjunto 52 ;  
04046-500 Sao Paulo, SP  
Brazil  
Tel. 55-11-5070 4000  
Fax. 55-11-5070 4010

**CANADA**  
JEOL CANADA, INC.  
3275 Tere Rue, Local #8  
St-Hubert, QC J3Y4Y6, Canada  
Tel. 1-450-676-8776  
Fax. 1-450-676-8694

**CHINA**  
JEOL (BEIJING) CO., LTD.  
Zhongkeziyuan Building South Tower 2F  
Zhongguancun Nanshanjie Street No. 6,  
Haidian District, Beijing, P.R.China  
Tel. 86-10-6804-6321  
Fax. 86-10-6804-6324

**JEOL (BEIJING) CO., LTD., SHANGHAI BRANCH**  
2F-3C Room, Building A, Mingji Business Plaza,  
No.207 Songhong Road, Changning District,  
Shanghai 200335, P.R.China  
Tel. 86-21-6249-4987  
Tel. 86-21-5836-6350  
Fax. 86-21-5836-3668

**JEOL (BEIJING) CO., LTD., GUANGZHOU BRANCH**  
Rm.3501, OnelinkCenter, 230 Tianhe Road, Tianhe District,  
Guangzhou, Guangdong Prov., 510620, China  
Tel. 86-20-8778-7849  
Fax. 86-20-8778-4268

**JEOL (BEIJING) CO., LTD., WUHAN BRANCH**  
Room A2118, Zhongshang Plaza Office Bldg.,  
No. 7 Zhongnan Road, Wuhan,  
Hubei, 430070, P.R.China  
Tel. 86-27-8713-2567  
Fax. 86-27-8713-2567

**JEOL LTD. (BEIJING) CO., LTD., CHENGDU BRANCH**  
1807A Zongfu Building,  
NO. 35 Zhongfu Road, Chengdu, Sichuan, 610016  
P.R. China  
Tel. 86-28-86622554  
Fax. 86-28-86622564

**EGYPT**  
JEOL SERVICE BUREAU  
3rd Fl. Nile Center Bldg., Nawal Street,  
Dokki, Cairo, Egypt  
Tel. 20-2-3335-7220  
Fax. 20-2-3338-4186

**FRANCE**  
JEOL (EUROPE) SAS  
Espace Claude Monet, 1 Allée de Giverny  
78290, Croissy-sur-Seine, France  
Tel. 33-1-9015-9737  
Fax. 33-1-9015-9747

**GERMANY**  
JEOL (GERMANY) GmbH  
Gute Aenger 30  
83306 Freising, Germany  
Tel. 49-8161-9845-0  
Fax. 49-8161-9845-100

**GREAT BRITAIN & IRELAND**  
JEOL (U.K.) LTD.  
Silver Court, Watchmead,  
Welwyn Garden City, Hertfordshire AL7 1LT, U.K.  
Tel. 44-1707-377117  
Fax. 44-1707-373254

**GREECE**  
N. ASTERIAS S.A.  
56-58 S. Tikoupi Str. P.O. Box 26140  
GR-1022, Athens, Greece  
Tel. 30-1-823-3383  
Fax. 30-1-823-9567

**HONG KONG**  
FARMING LTD.  
Unit No. 1009, 10/F, Prosperity  
683 King's Road, North Point, Hong Kong  
Tel. 852-2815-7234  
Fax. 852-2581-4635

**INDIA**  
JEOL INDIA PVT. LTD.  
Unit No.305, 3rd Floor,  
ABW Elegance Tower,  
Jasola District Centre,  
New Delhi 110 025, India  
Tel. 91-11-4595-8000  
Tel. 91-11-4595-8005  
Tel. 91-11-4595-8017

**JEOL INDIA PVT. LTD. Mumbai Office**  
214 E Square, Subhash Road,  
Vile Park (EAST),  
Mumbai 400 057, India  
Tel. 91-22-2612-9387

**JEOL INDIA PVT. LTD. Bangalore Office**  
125, Brigade Road,  
Unit No.402, Level 4, Palm Square,  
Bangalore-560025, India  
Tel. 91-80-4375-9351

**JEOL INDIA PVT. LTD. Kolkata Office**  
Regus, The Legacy, 25 / A,  
Shakaspore Sarani,  
Kolkata - 700017, India  
Tel. 91-98-3023-0484

**JEOL INDIA PVT. LTD. Hyderabad Office**  
422, Regus Solitaire Business centre,  
1-10-39 to 44, level 4, Gumdelli Towers, Old Airport Road,  
Begumpet, Hyderabad - 500016, India  
Tel. 91-40-6704-3708

**INDONESIA**  
PT. TEKNO LABindo Penta Perkasa  
Komplek Gading Bukit Indah Blok I/11  
Jl. Bukit Gading Raya Kelapa Gading Permai,  
Jakarta 14240, Indonesia  
Tel. 62-21-46847057/58  
Fax. 62-21-45842729

**ITALY**  
JEOL (ITALIA) S.p.A.  
Palazzo Pagnotti - Milano 3 City,  
Via Ludovico Il Moro, 5/A  
20079 Basiglio(MI) Italy  
Tel. 39-02-9041431  
Fax. 39-02-90414343

**KOREA**  
JEOL KOREA LTD.  
Dongwoo Bldg. 7F, 1443, Yangjae Daero,  
Gangdong-gu, Seoul, 05355, Korea  
Tel. 82-2-511-8501  
Fax. 82-2-511-2635

**KUWAIT**  
Ashraf & CO., Ltd.  
P.O.Box 3555 Safat, 13036, Kuwait  
Tel. 965-2435151  
Fax. 965-2433373

**MALAYSIA**  
JEOL (MALAYSIA) SDN.BHD.  
508, Block A, Level 5,  
Kollam Business Center,  
97, Jalan SS 7/2, Kelana Jaya,  
47301 Petaling Jaya, Selangor, Malaysia  
Tel. 60-3-7482-7722  
Fax. 60-3-7482-7723

**MEXICO**  
JEOL DE MEXICO S.A. DE C.V.  
Arkasana 11 Piso 2  
Colonia Naples  
Delegacion Benito Juarez, C.P. 03810  
Mexico D.F., Mexico  
Tel. 52-5-55-211-4511  
Fax. 52-5-55-211-0720

**Middle East**  
JEOL GULF FZCO  
P.O. Box No. 371107  
Dubai Airport Free Trade Zone West Wing 5WA No. G12,  
Dubai, UAE  
Tel. 971-4-609-1497  
Fax. 971-4-609-1498

**PAKISTAN (Karachi)**  
ANALYTICAL MEASURING SYSTEM (PVT) LTD. (AMS LTD.)  
14-C Main Sehar Commercial Avenue Lane 4,  
Khayaban-e-Sehar,  
D.H.A.VIII, Karachi-75500, Pakistan  
Tel. 92-21-35345581/35340747  
Fax. 92-21-35345582

**PANAMA**  
PROMED S.A.  
Parque Industrial Costa del Este  
Urbanizacion Costa del Este  
Apartado 0316-01765, Panama, Panama  
Tel. 507-303-3100  
Fax. 507-303-3115

**PHILIPPINES**  
JATECO Philippines Corporation  
28 Floor, The Enterprise Center Tower 2,  
Ayala Avenue corner Paseo de Roxas,  
Brno, San Lorenzo, Makati City, 1226 Philippines  
Tel. (632) 849 3904

**PORTUGAL**  
Izasa Portugal Lda.,  
R. do Proletariado, 1  
2780-193 CARNAXIDE, Portugal  
Tel. 351-21-424-73-00  
Fax. 351-21-418-60-20

**QATAR**  
Marnal Trading Company W.L.L.  
AlI Emadi Complex,  
Salwa Road P.O.Box 76, Doha, Qatar  
Tel. +974 4455-8216  
Fax. +974 4455-8214

**RUSSIA**  
JEOL (RUS) LLC  
Office 351, floor 3, 23,  
Novoslobodskaya St,  
Moscow 127059, Russia  
Tel. 7-495-748-7791/7792  
Fax. 7-495-748-7793

**SAUDI ARABIA**  
ABDULREHMAN ALGOSAIBI G.T.C. (Riyadh)  
Algosabi Building-Old Airport Road  
P.O. Box 213, Riyadh-11411, Saudi Arabia  
Tel. 966-1-477-7592

**SCANDINAVIA**  
SWEDEN  
JEOL (Nordic) AB  
Hammarbacken 6A, Box 716, 191 27 Sollentuna  
Sweden  
Tel. 46-8-298-2800  
Fax. 46-8-298-1647

**SINGAPORE**  
JEOL ASIA PTE.LTD.  
2 Corporation Road  
#01-12 Corporation Place  
Singapore 618434  
Tel. 65-6565-9369  
Fax. 65-6565-7552

**SOUTH AFRICA**  
AD Scientific (Pty) Ltd.  
370 Angus Crescent,  
Northlands Business Park, 29 Newmarket Road  
Northridge, Randburg, Republic of South Africa  
Tel. 27-11-462-1363  
Fax. 27-11-462-1466

**SPAIN**  
IZASA Scientific SLU.  
Argoneses, 13, 28108 Alcobendas,  
Madrid, Spain  
Tel. 34 902 20 30 80  
Fax. 49-8165-77246

**SWITZERLAND**  
JEOL (GERMANY) GmbH  
Gute Aenger 30  
83306 Freising, Germany  
Tel. 49-8165-77246  
Fax. 49-8165-77512

**TAIWAN**  
JIE DONG CO., LTD.  
7F, 112, Chung Hsiao East Road,  
Section 1, Taipei, Taiwan 10023 (R.O.C.)  
Tel. 886-2-2935-2978  
Fax. 886-2-2922-4665

For NMR & Mass Spectrometer Products:  
TechMax Technical Co., Ltd.  
5F, No.11, Wuqian 2nd Rd., Wugu Dist.,  
New Taipei City 248, Taiwan (R.O.C.)  
Tel. 886-2-8980-1779  
Fax. 886-2-8990-2559

For Semiconductor Products:  
JEOL TAIWAN SEMICONDUCTORS LTD.  
2F-2, No. 192, Dongguang Rd.  
East Dist., Hsinchu City 30069,  
Taiwan (R.O.C.)  
Tel. 886-3-571-5656  
Fax. 886-3-571-5151

**THAILAND**  
BECTHAI BANGKOK EQUIPMENT & CHEMICAL CO., Ltd.  
300 Phaholyothin Rd. Phayathai, Bangkok 10400,  
Thailand  
Tel. 66-2-615-2929  
Fax. 66-2-615-2350/2351

**JEOL ASEAN TECHNICAL CENTER (JATC)**  
MTEC building room 533  
11400, Thailand Science Park  
Paholyothin Rd., Klong 1, Klong Luang,  
Pathumthani 12120  
THAILAND  
Tel. 66-2-564-7738  
Fax. 66-2-564-7739

**THE NETHERLANDS**  
JEOL (EUROPE) B.V.  
Lureweg 4, NL-2153 PH Nieuw-Vennep,  
The Netherlands  
Tel. 31-252-623500  
Fax. 31-252-623501

**TURKEY**  
Tekser A.S.  
Kartal Cad. No: 55/3 Inonu Wah.,  
Atasehr 34755, Istanbul, Turkey  
Tel. 90-216-5733470  
Fax. 90-216-5736475

**USA**  
JEOL USA, INC.  
11 Dearborn Road, Peabody, MA 01960, U.S.A.  
Tel. 1-978-535-5900  
Fax. 1-978-536-2205/2206

**JEOL USA, INC. WEST OFFICE**  
5653 Stoneridge Drive Suite #110  
Pleasanton, CA 94588, U.S.A.  
Tel. 1-925-737-1740  
Fax. 1-925-737-1749

**VENEZUELA**  
GOMSA Service and Supply C.A.  
Urbanizacion Montalban III  
- Residencias Don Andres - Piso 7 - Apartamento 74  
Avenida 3, entre calles 7 y 8  
Montalban, Caracas, Venezuela  
Tel. 58-212-443-4342  
Fax. 58-212-443-4342

**VIETNAM**  
TECHNICAL MATERIALS AND RESOURCES  
IMPORT-EXPORT JOINT STOCK COMPANY (REXCO)  
Hanoi Branch  
SALES & SERVICE  
155-157 Lang Ha Street, Dong Da District, Hanoi, Vietnam  
Tel. +84 (43) 582 0516  
Fax. +84 (43) 853 2511